UNIVERSITÀ DEGLI STUDI DI SALERNO

DIPARTIMENTO DI FISICA "E.R. CAIANIELLO"

THESIS SUBMITTED FOR THE DEGREE OF

DOCTOR OF PHYLOSOPHY IN PHYSICS

XIII CYCLE - II SERIES (2012-2016)

GRAPHENE AND CARBON NANOTUBES IN TRANSISTORS, DIODES AND FIELD EMISSION DEVICES

LAURA IEMMO

SUPERVISOR

PROF ANTONIO DI BARTOLOMEO

COORDINATOR

PROF CANIO NOCE

A.A. 2016/2017

To my children
Aurora and Ivan

Contents

Introduction **1**

Bibliography **4**

1 Graphene and carbon nanotubes: theoretical and experimental background **6**

1.1 Introduction 6

1.2 Graphene 7

1.2.1 The direct lattice 8

1.2.2 The reciprocal lattice 9

1.2.3 Electronic properties 10

1.2.4 Graphene nanoribbons 15

1.2.5 Transport properties 16

1.2.6 Optical properties 20

1.3 Carbon nanotubes 20

1.3.1 The direct lattice 21

1.3.2 Brillouin zone 23

1.3.3 Electronic and transport properties 25

1.4 Theory of the field emission 30

Bibliography **32**

2 Graphene-based field-effect transistors **35**

2.1 Introduction 35

2.2 GFETs with Nickel and Titanium contacts 40

2.2.1 Devices fabrication and measurement setup 40

2.2.2 Results and discussion 42

2.2.2.1 Transfer characteristics 42

2.2.2.2 Contact resistance 44

2.3 GFETs with Niobium contacts 48

2.3.1 Devices fabrication and measurement setup 48

2.3.2 Results and discussion 50

2.3.2.1 Transfer characteristics 50

2.3.2.2 Contact resistance 52

2.3.2.3 Effect of electron beam irradiation 58

2.4 Side-gate GFETs 59

2.4.1 Devices fabrication and measurement setup 59

2.4.2 Results and discussion 61

2.4.2.1 Transfer characteristics 61

2.4.2.2 Leakage current and field emission 63

2.5 Conclusions 68

Bibliography **70**

3 Graphene/Si-nanotip Schottky diode **76**

3.1 Introduction 76

3.2 Device fabrication and measurement setup 77

3.3 Results and discussion 79

3.3.1 Schottky barrier. 79

3.3.2 Photoresponse 90

3.4 Conclusions 92

Bibliography **93**

4 Transport and field emission properties of CNTs **96**

4.1 Introduction 96

4.2 Samples fabrication and measurement setup 97

4.3 Results and discussion 99

4.3.1 The temperature dependence of the conductance 99

4.3.2 Field emission 102

4.4 Conclusions 106

Bibliography **107**

Conclusions **111**

Publications **114**

Acknowledgments **116**

Introduction

Since their discovery, graphene and carbon nanotubes have been playing an important role in nanoscience and nanotechnology thanks to their extraordinary physical and chemical properties.

Graphene, the two-dimensional layer of sp^2 carbon atoms discovered in 2004 [1], is an excellent material for electronic devices for its linear dispersion relation with electrons behaving as massless Dirac fermions [2], high electron mobility [3], great electric current carrying capacity [4], capability of being tuned from p-type to n-type doping by the application of a gate voltage, high thermal conductivity [5], record mechanical strength [6], resilience to high temperatures [7] and humidity [8], structural flexibility, resistance to molecule diffusion and chemical stability. Because of these exceptional properties, graphene has stirred a lot of interest in the scientific community for basic science and for technological applications, and it is considered a potential breakthrough in terms of carbon-based nanoelectronics.

With silicon-based electronics tending towards its scaling limits, the semiconductor industry is looking for the next switch which can replace the silicon field-effect transistor [9] and graphene can be a possible alternative for silicon. Graphene-based field-effect transistors (GFETs) [10] combine an ultra-thin body suitable for aggressive channel length scaling [11], with exceptional electronic properties [12]. However the development of graphene-based electronics is limited by the quality of contacts between the graphene and metal electrodes [13-15] that can significantly affect the electronic transport properties of the devices [16]. For such reason it becomes of fundamental importance to characterize metal/graphene interfaces at the contacts.

Further, due to its important advantage of being naturally compatible with thin film processing, graphene is easy to integrate into existing semiconductor device technologies. The graphene-silicon (Gr/Si) heterojunction is one of the simplest conceivable device in a hybrid graphene-semiconductor technology and it offers great opportunity to study the physics occurring at the interface between a 2D and a 3D material, as well as between a zero and a definite bandgap system, and can be a convenient platform to investigate electronic properties and transport mechanisms. Nonetheless, the Gr/Si junction has already been demonstrated as a rectifying or a barrier-variable device, a photovoltaic cell [17-19], a bias-tunable photodetector [20-22], a chemical-biological sensor [23-25] and it is gaining interest

from the semiconductor industry also for the potentiality to replace ultra-shallow doped junctions in modern complementary-metal-oxide-semiconductor (CMOS) technologies.

Carbon nanotubes (CNTs), for their very high aspect ratio (diameter in the nanometer scale and length of several microns), extremely small radius of curvature, unique electric properties, high chemical stability and important mechanical strength [26-29], have been considered extraordinary elements to realize field emission devices, since their discovery in 1991 [30]. Field emission (FE), which involves extraction of electrons from a conducting solid by an external electric field, is at the basis of several technological applications. Nowadays, CNT based field emitters are used in vacuum electronics to produce electron sources [31], flat panels [32], X-ray sources [23,24], and microwave amplifiers [35], exploiting a low-threshold electric field and large emission current density. As CNTs, also graphene has high potentiality for FE applications, due to its high aspect ratio (thickness to lateral size ratio) and a dramatically enhanced local electric field is expected at its edges.

The aim of this PhD thesis was to study electronic properties and transport mechanisms of graphene and carbon nanotubes through an extensive electrical characterization of field-effect transistors, diodes and field emission devices based on these materials.

The thesis is organized as follows.

In the first chapter, we describe the physical and electronic structures of graphene and carbon nanotubes in order to understand the transport properties and performance of studied devices. Moreover, we report a brief introduction to the optical properties of graphene and the field emission theory.

In the second chapter, we present the fabrication of graphene based field effect transistors in bottom and side gate configuration, and we perform an intense electrical characterization by measuring transfer and output characteristics. In particular, we study the physical effects due to the contact resistance between graphene and different metal electrodes. We discuss the effects of room temperature vacuum degassing and of low-energy electron beam irradiation on GFETs. Finally, we study the side-gating effect, the gate leakage in all-graphene devices and the field emission from graphene.

In the third chapter, we study a new-concept of Gr/Si photodiode made of a single-layer graphene transferred onto a matrix of nanotips patterned on n-type Si wafer. Through an extensive characterization, we estimate the relevant junction parameters. In particular, we analyze the effect of the tip geometry on the Schottky barrier height and on the photoresponse.

In the fourth chapter, we describe the transport characteristics in a wide temperature range and the field emission properties of buckypapers obtained from aligned carbon nanotubes. We report the study of the long-term stability of the field emission current and finally, we analyze the effect on the emitted current due to in plane applied currents in the buckypaper.

Bibliography

[1] Novoselov K S, Geim A K, Morozov S V, Jiang D, Zhang Y, Dubonos S V, Grigorieva I. V and Firsov A A 2004 *Science* **306** 666-669.

[2] Castro Neto A H, Guinea F, Peres N M R, Novoselov K S and Geim A K 2009 *Rev. Mod. Phys.* **81** 109 -162.

[3] Du X, Skachko I, Barker A and Andrei E Y 2008 *Nat. Nanotechnol.* **3** 491-495.

[4] Moser J, Barreiro A and Bachtold A 2007 *Appl. Phys. Lett.* **91** 163513.

[5] Balandin A A, Ghosh S, Bao W, Calizo I, Teweldebrhan D, Miao F and Lau C N 2008 *Nano Lett.* **8** 902-907.

[6] Lee C, Wei X, Kysar J W and Hone J 2008 *Science* **321** 385-388.

[7] Los J H, Zakharchenko K V, Katsnelson M I and Fasolino A 2015 *Phys. Rev. B* **91** 045415.

[8] Su P-G and Chiou C-F 2014 *Sensors and Actuators B* **200** 9–18.

[9] Bourianoff G, Brillouet M, Cavin R K, Hiramoto T, Hutchby J A, Ionescu A M and Uchida K 2010 *Proc. IEEE* **98** 1986–92.

[10] Schwierz F 2010 *Nature Nanotechnology* **5** 487-96.

[11] Meric I, Dean CR, Young AF, Baklitskaya N, Tremblay NJ, Nuckolls C, Kim P and Shepard KL 2011 *Nano Lett.* **11** 1093-7.

[12] Das Sarma S, Adam S, Hwang EH and Rossi E 2011 *Rev. Mod. Phys.* **83** 407-70.

[13] Nagashio K, Nishimura T, Kita K and Toriumi A 2010 *Jpn J. Appl. Phys.* **49** 051304.

[14] Nagashio K, Nishimura T, Kita K and Toriumi A 2010 *Appl. Phys. Lett.* **97** 143514.

[15] Khomyakov P A, Starikov A A, Brocks G and Kelly P J 2010 *Phys. Rev. B* **82** 115437.

[16] Nagashio K, Nishimura T, Kita K and Toriumi A 2009 *IEEE IEDM Tech. Dig.* **7-9** 565–68.

[17] An X, Liu F and Kar S 2013 *Carbon* **57** 329–337.

[18] Behura S K, Nayak S, Mukhopadhyay I and Jani O 2014 *Carbon* **67** 766–774.

[19] Ruan K, Ding K, Wang Y, Diao S, Shao Z, Zhang X and Jie J 2015 *J. Mater. Chem. A* **3** 14370-14377.

[20] An X, Liu F, Jung Y J and Kar S 2013 *Nano Lett.* **13** 909–916.

[21] Ferrari A, Bonaccorso F, Fal'ko V, Novoselov K S, Roche S, Bøggild P, Borini S, Koppens F H, Palermo V, Pugno N et al. 2015 *Nanoscale* **7** 4598-4810.

[22] Riazimehr S, Bablich A, Schneider D, Kataria S, Passi V, Yim C, Duesberg G S and Lemme M C 2016 *Solid-State Electronics* **115** 207-212.

[23] Kim H Y, Lee K, McEvoy N, Yim C and Duesberg G S 2013 *Nano Lett.* **13** 2182–2188.
[24] Singh A, Uddin A, Sudarshan T and Koley G 2014 *Small* **10** 1555-1565.
[25] Fattah A, Khatami S, Mayorga-Martinez C C, Medina-Sánchez M, Baptista-Pires L and Merkoçi A 2014 *Small* **10** 4193–4199.
[26] Popov VN and Henrard L 2004 *Mater Sci Eng* **43** 61–102.
[27] Harris PJF *Carbon nanotubes and related structures* 1999 Cambridge University Press.
[28] Saito R, Dresselhaus G and Dresselhaus MS 2004 Imperial College Press, London.
[29] Anantram MP and Léonard F 2006 *Rep Progr Phys* **69** 507–61.
[30] Iijima S 1991 *Nature* **354** 56–8.
[31] Saito Y and Uemura S 2000 *Carbon* **38** 169-182.
[32] Wang Q H, Yan M and Chang R P H 2001 *Appl. Phys. Lett.* **78** 1294–1296.
[33] Zhang J, Yang J, Cheng Y, Gao B, Qiu Q, Lee YZ, Lu JP and Zhou O 2005 *Appl. Phys. Lett.* **86** 184104.
[34] Liu Z, Yang G, Lee YZ, Bordelon D, Lu J and Zhou O 2006 *Appl. Phys. Lett.* **89** 103111.
[35] Teo KB, Minoux E, Hudanski L, Peauger F, Schnell JP, Gangloff L, Legagneux P, Dieumegard D, Amaratunga GA and Milne WI 2005 *Nature* **437** 968–968.

Chapter 1

Graphene and carbon nanotubes: theoretical and experimental background

1.1 Introduction

Carbon is one of the most versatile elements in the periodic table in terms of the number of compounds it may create, mainly due to the types of bonds it may form (single, double, and triple bonds) and the number of different atoms it can join in bonding. It can form a broad variety of architectures in all dimensions, both at the macroscopic and nanoscopic scales. During the last 25 years, brave new forms of carbon have been unveiled. The family of carbon-based materials now extends from C_{60} to carbon nanotubes, and from old diamond and graphite to graphene. The properties of the new members of this carbon family are so impressive that they may even redefine our era.

Under standard conditions (ordinary temperatures and pressures), the stable form of carbon is graphite. Graphite is a famous lubricant, an electrical (semimetal) and thermal conductor, and reflects visible light [1].

Graphite is a three-dimensional crystal made of stacked layers consisting of sp^2 hybridized carbon atoms; each carbon atom is connected to another three making an angle of 120° with a bond length of 1.42 $\AA$. This anisotropic structure clearly illustrates the presence of strong σ covalent bonds between carbon atoms in the plane, while the π bonds provide the weak interaction between adjacent layers in the graphitic structure. The σ-bonds, that have the electrons localized along the plane connecting carbon atoms, are responsible for the great strength and mechanical properties of graphene and carbon nanotubes [2,3], while the 2p electrons, that are weakly bound to the nuclei and hence relatively delocalized, are the ones responsible for the electronic properties of graphene and carbon nanotubes [1,4].

The objective of this chapter is to describe the physical and electronic structures of graphene and carbon nanotubes in order to understand the electronic properties and transport mechanisms in the studied electronic devices. Briefly, we report the optical properties of

graphene, that are important for the analysis of graphene-based optoelectronic devices. Finally, we introduce the field emission theory, whose properties and applications are currently the subject of a very active research field.

1.2 Graphene

Isolated graphene was discovered in 2004 by Geim and Novoselov [5,6], who made graphene accessible with a technique as simple as the mechanical exfoliation.

Graphene is a one-atom thick, planar layer consisting of sp^2 hybridized carbon atoms arranged in a 2D hexagonal honeycomb. The planar honeycomb structure of graphene has been observed experimentally and is shown in Fig. 1.1 [4].

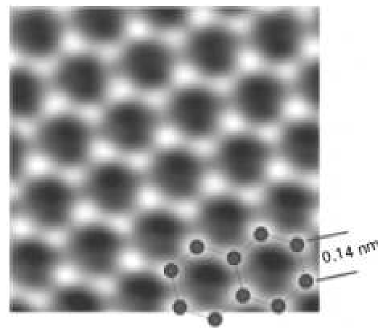

FIGURE 1.1: Remarkable transmission electron aberration-corrected microscope (TEAM) image of graphene vividly showing the carbon atoms and bonds in the honeycomb structure.

Graphene can be considered the mother of three carbon allotropes. As illustrated in Fig. 1.2, wrapping graphene into a sphere produces buckyballs, folding into a cylinder produces nanotubes, and stacking several sheets of graphene leads to graphite [7].

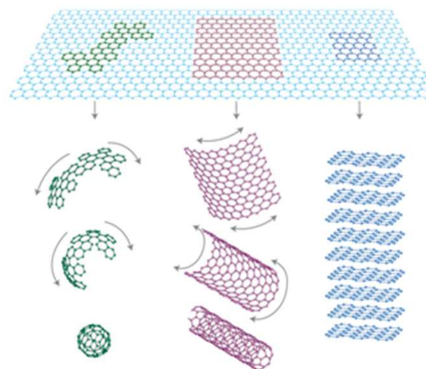

FIGURE 1.2: Two-dimensional graphene can be considered the building block of several carbon allotropes in all dimensions, including zero-dimensional buckyballs, 1D nanotubes, and 3D graphite.

1.2.1 The direct lattice

Graphene has a honeycomb lattice shown in Fig. 1.3 using a ball-and-stick model [4]. The balls represent carbon atoms and the sticks symbolize the σ-bonds between atoms. The carbon–carbon bond length is approximately $a_{c\text{-}c} \approx 1.42\ \AA$.

The honeycomb crystal can be mapped to a triangular Bravais lattice with a basis of two atoms, which can be considered as made of two interpenetrating triangular sub-lattices, indicated as A and B in Fig. 1.3. These contribute a total of two π electrons per unit cell to the electronic properties of graphene. The primitive unit vectors as defined in Fig. 1.3 are:

$$\mathbf{a}_1 = \left(\frac{\sqrt{3}a}{2}, \frac{a}{2}\right), \quad \mathbf{a}_2 = \left(\frac{\sqrt{3}a}{2}, -\frac{a}{2}\right), \tag{1.1}$$

with $|\mathbf{a}_1| = |\mathbf{a}_2| = a = \sqrt{3}a_{c-c} = 2.46\ \text{Å}$.

Each carbon atom is bonded to its three nearest neighbors and the vectors describing the separation between a type A atom and the nearest neighbor type B atoms as shown in Fig. 1.3 are:

$$\mathbf{R}_1 = \left(\frac{a}{\sqrt{3}}, 0\right), \ \mathbf{R}_2 = -\mathbf{a}_2 + \mathbf{R}_1 = \left(-\frac{a}{2\sqrt{3}}, -\frac{a}{2}\right), \ \mathbf{R}_3 = -\mathbf{a}_1 + \mathbf{R}_1 = \left(-\frac{a}{2\sqrt{3}}, \frac{a}{2}\right), \tag{1.2}$$

with $|\mathbf{R}_1| = |\mathbf{R}_2| = |\mathbf{R}_3| = a_{c-c}$.

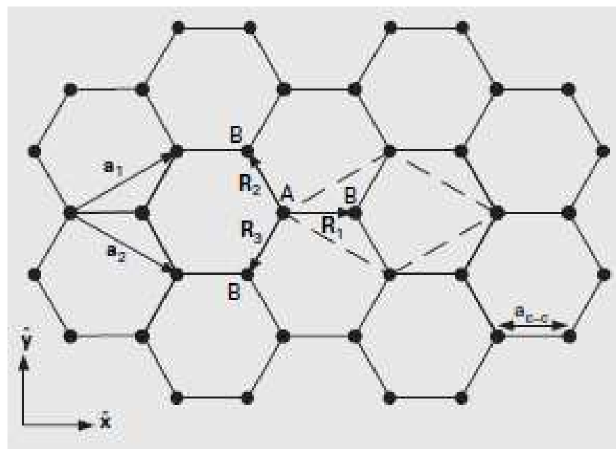

FIGURE 1.3: The honeycomb lattice of graphene. The primitive unit cell is the equilateral parallelogram (dashed lines) with a basis of two atoms denoted as A and B.

1.2.2 The reciprocal lattice

The reciprocal lattice, that is the discrete Fourier transform of the direct lattice, satisfies the basic relation:

$$e^{i\mathbf{K}\cdot\mathbf{R}} = 1, \tag{1.3}$$

where **K** is the set of wavevectors that determine the sites of the reciprocal lattice points and **R** is the Bravais lattice position vector [4].

In two dimensions, the primitive vectors of the reciprocal lattice ($\mathbf{b}_1$ and $\mathbf{b}_2$) are determined from the primitive vectors of the direct lattice ($\mathbf{a}_1$ and $\mathbf{a}_2$):

$$b_1 = 2\pi\frac{R_{90}(a_2)}{det(a_1, a_2)}, \quad b_2 = 2\pi\frac{R_{90}(-a_1)}{det(a_1, a_2)}, \tag{1.4}$$

where R_{90} is an operator that rotates the vector clockwise by 90° and *det* is the determinant, which geometrically is the area of the parallelogram formed by $\mathbf{a}_1$ and $\mathbf{a}_2$ and serves as a normalization factor. From the rotation operator, it is evident that the reciprocal lattice primitive vectors are either normal or parallel to the direct lattice primitive vectors, corresponding to $\mathbf{a}_i \cdot \mathbf{b}_j = 2\pi\delta_{ij}$, where δ_{ij} is the Kronecker delta function.

The reciprocal lattice of graphene shown in Fig. 1.4 is also a hexagonal lattice, but rotated 90° with respect to the direct lattice. The reciprocal lattice vectors are (from eq. (1.4)):

$$\mathbf{b}_1 = \left(\frac{2\pi}{\sqrt{3}a}, \frac{2\pi}{a}\right), \quad \mathbf{b}_2 = \left(\frac{2\pi}{\sqrt{3}a}, -\frac{2\pi}{a}\right), \tag{1.5}$$

with $|\mathbf{b}_1| = |\mathbf{b}_2| = 4\pi/\sqrt{3}a$.

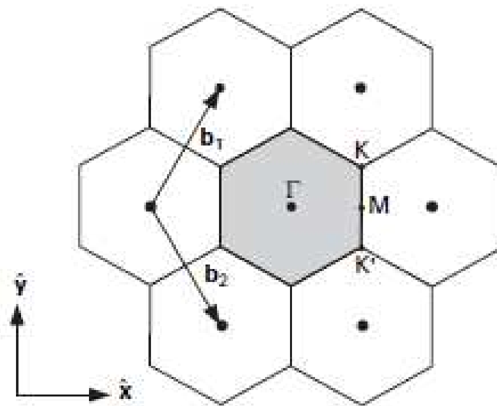

FIGURE 1.4: The reciprocal lattice of graphene. The first Brillouin zone is the shaded hexagon with the high symmetry points labeled as Γ, M, and K.

In the Brillouin zone, which is illustrated as the shaded hexagon in Fig. 1.4, there are three key locations of high symmetry. In Fig. 1.4, these locations are identified by convention as the Γ-point (point located at the center of the hexagon), the M-point (midpoint of the side of the hexagon) and the K-point (corner of the hexagon). The vectors describing the location of the points M and K with respect to the zone center are:

$$\mathbf{\Gamma M} = \left(\frac{2\pi}{\sqrt{3}a}, 0\right), \quad \mathbf{\Gamma K} = \left(\frac{2\pi}{\sqrt{3}a}, \frac{2\pi}{3a}\right). \tag{1.6}$$

There are six K-points and six M-points within the Brillouin zone. Sometimes a distinction is made between the K-point and K'-point (Fig. 1.4), particularly in the discussion of intervalley or interband electron scattering by lattice vibrations, but they are essentially equivalent for most purposes. The unique solutions for the energy bands of crystalline solids are found within the Brillouin zone and sometimes the dispersion is graphed along the high symmetry directions.

1.2.3 Electronic properties

The electronic band structure of graphene is of primary importance because it is the starting point for the understanding of graphene's solid-state properties and analysis of graphene devices and it is also the starting point for the understanding and derivation of the band structure of CNTs.

The band structure of graphene is shown in Fig. 1.5. This band structure was computed numerically from first principles and shows many energy branches resulting from all the π and σ electrons that form the outermost electrons of carbon [8].

There is a limiting technique for obtaining a satisfactory band structure, called the "tight-binding model", that is in good agreement with experimental measurements or more sophisticated numerical ab-initio band structure computations. This model assumes that the outermost electrons are localized (i.e. tightly bound) to their respective atomic cores.

The assumptions belonging to the tight-binding formalism are [4]:

- Nearest neighbor tight-binding (NNTB) model: the wavefunction of an electron in any primitive unit cell only overlaps with the wavefunctions of its nearest neighbours. The nearest neighbors of a type-A atom in the graphene lattice are three equivalent type-B atoms.

- Electron–hole symmetry: a close observation of the ab-initio dispersion in the neighborhood of the Fermi energy (E = 0 eV at the K-point in Fig. 1.5) reveals that the π and π^* branches have similar structure, at least for energies close to the E_F. Within this restricted range, the energy branches are approximately mirror images of each other. Since electrons are the mobile charges in the π^* band and holes are the mobile charges in the π band, this approximation is called "the electron–hole symmetry".

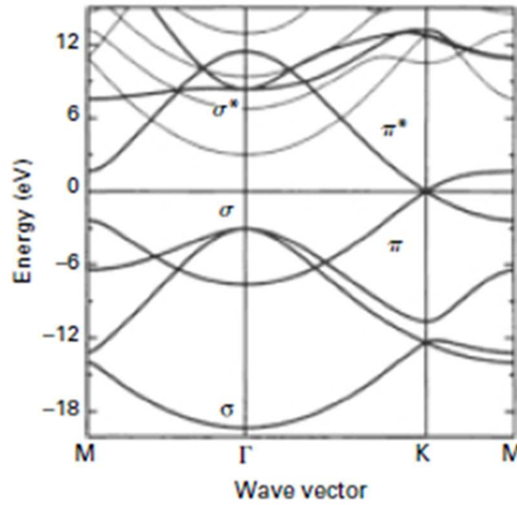

FIGURE 1.5: The ab-initio band structure of graphene, including the σ and π bands. The Fermi energy is set to 0 eV [8].

As a result of the NNTB stipulations, the dispersion relation $E(\mathbf{k})$ is [4,9,10]:

$$E(\mathbf{k})^{\pm} = \pm\gamma\sqrt{1 + 4\cos\frac{\sqrt{3}a}{2}k_x\cos\frac{a}{2}k_y + 4cos^2\frac{a}{2}k_y}, \quad (1.7)$$

where γ , including the nearest neighbor overlap energy, is called " the hopping energy" and it is often used as a fitting parameter to match ab-initio computations or experimental data. Commonly used values for γ range from about 2.7 eV to 3.3 eV.

Comparison of the NNTB dispersion, eq. (1.7), with ab-initio computations for the π bands shows good agreement (Fig. 1.6) with the strongest agreement expectedly at low energies (range within ±1 eV is sometimes considered reasonable) [11]. Much of the exploration of graphene and derived nanostructures such as CNTs has been focused on the low-energy properties.

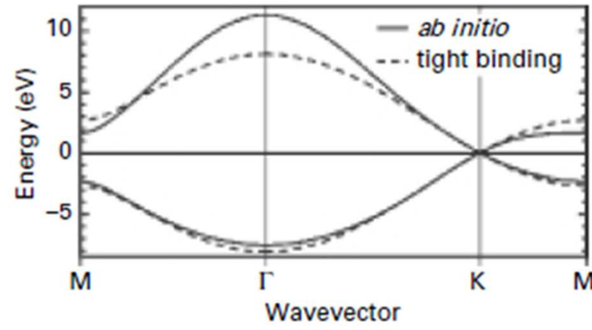

FIGURE 1.6: Comparison of ab-initio and NNTB dispersions of graphene showing good agreement at low energies (energies about the K-point). $\gamma = 2.7\ eV$ is used [11].

Fig. 1.7 shows the 3D plot of the NNTB dispersion throughout the Brillouin zone. The upper half of the dispersion is the conduction (π*) band and the lower half is the valence (π) band. The highest occupied state housing the most energetic electrons are at the K-points, as identified earlier, and the corresponding energy is formally defined as the Fermi energy ($E_F = 0\ eV$). The properties of electrons around the Fermi energy often determine the characteristics of practical electronic devices.

Owing to the absence of a bandgap at the Fermi energy, and the fact that the conduction and valence bands touch at E_F, graphene is considered a semi-metal or zero-bandgap semiconductor, in contrast to a regular metal, where E_F is typically in the conduction band, and a regular semiconductor, where E_F is located inside a finite bandgap. Under non-equilibrium conditions (applied electric or magnetic fields) or extrinsic conditions (presence of impurity atoms), the Fermi energy will depart from its equilibrium value of 0 eV.

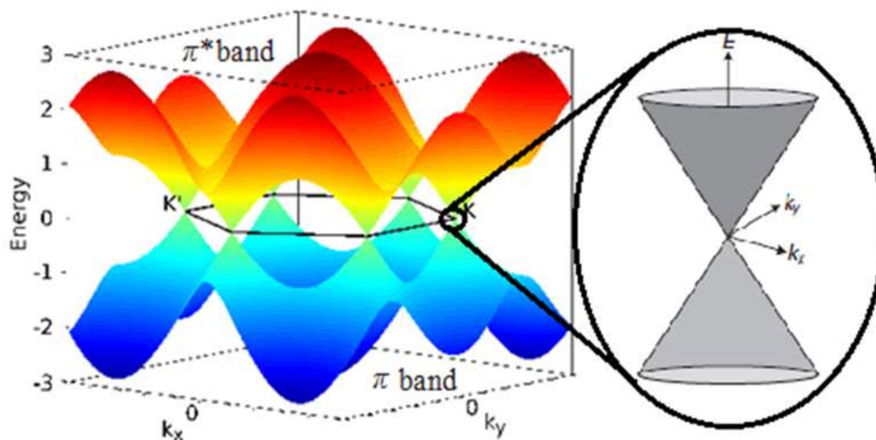

FIGURE 1.7: The nearest neighbor tight-binding band structure of graphene: the π and π* bands are symmetric with respect to the valence and conduction bands. The hexagonal Brillouin zone is superimposed and touches the energy bands at the K-points. The linear dispersion relation close to the K' and K points of the first 2D Brillouin zone gives rise to the “Dirac cones” as shown on the right.

Expanding eq. (1.7) for **k** in the vicinity of **K** (or **K'**), yields a linear dispersion for the π and π^* bands near these six corners of the hexagonal 2D Brillouin zone [1,4,12]:

$$E(\mathbf{k})^{\pm} = \pm\hbar v_F|\mathbf{k}|, \tag{1.8}$$

where:

$$v_F = \frac{\sqrt{3}\gamma a}{2\hbar}, \tag{1.9}$$

is the electronic group velocity, called " the Fermi velocity", and ħ is the reduced Planck's constant. Graphene is thus highly peculiar for this linear energy-momentum relation and electron-hole symmetry. The electronic properties in the vicinity of these corners of the 2D Brillouin zone mimic those of massless Dirac fermions forming "Dirac cones" as illustrated in Fig. 1.7. The six points where the Dirac double cones touch are referred to as the Dirac points. The electronic group velocities close to those points are quite high at ~ 10^6 *m/s*, and within the massless Dirac fermions analogy represent an effective "speed of light" ($v_F \sim c/300$). This behavior is responsible for much of the research attention that graphene has been receiving as platform for investigating the properties of the Dirac fermions and for perspective high-speed electronic applications.

Another important property of graphene is a special feature of the carrier wavefunction which leads to other unusual properties. Due to the two interpenetrating sub-lattices, A and B, carriers near the Dirac point **K**, can be described by a two component wavefunction [10]:

$$\psi_{\pm,\mathbf{K}}(\mathbf{k}) = \frac{1}{\sqrt{2}}\begin{pmatrix} e^{-\frac{i\theta_k}{2}} \\ \pm e^{\frac{i\theta_k}{2}} \end{pmatrix}, \tag{1.10}$$

where $\theta_k = arctan(q_x/q_y)$ and $\mathbf{q} = \mathbf{k}\text{-}\mathbf{K}$ is the momentum measured from the Dirac point **K**. This wavefunction has some interesting implications. For example, electrons along + k_x and - k_x have orthogonal wavefunctions, so there is no probability of backscattering at 180 degrees which favors mobility and enables near ballistic transport at room temperature. The mobility μ, in $cm^2V^{-1}s^{-1}$, is defined both in a diffusive or ballistic regime as the ratio between the conductivity σ and the carrier charge density and is commonly used to characterize the graphene structural quality:

$$\mu = \frac{\sigma}{en}. \tag{1.11}$$

The conductivity (which for a two-dimensional system coincides with the so called "sheet conductance") and the mobility of graphene depend on the microscopic scattering processes that occur in graphene at a given temperature [13-15].

The carrier density n sets the position of the Fermi level, E_F, with respect to the Dirac point. For ideal neutral graphene without free carriers, E_F is located at the Dirac point, where $n \approx 0$ ($n = 0$ at $T = 0$ K). Graphene becomes an n- or p-type conductor when the Fermi level shifts above or below the Dirac point and n corresponds to an excess of electrons or holes, respectively.

The relation between n and E_F can be easily derived considering that the density of states (DOS) in graphene depends linearly on the energy E. Formally, in two dimensions, the total number of states available between an energy E and an interval dE is given by the differential area in k-space dA divided by the area of one k-state $(2\pi)^2/\Omega$, where Ω is the area of the lattice. Mathematically, this is equivalent to [4,14]:

$$N(E)\mathrm{d}E = 2\mathrm{g}_z \frac{\mathrm{d}A}{(2\pi)^2/\Omega}, \tag{1.12}$$

where the factor of two in the numerator is included for spin degeneracy and g_z is the zone degeneracy. There are six equivalent K-points, and each K-point is shared by three hexagons; therefore, $g_z = 6 \cdot 1/3 = 2$ for graphene. To determine dA, let us consider a circle of constant energy in k-space of radius k. The differential area obtained by an incremental increase of the radius by dk is $2\pi k\mathrm{d}k$. Therefore, the DOS, which is always a positive value or zero, is:

$$\mathrm{g}(E) = \frac{N(E)}{\Omega} = \frac{2}{\pi}\left|k\frac{\mathrm{d}k}{\mathrm{d}E}\right| = \frac{2}{\pi}\left|k\left(\frac{\mathrm{d}E}{\mathrm{d}k}\right)^{-1}\right|. \tag{1.13}$$

Substituting from eq. (1.8) yields a linear DOS appropriate for low energies:

$$\mathrm{g}(E) = \frac{2}{\pi(\hbar v_F)^2}|E| = \beta_\mathrm{g}|E|, \tag{1.14}$$

where β_g is a material constant, $\beta_\mathrm{g} \approx 1.5 \cdot 10^6$ $eV^{-2}\mu m^{-2}$ and the absolute value of E is necessary because energy can be either positive (electrons) or negative (holes). At the Fermi energy ($E_F = 0$ eV), the DOS vanishes to zero even though there is no bandgap. This is the reason why graphene is considered a semi-metal in contrast to regular metals that have a large DOS at the Fermi energy.

The equilibrium electron carrier density *n* is [4,12]:

$$n = \int_0^{+\infty} \mathrm{g}(E) f(E) \mathrm{d}E = \frac{2}{\pi}\left(\frac{k_B T}{\hbar v_F}\right) F_1\left(\frac{E_F}{k_B T}\right) \approx \frac{1}{\pi}\left(\frac{E_F}{\hbar v_F}\right)^2, \tag{1.15}$$

where $f(E)$ is the Fermi–Dirac distribution function:

$$f(E) = \frac{1}{1 + e^{(E-E_F)/k_B T}}, \tag{1.16}$$

and $F_1(E_F/k_BT)$ is the so-called "Fermi-Dirac Integral" and the last expression rigorously holds at $T = 0$ *K*. Eq. (1.15) shows that the Fermi level changes as the square root of the carrier density:

$$E_F = \pm \frac{h}{2\sqrt{\pi}} v_F \sqrt{n}, \tag{1.17}$$

where the + and - sign correspond to n and p-type graphene, respectively).

The position of E_F can be varied experimentally either by chemically doping the graphene [16] or by inducing an excess of carriers by means of an electric field generated by an applied bias or a gate [17]. The possibility of controlling the position of the Fermi energy, the sign of the excess carries and hence the conductivity by doping or by a bias/gate is a remarkable feature of graphene and opens the possibility of a new class of electronic devices.

1.2.4 Graphene nanoribbons

Graphene nanoribbons are narrow rectangles made from graphene sheets and have widths on the order of nanometers up to tens of nanometers [4]. The nanoribbons can have arbitrarily long length and, as a result of their high aspect ratio, they are considered quasi-1D nanomaterials. GNRs can have metallic or semiconducting character. GNRs show a departure from the electronic properties of graphene sheets, most notably the opening of a bandgap due to the quantum confinement and edge effects. The opening of a bandgap is of great interest because it unlocks the potential of employing GNRs as transistors.

The band structure of GNRs can be computed numerically using first principles or tight-binding schemes [18]. A useful first-order semi-empirical equation capturing the width dependence of the bandgap E_g has a simple relation:

$$E_g = \frac{\alpha}{w + w_0}, \tag{1.18}$$

where w (nm) is the width of the nanoribbons and w_0 (nm) and α ($eV{\cdot}nm$) are fitting parameters. Experimentally extracted values of α range from 0.2 eV to about 1 eV [19,20]. Experimental and theoretical data suggest a $w_0 \approx 1.5$ nm. As the width of the nanoribbon increases and exceeds about 50 or 100 nm, E_g vanishes and the band structure of GNRs gradually returns to that of a 2D graphene sheet. Fig. 1.8 plots a set of experimentally extracted values for the bandgap confirming the inverse width dependence [19].

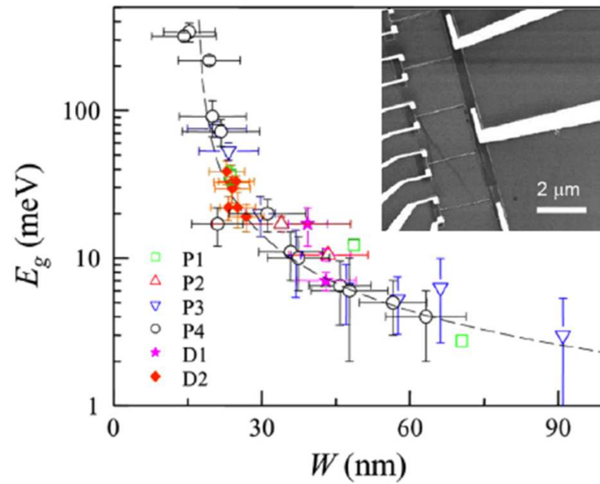

FIGURE 1.8: Experimentally extracted bandgap versus width for GNRs [19].

1.2.5 Transport properties

At the Dirac point, even at cryogenic temperatures when n and σ should tend to zero, the conductivity of graphene remains finite [12]. This is a consequence of the intrinsic properties of the 2D Dirac fermions, which set a limit on the minimum attainable conductivity. In short and wide strips (width to length ratio $W/L \gg 1$) of ideal graphene, with no impurities or defects and for $T \rightarrow 0K$, transport at the Dirac point is explained as propagation of charge carriers via evanescent waves (tunneling between the leads) [21]. Under these conditions, the minimum of conductivity can reach the universal minimum value:

$$\sigma_{Dirac} = \frac{4e^2}{\pi h}, \tag{1.19}$$

regardless of the edges of the graphene strip. Experimental confirmation of the ballistic transport and the universal minimum conductivity in graphene was provided by low-temperature transport spectroscopy on single-layers and bilayers [22] and through measurements of shot noise at low frequency in field effect devices (200 *nm* long and with $W/L = 24$) at temperatures around 4.2 *K* [23]. When the effect of graphene edges cannot be neglected ($W/L<3$) or at the presence of disorder which locally affects the density of carriers, the evanescent states are accompanied by propagating states and the minimum conductivity rapidly increases [24]. Due to the fabrication process, graphene usually contains various sources of disorder, as defects, impurities, strong interaction with charges in surrounding dielectrics, phonons, etc. This disorder causes spatial inhomogeneities in the carrier density. Local accumulations of charge carriers, so called electron-hole puddles [25], produce percolation paths for carrier transport and prevent the transition to the ideal minimum conductivity state at the Dirac point. Hence, for real graphene the measured conductivity at cryogenic temperatures is much higher than the universal minimum value, changes from sample to sample and is typically in the range 2÷5 e^2/h on good quality samples [26-28].

At higher carrier density, i.e. away from the Dirac point, the mentioned disorder sources, acting as scattering centers, reduce the electron mean free path. Two transport regimes are often considered depending on the mean free path length l with respect to the graphene length L. When $l > L$, transport is ballistic since carriers can travel through graphene at Fermi velocity v_F without scattering. On the other hand, when $l < L$, transport is diffusive since carriers undergo elastic and inelastic collisions. In both cases, transport can be described by the Landauer formalism [29] and the conductivity can be expressed as:

$$\sigma = \frac{L}{W}\frac{2e^2}{h}\int_0^\infty T(E)M(E)\left(-\frac{\partial f}{\partial E}\right)dE, \tag{1.20}$$

with $T(E)$ the transmission function and $M(E)$ the number of conducting channels.
For ballistic transport:

$$T(E) = 1, \tag{1.21}$$

while for diffusive transport:

$$T(E) = \frac{\lambda(E)}{\lambda(E) + L}, \tag{1.22}$$

where L is the length of the sample and $\lambda(E)$ is the energy-dependent scattering mean free path.

$M(E)$ can be calculated [14] from the dispersion relation eq. (1.8), and, similarly to the density of states, has a linear dependence on the energy E:

$$M(E) = W\frac{2|E|}{\pi\hbar v_F}. \tag{1.23}$$

From eqs. (1.20)-(1.23), under the approximation that $-\partial f/\partial E \approx \delta(E-E_F)$ valid for $T \rightarrow 0K$, a simple expression of graphene conductivity can be easily obtained:

$$\sigma = \frac{2e^2}{h}\left(\frac{2E_F}{\pi\hbar v_F}\right)\lambda(E_F). \tag{1.24}$$

In eq. (1.24), $\lambda = L$, independent of the energy E in the ballistic regime, and:

$$\lambda(E) = \frac{\pi}{2}v_F\tau(E), \tag{1.25}$$

in the diffusive regime, where $\tau(E)$ is the momentum relaxation time, i.e. the average time between scattering events.

Recalling eq. (1.11) and the E_F vs. n relation of eq. (1.17), eq. (1.24) implies that $\sigma \propto \sqrt{n}$ and $\mu \propto 1/\sqrt{n}$ in the ballistic regime. This dependence, which is sketched in Fig. 1.9, has been experimentally observed on clean graphene [30].

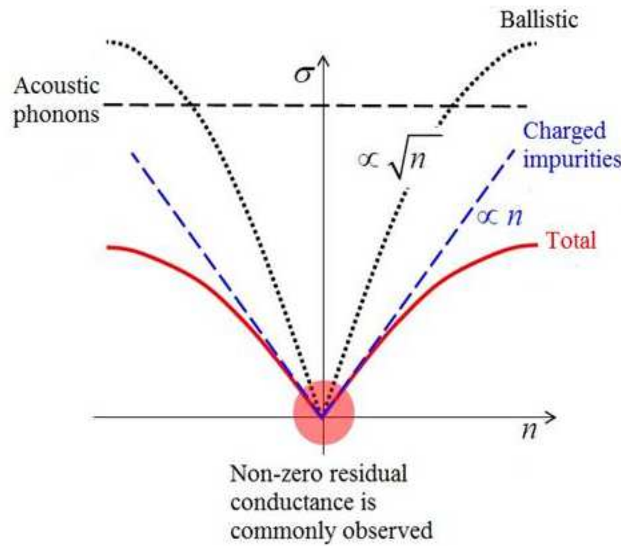

FIGURE 1.9: Conductivity vs. carrier density (σ vs. n) for graphene. Acoustic phonons (short range) and ionized impurity (long range) scattering are considered [12].

In the diffusive regime, $\lambda(E)$ and $\tau(E)$ depend on the scattering mechanism. In graphene, three main scattering mechanisms are considered: Coulomb scattering by charged impurities (long range scattering), short-range scattering (defects, adsorbates), and electron-phonon scattering.

Charged impurity scattering is a very important scattering mechanism [30]. It is caused by the presence of charged impurities close to the graphene sheet. These impurities can be trapped ions in the top or bottom dielectric or ions on the graphene surface. Coulomb scattering is more relevant at low energies and the relaxation time corresponding to it varies linearly with energy, $\tau(E) \propto E$ [31,32]. According to eqs. (1.11), (1.17), (1.24) and (1.25), $\sigma \propto n$ and the mobility is independent of n. The observation of a linear σ vs. n plot (Fig. 1.9) is frequently taken as evidence for the presence of charged impurity scattering.

Short range scattering potential is due to localized defects as vacancies and cracks [31,33]. The resulting scattering rate is proportional to the final density of states, so $1/\tau(E) \propto E$, and is independent of temperature. Hence, for this scattering mechanism, the conductivity does not depend on n and $\mu \propto 1/n$.

Deformation potential scattering by acoustic phonons [33-35] is another important scattering mechanism. Phonons can be considered an intrinsic scattering source since they limit the mobility at finite temperature even when there are no defects. Longitudinal acoustic (LA) phonons are known to have a higher electron-phonon scattering cross-section. The scattering of electrons by LA phonons can be considered quasi-elastic since the phonon energies are negligible in comparison with the Fermi energy of electrons. Optical phonons in the graphene can also scatter carriers, especially at temperatures above 300 K, and are believed to be responsible for the decrease in conductivity at high temperatures [36]. Phonon scattering is usually invoked to explain the temperature dependence of σ but it does not introduce any dependence on n (Fig. 1.9) .

Other scattering mechanisms can affect the conductivity. Different scattering mechanisms add up to produce a total conductivity σ_{Tot} given by:

$$\frac{1}{\sigma_{Tot}} = \frac{1}{\sigma_1} + \frac{1}{\sigma_2} + \cdots, \tag{1.26}$$

where σ_i is the conductivity corresponding to a given scattering mechanism. According to eq. (1.26), the smaller σ_i limits the total σ_{Tot}. An example is given in Fig. 1.9 where acoustic phonons and charged impurities are considered.

1.2.6 Optical properties

Graphene has remarkable optical properties. The gapless energy band enables charge carrier generation by light absorption over a very wide energy spectrum, unmatched by any other material [12]. This includes the ultraviolet, visible, infrared (*IR*) and terahertz (*THz*) spectral regimes. In the near-*IR* and visible, light transmittance T of graphene does not depend on frequency, being controlled by the fine structure constant $\alpha = e^2/(4\pi\varepsilon_0\hbar^2 c)$ [37] . At normal incidence, the transmittance can expressed as [38]:

$$T = (1 - 0.5\pi\alpha)^2 \approx 1 - \pi\alpha \approx 0.977. \quad (1.27)$$

Considering the thickness of 0.334 nm, a single-layer of suspended graphene has an unusually high absorption of $A = 1\text{-}T \approx 2.3\%$, corresponding to an absorption coefficient about 50 times higher than for example the absorption of GaAs at $\lambda = 1.55$ μm and it demonstrates the strong coupling of light and graphene, which can be exploited for conversion of photons into electrical current or voltage [39,40]. Because graphene sheets behave as a 2-D electron gas, they are optically almost noninteracting in superposition, and the absorbance of few-layer graphene sheets is roughly proportional to the number of layers. The proportionality is gradually lost and the transparency remains quite high while adding further layers: graphene layers corresponding to a thickness of 1 μm still have a transparency of approximately 70% [41].

In addition, the reflectivity of graphene is very low: $R = 0.25\pi^2\alpha^2(1\text{-}A) = 1.3\times10^{-4}$, though it increases to 2% for 10 layers [42].

1.3 Carbon nanotubes

Carbon nanotubes (CNTs) are graphitic sheets curled up into seamless cylinders. There are two families of CNTs, namely single-wall CNTs (SWCNTs) and multi-wall CNTs (MWCNTs). A SWCNT (Fig. 1.10(a)) is a hollow cylindrical structure of carbon atoms with a diameter that ranges from about 0.5 to 5 *nm* and lengths of the order of micrometers to centimeters. An MWCNT (Fig. 1.10(b)) is similar in structure to a SWCNT but has multiple concentric cylindrical walls with the spacing between walls comparable to the interlayer spacing in graphite, approximately 0.34 *nm* [4].

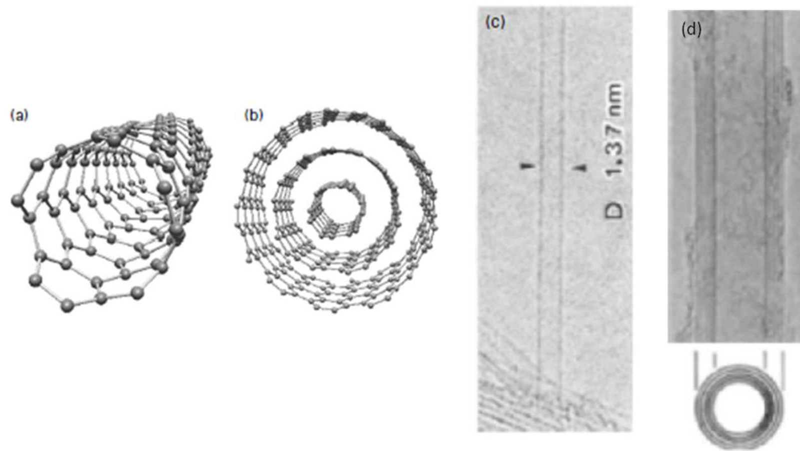

FIGURE 1.10: On the left: ball-and-stick models of a SWCNT (a) and a MWCNT (b). The balls represent the carbon atoms and the sticks stand for the bonds between carbon atoms. On the right: high-resolution TEM images of single-wall and multi-wall CNTs observed by Sumio Iijima [44,45].

The large aspect ratio makes the nanotubes nearly ideal one-dimensional (1-D) objects. There are three types of SWCNT: chiral CNTs, armchair CNTs, and zigzag CNTs, of which the latter two are achiral. Depending on the detailed arrangement of the carbon atoms the SWCNTs can be metallic or semiconducting [43]; instead the MWCNTs are usually metallic.

MWCNTs were observed for the first time in transmission electron microscopy (TEM) studies by Iijima in 1991 [44], while SWCNTs were produced independently by Iijima [45] and Bethune [46] in 1993. Fig. 1.10(c) and Fig. 1.10(d) show the TEM images of single-wall and multi-wall CNTs observed by Sumio Iijima.

1.3.1 The direct lattice

To understand the origin of the different types of CNT, we start from the direct lattice of graphene and then define a mathematical construction which folds graphene's lattice into a CNT. This construction directly leads to a precise determination of the primitive lattice of carbon nanotubes, which is required information in order to derive the CNT band structure.

With reference to Fig. 1.11(a), that shows the honeycomb lattice of graphene, a single-wall CNT can be conceptually conceived by considering folding the dashed line containing primitive lattice points A and C with the dashed line containing primitive lattice points B and D such that point A coincides with B, and C with D to form the nanotube shown in Fig. 1.11(b) [4].

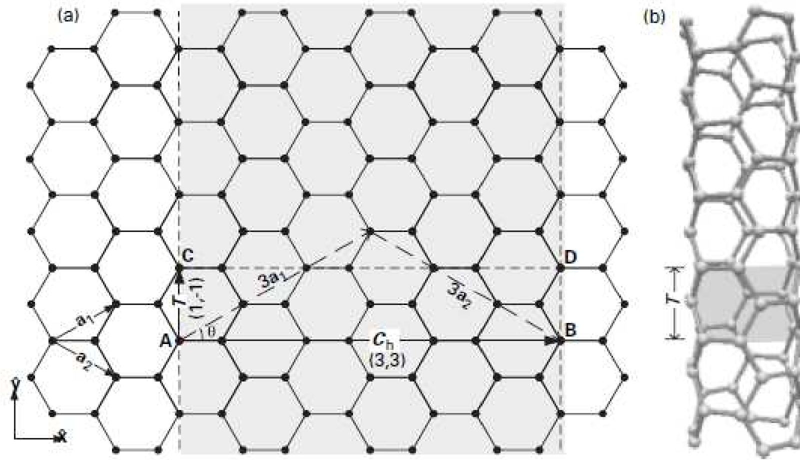

FIGURE 1.11: An illustration to describe the conceptual construction of a CNT from graphene. (a)Wrapping or folding the dashed line containing points A and C to the dashed line containing points B and D results in the (3,3) armchair carbon nanotube in (b). The CNT primitive unit cell is the cylinder formed by wrapping line AC onto BD and is also highlighted in (b).

The CNT is characterized by three geometrical parameters, the chiral vector $\mathbf{C}_h$, the translation vector $\mathbf{T}$, and the chiral angle θ, as shown in Fig. 1.11(a).

$\mathbf{C}_h$ is defined as the vector connecting any two primitive lattice points of graphene such that when folded into a nanotube these two points are coincidental or indistinguishable, and $|\mathbf{C}_h|$ is the CNT circumference. $\mathbf{C}_h$ is equivalent to:

$$\mathbf{C}_\mathrm{h} = n\mathbf{a}_1 + m\mathbf{a}_2, \tag{1.28}$$

where $\mathbf{a}_1$ and $\mathbf{a}_2$ are the primitive lattice vectors defined by eq. (1.1), n and m are positive integers.

The type of CNT can be deduced directly from the values of the chiral vector and it is described as an (n, m) CNT. The (n, n) CNTs are armchair nanotubes, the (n, 0) CNTs are zigzag nanotubes and all other (n, m) CNTs lead to chiral nanotubes.

The other two geometrical parameters (T and θ) can be derived from the chiral vector. The chiral angle is the angle between the chiral vector and the primitive lattice vector $\mathbf{a}_1$:

$$cos\theta = \frac{\mathbf{C}_\mathrm{h} \cdot \mathbf{a}_1}{|\mathbf{C}_\mathrm{h}||\mathbf{a}_1|}. \tag{1.29}$$

Unique values of the chiral angle are restricted to $0° \leq \theta \leq 30°$. All armchair nanotubes have a chiral angle of 30° and $\theta = 0°$ for all zigzag nanotubes.

The translation vector **T** defines the periodicity of the lattice along the tubular axis and it is the smallest graphene lattice vector perpendicular to $\mathbf{C}_h$.
Let $\mathbf{T} = t_1\mathbf{a}_1 + t_2\mathbf{a}_2$, where t_1 and t_2 are integers. Therefore:

$$\mathbf{C}_\mathrm{h} \cdot \mathbf{T} = t_1(2n+m) + t_2(2m+n) = 0. \tag{1.30}$$

The acceptable solution for eq. (1.30) is:

$$\mathbf{T} = \left(\frac{2m+n}{g_d}, -\frac{2n+m}{g_d}\right), \tag{1.31}$$

where g_d is the greatest common divisor of $2m + n$ and $2n + m$.

The chiral and translation vectors define the primitive unit cell of the CNT, which is a cylinder with diameter $d_t = |\mathbf{C}_\mathrm{h}|/\pi$ and length $|\mathbf{T}| = \sqrt{3}|\mathbf{C}_\mathrm{h}|/g_d$ (Fig. 1.11(b).

1.3.2 Brillouin zone

The wavevectors defining the CNT first Brillouin zone are the reciprocals of the primitive unit cell vectors given by the reciprocity condition [4]:

$$e^{i(\mathbf{K}_\mathrm{a}+\mathbf{K}_\mathrm{c})\cdot(\mathbf{C}_\mathrm{h}+\mathbf{T})} = 1, \tag{1.32}$$

where $\mathbf{K}_\mathrm{a}$ is the reciprocal lattice vector along the nanotube axis and $\mathbf{K}_\mathrm{c}$ is along the circumferential direction, both given in terms of the reciprocal lattice basis vectors of graphene defined by eq. (1.5). Eq. (1.32) simplifies to:

$$\mathbf{C}_\mathrm{h} \cdot \mathbf{K}_\mathrm{c} = 2\pi, \qquad \mathbf{T} \cdot \mathbf{K}_\mathrm{c} = 0, \qquad \mathbf{C}_\mathrm{h} \cdot \mathbf{K}_\mathrm{a} = 0, \qquad \mathbf{T} \cdot \mathbf{K}_\mathrm{a} = 2\pi. \tag{1.33}$$

By the periodic boundary conditions on the Bloch wave functions, the allowed wavevectors k within the Brillouin zone along the axial direction are:

$$k = \frac{2\pi}{N_{uc}T} l, \qquad l = 0,1, \dots, N_{uc} - 1, \tag{1.34}$$

where N_uc is the number of unit cells in the nanotube of length $L_\mathrm{t} = N_\mathrm{uc}T$. The maximum integer value of l is determined from the requirement that unique solutions for k are restricted to the first Brillouin zone, i.e. maximum $k < |\mathbf{K}_\mathrm{a}| = 2\pi/T$. In the limit where the CNT is very

long, for instance $L_t \gg T$ or $N_{uc} \gg 1$, then the spacing between k-values vanishes and k can be considered a continuous variable along the axial direction:

$$k = \left(-\frac{\pi}{T}, \frac{\pi}{T}\right), \tag{1.35}$$

where the wavevector has been re-centered to be symmetric about zero consistent with standard Brillouin zone convention.

Applying the periodic boundary conditions to determine the allowed wavevectors q along the circumferential direction yields:

$$q = \frac{2\pi}{C_h} j = j|\mathbf{K}_c|, \qquad j = 0,1, \dots, N-1, \tag{1.36}$$

where N is the number of hexagons per unit cell.

We observe that the q-values are separated by a gap that is much greater than the spacing in k-values, i.e. $2\pi/C_h \gg 2\pi/L_t$ for long CNTs with lengths $L_t \gg C_h$. Therefore, the q variable is quantized or discretely spaced compared with the relatively continuous k variable, which implies that the allowed CNT wavevectors in the Brillouin zone are composed of a series of lines, as shown in Fig. 1.12. These lines are basically 1D cuts of graphene's reciprocal lattice.

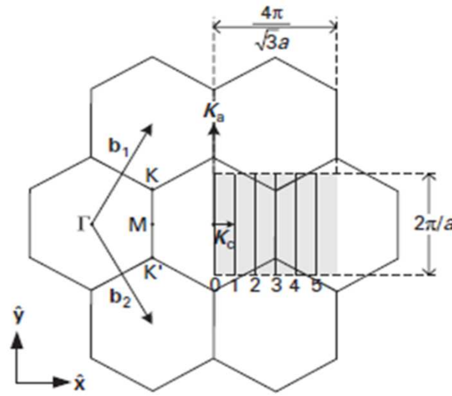

FIGURE 1.12: Brillouin zone of a (3, 3) armchair CNT (shaded rectangle) overlaid on the reciprocal lattice of graphene. The numbers refer to j = 0, 1, ... , 5 for a total of N = 6 1D bands in the CNT Brillouin zone.

Finally, the expression for any arbitrary allowed wavevector within the Brillouin zone is:

$$\mathbf{k} = k\frac{\mathbf{K}_a}{2\pi/T} + j\mathbf{K}_c, \quad \left(j = 0,1, \dots, N-1 \quad \text{and} \quad -\frac{\pi}{T} < k < \frac{\pi}{T}\right), \tag{1.37}$$

where each value of j corresponds to a line with wave vectors k ranging from $-\pi/T$ to $+\pi/T$.

1.3.3 Electronic and transport properties

The electronic structure and electrical properties of SWCNTs are usually discussed in terms of the electronic structure of graphene [4,47]. Fig. 1.15(a) shows the band structure and the hexagonal first Brillouin zone of graphene. The energy bands of CNTs are line cuts or cross-sections of the bands of graphene and the entire Brillouin zone of CNTs can be folded into the first Brillouin zone of graphene. When these cuts pass through a Dirac point, the nanotube is metallic (Fig. 1.13(b)); in cases where no cut passes through a K point, the nanotubes are semiconducting (Fig. 1.13(c)).

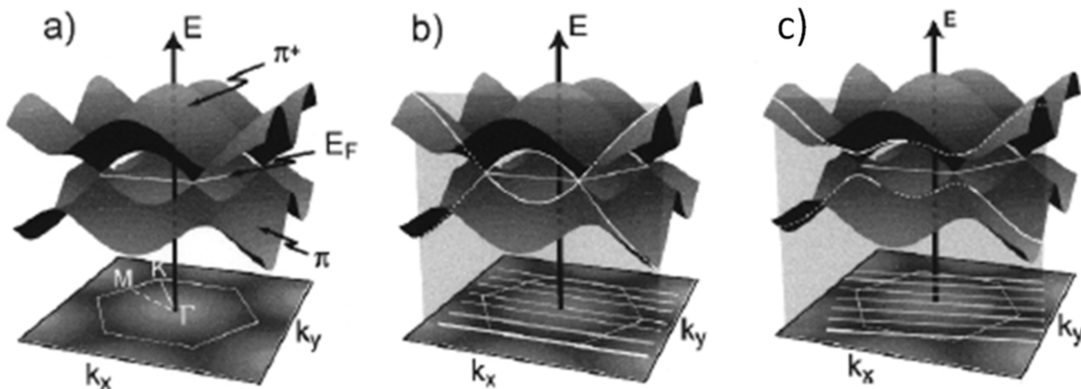

FIGURE 1.13: (a) Band structure of a graphene sheet (top) and the first Brillouin zone (bottom). (b) Band structure of a metallic (3,3) CNT. (c) Band structure of a (4,2) semiconducting CNT. The allowed states in the nanotubes are cuts of the graphene bands indicated by the white lines. If the cut passes through a K point, the CNT is metallic; otherwise, the CNT is semiconducting.

It can be shown that an (n,m) CNT is metallic when $n = m$ and when $n\text{-}m = 3i$ [48], where i is an integer, while CNTs with $n\text{-}m \neq 3i$ are semiconducting [49,50].

The band structure of CNTs can be computed by inserting the allowed wavevectors, given by eq. (1.37) and rewritten in terms of its $\hat{\mathbf{x}}$ and $\hat{\mathbf{y}}$ components.

In general, for any (n, m) CNT, there will be N valence bands ($E \leq 0$) and N conduction bands ($E \geq 0$). Each one of the bands has $2N_{uc}$ allowed states, where the factor of 2 is due to spin degeneracy. At equilibrium the valence bands will be fully occupied and the conduction bands empty with the Fermi energy $E_F = 0$ eV.

Fig. 1.14 shows the band structures for (10, 4) metallic and (10, 5) semiconducting chiral CNTs [4].

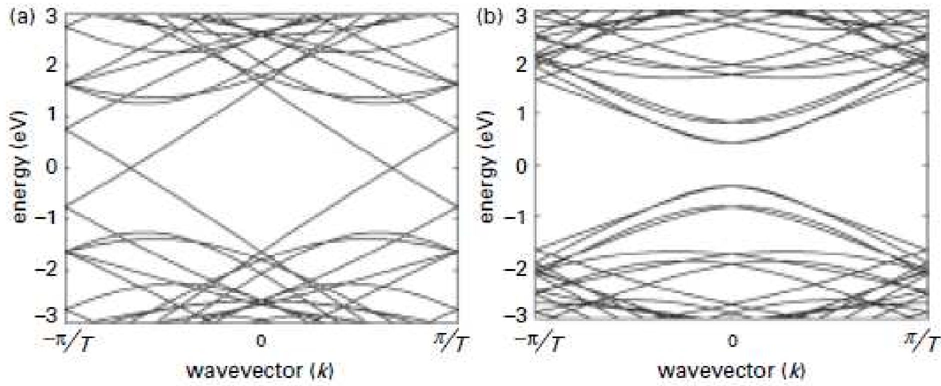

FIGURE 1.14: Band structures for (a) (10, 4) metallic CNT and (b) (10, 5) semiconducting CNT, within ±3 *eV*. The metallic CNT shows a band degeneracy at 0 *eV* and $k = \pm 2\pi/3T$. The semiconducting CNT has a bandgap of ∼ 0.86 *eV*.

Fig. 1.15 shows the band structure for an (8,8) armchair CNT, revealing an energy degeneracy at $ka = \pm 2\pi/3$, where the valence band touches the conduction band [4].

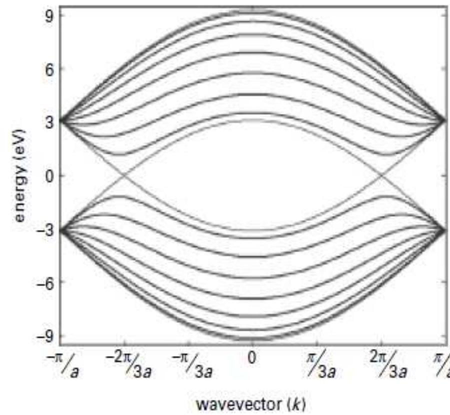

FIGURE 1.15: Band structure for (8, 8) armchair nanotube. For all armchair CNTs, the valence band touches the conduction band at $ka = \pm 2\pi/3$, which explains their metallic properties.

In general, the energy degeneracy at 0 *eV* is common to all armchair CNTs and, hence, armchair CNTs are metallic.

For armchair CNTs, the first subbands of the valence and conduction bands have a linear dispersion at low energies and to a good approximation can be approximated in a simple manner with a linear $E{-}k$ relation independent of chirality. The linear dispersion for the right-half of the Brillouin zone can be expressed as:

$$E(k)^{\pm} \approx \pm \hbar v_F \left| k - \frac{2\pi}{3a} \right|, \quad \left(\frac{\pi}{3a} < k < \frac{\pi}{a} \right), \tag{1.38}$$

where ħ is the reduced Planck's constant and v_F is the Fermi velocity.

Fig. 1.16 shows the band structures for (12, 0) metallic and (13, 0) semiconducting zigzag CNTs [4].

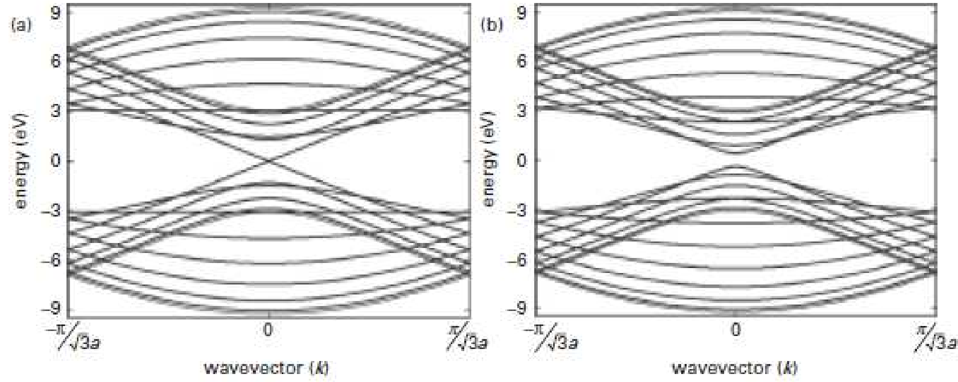

FIGURE 1.16: Band structures for (a) (12, 0) and (b) (13, 0) zigzag CNTs. The (12, 0) CNT is metallic, while the (13, 0) CNT is semiconducting due to the bandgap at $k = 0$.

In general, when n is a multiple of 3, the zigzag CNT is metallic, otherwise it is semiconducting.

For metallic zigzag CNTs, a simple linear $E{-}k$ relation can accurately describe the first subband of the valence and conduction bands. Similar to graphene's linear dispersion, the linear dispersion for the first subband of metallic zigzag CNTs can be expressed as:

$$E(k)^{\pm} \approx \pm\hbar v_F |k|. \tag{1.39}$$

The bandgap for semiconducting CNTs is [4,49]:

$$E_{\mathrm{g}} \approx 2\gamma \frac{a_{c-c}}{d_t}, \tag{1.40}$$

where γ is the hopping energy, $a_{\text{c-c}}$ is the carbon–carbon bond length and d_t is the diameter of the CNT. Numerically, $E_g(eV) \sim 0.9/d_{\mathrm{t}}\,(nm)$.

The CNT electronic structure has many 1D subbands; as such, the total DOS g_{tot} at a given energy is the sum of the contributions from the DOS of each subband [4]:

$$\mathrm{g}_{tot}(E) = \sum_{j=1}^{N} \mathrm{g}(E, j). \tag{1.41}$$

where N is the number of subbands in the CNT band structure.

In a 1D solid, the number of states between E and $E + \mathrm{d}E$ is the differential wave vector $\mathrm{d}k$ normalized to the length of one state:

$$\mathrm{g}(E)\,\mathrm{d}E\,L = 2\frac{\mathrm{d}k}{2\pi/L}, \tag{1.42}$$

where L is the length of the 1D system and $2\pi/L$ is the length of one k-state; the factor of 2 in the numerator accounts for spin degeneracy. Hence, it follows that a general formula for the electron DOS in a 1D solid is:

$$\mathrm{g}(E) = \frac{1}{\pi}\frac{\mathrm{d}k}{\mathrm{d}E}. \tag{1.43}$$

For example, we report the DOS for zigzag (n, 0) nanotubes. Owing to mirror symmetry of the $E{-}k$ relationship, the DOS for the negative branch of the wavevector is identical to the DOS for the positive branch and the complete DOS for the jth subband is [4]:

$$\mathrm{g}_{zz}(E,j) = \frac{4\alpha}{\sqrt{3}\alpha\pi}\frac{|E|}{\sqrt{(E^2 - E_{vh1}^2)(E_{vh2}^2 - E^2)}}, \tag{1.44}$$

where α accounts for the Brillouin zone mirror symmetry or degeneracy and E_{vhi} (i = 1,2) is known as a van Hove singularity (VHS) [4]. Specifically, $\alpha = 1$ if E is energy at the Brillouin zone center (since the Γ-point center is common to both branches of the wavevector), otherwise $\alpha = 2$.

The DOS for semiconducting and metallic zigzag nanotubes are shown in Fig. 1.17. A noteworthy insight is that the square of the energy terms in the denominator of the expression for the DOS is due to the electron–hole symmetry present in the NNTB band structure of CNTs leading to mirror symmetry between the conduction and valence bands' DOS visually evident in Fig. 1.17.

The SWCNTs are 1-D objects and as such their two-terminal conductance is given by Landauer's equation [50-52]:

$$G = \left(\frac{2e^2}{h}\right)\sum_{i}^{Nch} T_i, \tag{1.45}$$

where $2e^2/h$ is the quantum of conductance, T_i is the transmission of a contributing conduction channel (subband), and the sum involves all contributing conduction channels, i.e., channels whose energy lies between the electrochemical potentials of the left and right reservoirs to which the nanotube is connected.

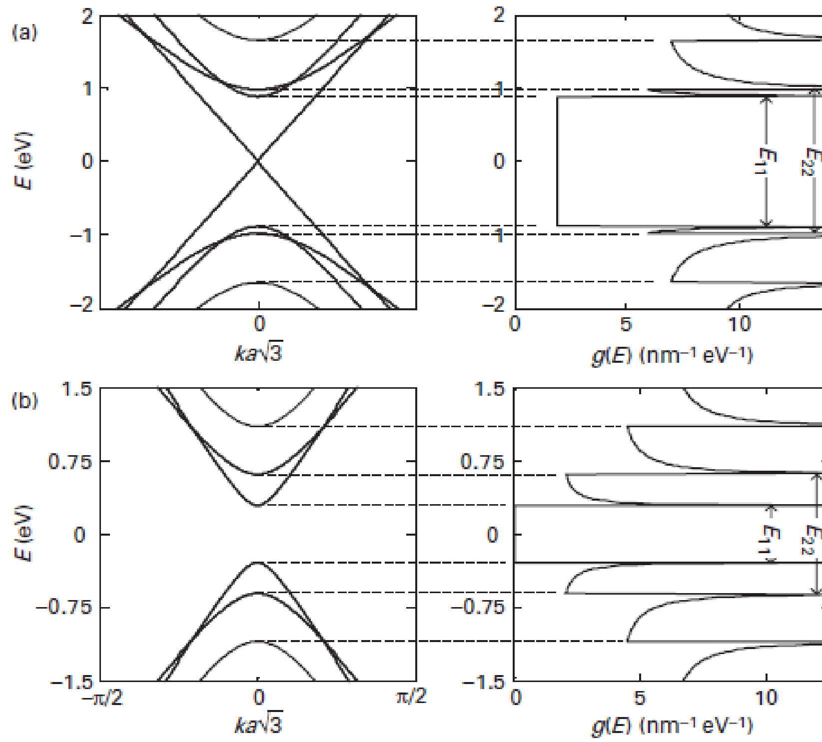

FIGURE 1.17: The electronic DOS for (a) metallic and (b) semiconducting zigzag nanotubes. For metallic (semiconducting) nanotubes, the DOS around 0 eV is non-zero (zero).

In the absence of any scattering, i.e., when all $T_i = 1$, the resistance of a metallic SWCNT is $(h/4e^2) \approx 6.5\ k\Omega$, because for the lowest subband in metallic CNTs the number of degenerate subbands is $N_{ch} = 2$ [4]. This quantum mechanical resistance is a contact resistance arising from the mismatch of the number of conduction channels in the CNT and the macroscopic metal leads.

There is strong evidence that $T_i = 1$ in the case of metallic SWCNTs, so that these tubes behave as ballistic conductors [53–56]. This arises from the 1-D confinement of the electrons which allows motion in only two directions. This constraint along with the requirements for energy and momentum conservation severely reduces the phase space for scattering processes. However, in addition to the quantum mechanical contact resistance, there are other sources of contact resistance, such as those produced by the existence of metal-nanotube interface barriers, or poor coupling between the CNT and the leads. These types of resistance are very important and can dominate electrical transport in nanotubes [56].

Unlike SWCNTs, the electrical properties of MWCNTs have received less attention. This is due to their complex structure (every carbon shell can have different electronic character and chirality) and the presence of shell–shell interactions [57,58]. However, at low bias and temperatures, and when MWCNTs are side-bonded to metallic electrodes, transport is dominated by outer-shell conduction [59,60].

1.4 Theory of the field emission

Controlled propagation of electrons in vacuum is at the basis of several technological applications, like CRT displays, vacuum electronics, electron microscopy, X-ray generation, electron beam lithography, etc. The most common technique to extract electron from matter is thermionic emission, where electrons are emitted from heated filaments (hot cathodes), which requires a source heated at high temperature(~1000 $^{\circ}C$) and has several drawbacks. Field emission (FE), which involves extraction of electrons from a conducting solid (metal or highly doped semiconductor) by an external electric field, is becoming one of the best alternatives. Indeed, by this method, an extremely high current density with low energy spread of the emitted electrons and with negligible power consumption can be achieved [61-63].

The phenomenon of field emission is associated with a quantum mechanical tunneling process whereby electrons near the Fermi level tunnel through a (material dependent) potential barrier, whose width is reduced by the application of an external electric field, and escape to the vacuum level (Fig. 1.18) [64].

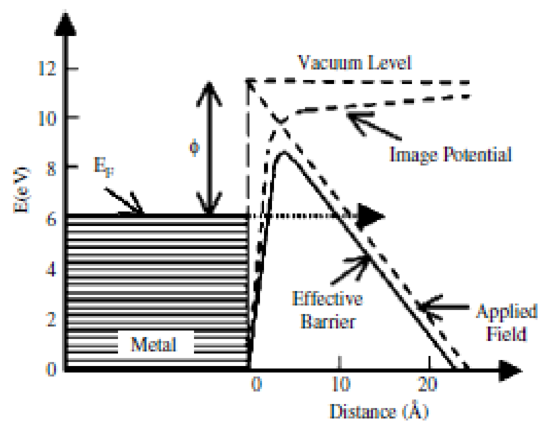

FIGURE 1.18: Potential-energy diagram illustrating the effect of an external electric field on the energy barrier for electrons at a metal surface [64].

For a parallel flat electrode configuration the field is off the order of 10^9 *V/m*. However, if the cathode surface has a high point or a protrusion, electrons may be extracted at a considerably lower applied field [62,65]. This is because the lines of force converge at the sharp point and the physical geometry of the tip provides a field enhancement.

The emission current depends on the electric field at the emitter surface (referred as microscopic or local electric field), E_S, and on the workfunction, Φ, i.e. the effective surface-

vacuum barrier height. The Fowler–Nordheim model [66], derived for a flat metallic surface at 0 *K* and assuming a triangular potential barrier, predicts an exponential behaviour of the emitted current:

$$I = a\frac{E_S^2}{\Phi}S \cdot exp\left(-b\frac{\Phi^{3/2}}{E_s}\right), \quad (1.46)$$

where *S* is the emitting surface area, E_S is the uniform electric field on that surface and *a* and *b* are constants. When *S* is expressed in cm^2, Φ and E_S respectively in *eV* and *V/cm*, $a = 1.54 \cdot 10^{-6}\ A \cdot eV \cdot V^{-2}$ and $b = 6.83 \cdot 10^{9}\ eV^{-3/2} \cdot V \cdot m^{-1}$.

In a parallel plate configuration, the field E_S can be obtained from the applied potential *V* and the inter-electrode distance *d* as $E_S = V/d$. If the cathode surface has a protrusion, a field enhancement factor, β, which takes into account the amplification occurring around the tip, has to be introduced and:

$$E_s = \frac{\beta V}{d}. \quad (1.47)$$

According to eqs. (1.46) and (1.47), a Fowler–Nordheim plot of $ln(I/V^2)$ as a function of $1/V$ is a straight line, whose slope, $m = b\Phi^{3/2}d/\beta$, and interception, $y_0 = ln(aS\beta^2/\Phi d^2)$, can, in principle, be used to estimate β and Φ. Although corrections [67,68] are required to describe effects of non-zero temperature, series resistance, extremely curved surfaces and non-uniform field enhancement factors or workfunctions, the basic FN theory has proven to be a good model to achieve a first-approximation understanding of the emission phenomena. For temperatures up to several hundred degree Celsius and fields in a large window, F–N model provides a good fitting to the *I–V* characteristics of several kind of emitters.

Bibliography

[1] Foa Torres L E F, Roche S and Charlier J C *Introduction to Graphene-Based Nanomaterials*, 2014 Cambridge University Press, New York.

[2] Frankand I W , Tanenbaum D M, vanderZande A M and McEuen P L 2007 *J. Vac. Sci. Technol. B* **25** 2558-2561.

[3] Lee C, Wei X, Kysar J W and Hone J 2008 *Science* **321** 385-388.

[4] Wong H S P and Akinwande D *Carbon Nanotube and Graphene Device Physics* 2011 Cambridge University Press, New York.

[5] Novoselov K S, Geim A K, Morozov S V, Jiang D, Zhang Y, Dubonos S V, Grigorieva I V and Firsov A A 2004 *Science* **306** 666-669.

[6] Geim A K, Morozov S V, Jiang D, Katsnelson M I, Grigorieva I V, Dubonos S V and Firsov A A 2005 *Nature* **438** 197-200.

[7] Geim A K and Novoselov K S 2007 *Nat. Mater.* **6** 183–91.

[8] Machón M, Reich S, Thomsen C, Sánchez-Portal D and Ordejón P 2002 *Phys. Rev. B* **66** 155410.

[9] Das Sarma S, Adam S, Hwang E K and Rossi E 2011 *Rev. Mod. Phys.* **83** 407–470.

[10] Castro Neto A H, Guinea F, Peres N M R, Novoselov K S and Geim A K 2009 *Rev. Mod. Phys.* **81** 109-162.

[11] Reich S, Maultzsch J and Thomsen C 2002 *Phys. Rev. B* **66** 35412.

[12] Di Bartolomeo A 2016 *Physics Reports* **606** 1-58.

[13] Cooper D R, D'Anjou B, Ghattamaneni N, Harack B, Hilke M, Horth A, Majlis N, Massicotte M, Vandsburger L, Whiteway E and Yu V 2012 I*nternational Scholarly Research Network ISRN Condensed Matter Physics* **2012** 501686.

[14] Lundstrom M and Jeong C *Near-equilibrium transport* 2013 World Scientific,Singapore.

[15] Chen J H, Cullen W G, Jang C, Fuhrer M S and Williams E D 2009 *Physical Review Letters* **102** 236805.

[16] Oh J S, Kim K N and Yeom G Y 2014 *J. Nanosci. Nanotechnol.* **14** 1120-1133.

[17] Yu Y J, Zhao Y, Ryu S, Brus L E, Kim K S and Kim P 2009 *Nano Lett.* **9** 3430–3434.

[18] Son Y W, Cohen M L and Louie S G 2006 *Phys. Rev. Lett.* **97** 089901.

[19] Han M Y, Ozyiluaz B, Zhang Y and Kim P 2007 *Phys. Rev. Lett.* **98** 206805.

[20] Li X, Wang X, Zhang L, Lee S and Dai H 2008 *Science* **319** 1229–32.

[21] Tworzydło J, Trauzettel B, Titov M, Rycerz A and Beenakker C W J 2006 *Phys. Rev. Lett.* **96** 246802.

[22] Miao F, Wijeratne S,Zhang Y, Coskun U C, Bao W and Lau C N 2007 *Science* **317** 1530-33.

[23] Danneau R, Wu F, Craciun M F, Russo S, Tomi M Y, Salmilehto J, Morpurgo A F and Hakonen P J 2006 *Phys. Rev. Lett.* **96** 246802.

[24] Danneau R, Wu F, Craciun M F, Russo S, Tomi M Y, Salmilehto J, Morpurgo A F and Hakonen P J 2008 *J. Low Temp. Phys*. **153** 374-392.

[25] Martin J, Akerman N, Ulbricht G, Lohmann T, Smet J H, von Klitzing K and Yacoby A 2008 *Nature Physics* **4** 144-148.

[26] Perez N M R 2010 *Rev. Mod. Phys*. **28** 2673-2700.

[27] Jiang Z, Zang Y, Stormer H L and Kim P 2007 *Phys. Rev. Lett* **99** 106802.

[28] Öezyilmaz B, Jarillo-Herreo P, Efetov D, Abanin D A, Levitov L S and Kim P 2007 *Phys. Rev. Lett.* **99** 166804.

[29] Büttiker M, Imry Y, Landauer R and Pinhas S 1985 *Phys. Rev. B* **31** 6207-6215.

[30] Chen J H, Jang C, Adam S, Fuhrer M S, Williams E D and Ishigami M 2008 *Nature Physics* **4** 377-381.

[31] Peres N M R, Lopes dos Santos J M B and Stauber T 2007 *Phys. Rev. B* **76** 073412.

[32] Adam S, Hwang E H, Galitski V M and Das Sarma S 2007 *Proc. Nat. Aca. Sci.* **104** 18392-18397.

[33] Shon N H and Ando T 1998 *J. Phys. Soc. Jap*. **67** 2421-2429.

[34] Stauber T, Peres N M R and Guinea F 2007 *Phys. Rev. B* **76** 205423.

[35] Hwang E H and Das Sarma S 2008 *Phys. Rev. B* **77** 115449.

[36] Shishir R S and Ferry D K 2009 *J. of Phys.: Condensed Matter* **21** 232204.

[37] Nair R R, Blake P, Grigorenko A N, Novoselov K S, Booth T J, Stauber T, Peres N M R and Geim A K 2008 *Science* **320** 1308.

[38] Falkovsky L A 2008 *Journal of Physics: Conference Series* **129** 012004.

[39] Xia F N, Mueller T, Lin Y-M, Valdes-Garcia A and Avouris P 2009 *Nat. Nanotechnol.* **4** 839–843.

[40] Müller T, Xia F and Avouris P 2010 *Nature Photon.* **4** 297-301.

[41] Wang X, Zhi L and Muellen K 2008 *Nano Lett.* **8** 323–327.

[42] Casiraghi C, Pisana S, Novoselov K S, Geim A K and Ferrari A C 2007 *Appl. Phys. Lett.* **91** 233108.

[43] Mintmire J W, Dunlap B I and White C T 1992 *Phys. Rev. Lett.* **68** 631–634.

[44] Iijima S 1991 *Nature* **354** 56–58.

[45] Iijima S and Ichihashi T 1993 *Nature* **363** 603–605.

[46] Bethune D S, Kiang C H, Devries M S, Gorman G, Savoy R, Vaszquez J and Beyers R 1993 *Nature* **363** 605–607.

[47] Dresselhaus M S, Dresselhaus G and Avouris P *Carbon Nanotubes: Synthesis, Structure Properties and Applications* 2001 Springer-Verlag, Berlin, Germany.

[48] Ouyang M, Huang J L, Cheung C L and Lieber C M 2001 *Science* **292** 702–705.

[49] Mintmire J W, Dunlap B I and White C T 1992 *Phys. Rev. Lett.* **68** 631–634.

[50] Avouris P, Appenzeller J, Martel R and Wind S J 2003 *Proc. IEEE* **91** 1772–84.

[51] Imry Y and Landauer R 1999 *Rev. Mod. Phys.* **71** S306–S312.

[52] Data S *Electronic Transport in Mesoscopic Systems* 1995 Cambridge Univ. Press, Cambridge, U.K.

[53] McEuen P L , Bockrath M, Cobden D H, Yoon Y-G and Louie S G 1999 *Phys. Rev. Lett.* **83** 5098–5101.

[54] Wenjie L, Bockrath M, Bozovic D, Hafner J H, Tinkman M and Hongkum P 2001 *Nature* **411** 665–669.

[55] Kong J, Yenilmez E, Tombler T W, Kim W, Dai H, Laughlin R B, Liu L, Jayanthi C S and Wu S Y 2001 *Phys. Rev. Lett.* **87** 106 801/1–106 891/4.

[56] Appenzeller J, Martel R, Avouris P, Stahl H and Lengeler B 2001 *Appl. Phys. Lett.* **78** 3313–3315.

[57] Collins P G, Arnold M S and Avouris P 2001 *Science* **292** 706–709.

[58] Collins P G and Avouris P 2002 *Appl. Phys. A* **74** 329–332.

[59] Bachtold A, Strunk C, Salvetat J-P, Bonard J-M, Forró L, Nussbaumer T and Schönenberger C 1999 *Nature* **397** 673–675.

[60] Schoenenberger C, Bachtold A, Strunk C, Salvetat J-P and Forro L 1999 *Appl. Phys. A* **69** 283–295.

[61] Murphy E L and Good R H 1956 *Phys. Rev.* **102** 1464–73.

[62] Xu N S and Huq S E 2005 *Mater. Sci. Eng. R – Rep.* **48** 47–189.

[63] Yamamoto S 2006 Rep. Prog. Phys. **69** 181–232.

[64] Gomerv R *Field Emission and Field Ionization* 1961 Harvard University Press, Cambridge, MA.

[65] Di Bartolomeo A, Scarfato A, Giubileo F, Bobba F, Biasiucci M, Cucolo AM, Santucci S and Passacantando M 2007 *Carbon* **45** 2957–2971.

[66] Fowler RH and Nordheim L 1928 *Proc. Royal Soc. A* **119** 173-181.

[67] Edgcombe C J 2005 *Phys Rev B* **72** 045420 1–7.

[68] Edgcombe C J and Johansen A M 2003 *J. Vac. Sci. Technol. B* **21** 1519–23.

Chapter 2

Graphene-based field-effect transistors

2.1 Introduction

The Si-based electronics has severe physical limitations for further developments, in particular related to high power dissipation caused by leakage effects. This is especially dangerous when continuing the shrinkage of field effect transistor (FET) dimensions and oxide thicknesses [1,2].

Graphene is a promising candidate for future nanoelectronics. Graphene-based field-effect transistors (GFETs) [3] combine an ultra-thin body suitable for aggressive channel length scaling [4], with excellent properties, as a linear dispersion relation with electrons behaving as massless Dirac fermions [5], a very high carrier mobility [6] and a superior current density capability [7]. In such devices, an electric current is injected/extracted from metallic electrodes (source/drain) through a graphene channel whose conductance is modulated by the electric field from a back- or top-gate. The linear energy dispersion, with zero bandgap and a double-cone shape with intrinsic Fermi level at the vertex, gives symmetric valence and conduction bands; differently from most materials, current modulation by means of a gate in GFETs is possible even without a bandgap, due to the vanishing density of states at the vertex [5, 8].

However the development of graphene-based electronics is limited by the quality of the contacts between the graphene and the metal electrodes [9-11] which can significantly affect the electronic transport properties of the devices [12]. Despite this, the physics of graphene–metal contacts remains still an open subject.

Although the carrier mobility in the graphene is high, the very small DOS for graphene might suppress the current injection from the metal contacts to the graphene, thus resulting in high contact resistivity R_c [10,12]. In particular, a high R_c limits the total on-state current, and has a severe impact on transistor performance, negatively influencing the peak transconductance as well as the linearity of the current versus gate-voltage characteristic [13].

The use of a four-point setup for electrical characterization is clearly suitable to prevent the problems related to contact resistance, but real electronic applications are based on two-

terminal devices where the effect of contact resistance cannot be avoided. For such reason it becomes of fundamental importance to characterize the metal/graphene interfaces at the contacts. Moreover, current crowding occurs as the current transfers between the graphene and the metal contact over a finite length, leading to a non-uniform current density that is higher at the edge of the metal contact and decreases to zero deeper into the contact [10,14]. Up to now, a large range of R_c values is reported in literature, either as edge specific contact resistivity (R_cW in $\Omega\mu m$, with W the width of the contact), or area specific contact resistivity ρ_c ($\rho_c = R_cA$ in $\Omega\mu m^2$, with A the area of the contact). Experimentally, the use of Pd contacts on graphene has resulted in the lowest edge specific contact resistivity (230 ± 20 $\Omega\mu m$ [15]), while for Ti contacts a value of 0.8 $k\Omega\mu m$ [16], and for Ni contacts an area specific contact resistivity of few $k\Omega\mu m^2$ have been reported. Annealing treatments of the contacts in different gases (H_2-Ar [10], O_2 [17]) have been proposed in order to improve the specific contact resistivity.

In section 2.2 we report the electrical characterization of graphene-based field-effect transistors and the physical effects due to the contact resistance on the graphene layers. The transistor transfer characteristics (source-drain conductance versus back-gate voltage) showed a clear double-dip feature that is discussed in terms of graphene doping under metal contacts [18-19] and a hysteresis that is attributed to charge trapping in silanol group at the SiO_2 surface [20, 21]. In order to analyze the effects of the metal contacts on the graphene, several parallel contacts (with Ti or Ni) were produced for each device to perform transfer length method (TLM) measurements, which evidenced a dependence of the contact resistance on the back-gate voltage for both metals [22].

Since the superconductor/graphene junction is the ideal platform to study the interaction of Cooper pairs and massless Dirac fermions, this is a research field that let envisage new fundamental physics as well as innovative device applications. The absence of a bandgap in graphene enables easy formation of ohmic contacts with most superconducting metals. Nonetheless, the band alignment and the vanishing density of states (DOS) of graphene around the Dirac point, as well as defects or chemical residues, may affect current injection and hinder the detection of exotic new phenomena at the superconducting transition. The understanding of the contact formed by a given superconductor with graphene is therefore an important prerequisite to any low temperature investigation.

Heersche et al. [23] used back-gated graphene field effect transistors with Ti/Al contacts to demonstrate that graphene can support a supercurrent, which is carried either by electrons in the conduction band or by holes in the valence band, and that Josephson effect in graphene is

a robust phenomenon. Rickhaus et al. [24] fabricated superconductor-graphene-superconductor (S-G-S) devices based on Niobium (Nb) contacts to study the integer quantum Hall effect and evidenced Andreev processes at the graphene-superconductor interface. Their devices were fabricated with exfoliated graphene on SiO_2/p-Si substrate and, when tested as back-gated field effect transistors, exhibited asymmetric transfer characteristics with saturation in the p-branch and a field effect mobility around 3000 $cm^2V^{-1}s^{-1}$. Since they observed an exponentially increasing contact resistance for decreasing temperature, to achieve transparent contacts to graphene they used a 4 *nm* Ti layer under Nb. Similarly, Komatsu et al. [25] fabricated S-G-S junctions with Nb to investigate the superconducting proximity effect through graphene. They found that the low transparency of the superconductor/graphene junction is a serious limitation and, only after using an intermediate thin Pd layer (4- to 8 *nm* thick), they were able to evidence a suppression of the critical current near the graphene charge neutrality point, which was attributed to specular reflection of Andreev pairs at the interface of charge puddles. Mizuno et al. [26] fabricated high-quality suspended monolayer graphene–Niobium nitride (NbN) Josephson junctions and measured a supercurrent at critical temperatures greater than 2 *K*. The production of highly transparent graphene–NbN contacts was identified as one of the major experimental challenges. A Ti/Pd intermediate layer was e-beam evaporated on graphene prior to Ar/N_2 plasma sputtering of Nb to reduce the damage from energetic ions and improve contact transparency.

To date, Nb is the metal often chosen in the superconductor/graphene investigations for its high critical temperature (9.25 *K*) and well-known properties and deposition technology, although it does not seem to establish a good contact with graphene and a thin inter-layer is often added. If and how this extra layer impacts the physics at the superconducting transition is unclear. In this direction, a deeper understanding of the properties of the Nb/graphene interface and the assessment of its suitability for superconductor/graphene investigations is timely and necessary.

In section 2.3 we report the electrical characterization of graphene field effect transistors at room temperature and decreasing pressure with the goal to elucidate specific features of the Nb/graphene contact. We find that gently sputtered Nb forms contacts with specific resistivity (~ 25 $k\Omega\mu m$) in the range of that reported for evaporated metals, as Ti or Cr (~ 1-100 $k\Omega\mu m$), and about an order of magnitude higher than the specific contact resistance achieved with strongly chemisorbed metals as Pd or Ni (~ 0.1-5 $k\Omega\mu m$) [10,19, 27-29]. We distinguish the role of air adsorbates and process residues on the doping of the graphene channel from that of the supporting SiO_2 and argue that strain of graphene under the contacts plays an important

role in increasing the contact resistance. Furthermore we show that Niobium acts as p-dopant on graphene and that depinning of the graphene Fermi level at the contact strongly suppresses the conductance of the transistor in the electron branch. As a byproduct, we estimate a lower limit for the workfunction of the Nb film as $\Phi_{Nb} \geq 4.7\ eV$ [30].

From an experimental viewpoint, the use of scanning electron microscopy (SEM), transmission electron microscopy (TEM), electron beam lithography (EBL) and focus ion beam (FIB) processing in ultra-high vacuum represents a necessary step for the fabrication and characterization of graphene-based devices. Consequently, graphene devices during fabrication or under test are necessarily exposed to high vacuum and electron irradiation, which may considerably affect their electronic properties.

Several experiments have shown that the irradiation of energetic particles, such as electrons [31-35] and ions [36,37], can induce defects and damages in graphene and cause severe modifications of its properties. Raman spectroscopy has been largely used to study electron-beam induced structural modifications [38-40] or formation of nanocrystalline and amorphous carbon [37,41]. The shape and relative magnitude of a D peak, as well as the shift of the G peak, have been used to quantitatively evaluate the damage and the strain induced by a very low energy e-beam [42]. Raman and Auger electron spectroscopy have shown that e-beam irradiation can selectively remove graphene layers and induce chemical reactions and structural transformations [39,40]. The interaction of an e-beam with water adsorbates on the graphene surface has been also proposed for the hydrogenation of graphene [43,44]. However, the Raman spectroscopy is unable to reveal all the effects of e-beam irradiation, and electrical measurements are needed to check for possible modifications of transport properties. Despite that, electronic transport properties of irradiated graphene devices have not yet been deeply investigated [45,46]. The negative shift of the Dirac point has been reported as an effect of e-beam induced n-doping. The comparison with the case of suspended graphene has also evidenced the importance of the substrate [45]. It has been demonstrated in particular that e-beam irradiation of graphene field effect transistors modifies the substrate band bending and results in localized n-doping of graphene, which creates graphene p-n junctions working as photovoltaic device [47].

In section 2.3, after the electrical characterization of graphene field effect transistors with Nb contacts at room temperature and decreasing pressure, we study the modification of electronic transport properties of GFETs upon exposure to electron beam irradiation for scanning electron microscopy imaging with acceleration energy up to 10 *keV*. Electron irradiation affects the transistor current drive capability by reducing the carrier mobility and

increasing the channel and contact resistance. We also show that, for low energy electron irradiation, the conditions of pristine devices are almost restored by successive gate voltage sweeps while measuring the channel conductance [48].

Since the discovery of graphene, the field effect modulation of the relativistic charge carriers in this material has largely been investigated in capacitive structures, whereby a highly doped substrate coated by an oxide dielectric was used as back-gate to apply a vertical electric field. Extra control was then added by including a top-gate, at the cost of process complexity and increased risk of device failure due to the top dielectric deposition [49-52]. The use of side-gate(s) to limit interaction with dielectrics and avoid mobility degradation emerged soon after with side-gates formed by graphene [53-57] or metal leads [58]. All-graphene devices, where graphene is used both as channel and side-gate, offer the further advantage of the fabrication of self-aligned structures in a single lithographic step, with optimized gate to source/drain overlapping.

To date, research on side-gate devices has been dealing with the effect of the gate on the electrical transport properties of the graphene channel in terms of the modulation of conductance [53-54,58], penetration of the transversal field in the channel [53] or transconductance [55]. Different geometries with single and dual side-gate and various critical dimensions have been considered [56], and some progress has been made towards a process suitable for integration in the existing Si technology [57].

The potentially high gate leakage caused by current flowing from gate to channel through the dielectric/air or dielectric/vacuum interface is one of the main weaknesses of graphene side-gated transistors [54]. Besides, the electron transport between horizontal graphene flakes at a nanometric distance and on a dielectric surface is by itself an interesting fundamental problem. Yet, it has received almost no attention. Although electron emission from the edge of a graphene flake has been largely investigated in connection to the quest for graphene field emission devices [59-65], the current between two graphene flakes separated by a nanogap has been rarely investigated. Wang et al. [66] patterned graphene sheets with crystallographically matching edges by divulsion, separated by a few hundred-nanometers distance on SiO_2/Si and used them to measure the current-voltage (*I-V*) characteristics in a high-vacuum chamber. They found that *I-V* curves are governed by the space-charge-limited flow of current at low biases and by Fowler–Nordheim [67] tunneling in high voltage regime. A recent study on field emission between suspended graphene flakes also reported Fowler-Nordheim field emission as a dominant microscopic mechanism and a current density as high as 10 *nA/µm* at modest voltages of tens of volts [68]. In particular, it was found that the

emission is stable in time and repeatable over large numbers of voltage cycles, and that the emission current follows a power law dependence on pressure, a feature that they suggest to exploit for sensing purposes.

In section 2.4, we study the side-gating effect and the gate leakage in all-graphene devices. Side-gated all-graphene field-effect transistors have been fabricated by patterning exfoliated flakes on a SiO_2/Si substrate. Channel and gate are formed by graphene with parallel edges, separated by 100 *nm* gap. Such configuration helps to build a uniform electrical field along the channel direction, which is suitable to study the planar gate-to-channel leakage mechanisms and the electron field emission from individual graphene flakes. We report rapidly growing leakage for an electric field higher than 150 *V/μm* and we clarify that the current is due to Frenkel-Poole transport through SiO_2 until Fowler-Nordheim emission in vacuum between graphene flakes takes over and dominates with a current reaching a value as high as 1 *μA/μm* at ~ 1 *kV/μm*. This study offers opportunities for both fundamental and applied research in vacuum nanoelectronics [69].

2.2 GFETs with Nickel and Titanium contacts

2.2.1 Devices fabrication and measurement setup

Graphene flakes, produced by mechanical exfoliation (scotch-tape method) from graphite, were transferred to Si substrates covered by a 300 *nm* thermal SiO_2. The first identification of the graphene flakes was performed by optical microscopy and then confirmed by Raman spectroscopy and SEM imaging [70]. Larger flakes (between 20 *μm* and 50 *μm* in at least one dimension) were selected in order to produce multi-lead devices. Normally, four to six parallel leads were realized by electron beam lithography and a lift-off process. The scheme of the produced GFETs is shown in Fig. 2.1(a). Images of real devices acquired by a scanning electron microscope are also reported in Fig. 2.1: two devices with Ni contacts (Fig. 2.1(b) and Fig. 2.1(c)) in the following named as sample Ni#1 and sample Ni#2, and two devices with Ti contacts (sample Ti#1 in Fig. 2.1(d) and sample Ti#2 in Fig. 2.1(e)). The graphene flakes have been produced and transferred to Si substrates at IHP-Microelectronics in Frankfurt instead the metal electrodes have been grown at Georgetown University of Washington (DC).

In order to improve the quality of the interface between the graphene and the metal lead, the flakes are normally kept under a vacuum better than 10^{-5} *mbar* before depositing Ti (work function ≈ 4.33 *eV*) or Ni (work function ≈ 5.01 *eV*) contacts by sputtering.

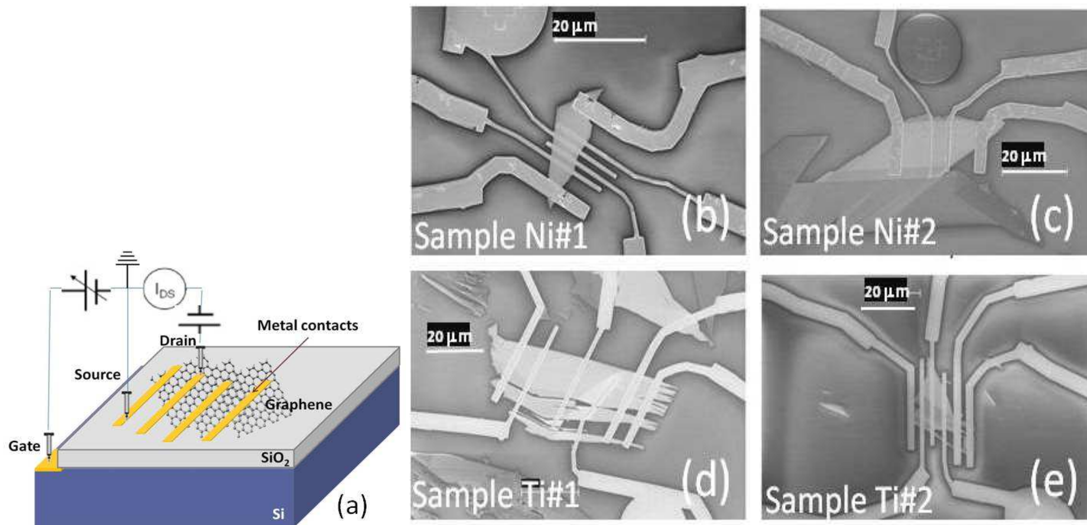

FIGURE 2.1: (a) Schematic representation of a GFET device. (b)-(e) SEM images of typical devices produced for this experiment; (b) graphene monolayer contacted with Ni leads; (c) mono- and bi-layer contacted with Ni leads; (d) bi-layer with Ti contacts (the bi-layer is further exfoliated to become a mono-layer under one lead); (e) mono- and bi-layer contacted with Ti leads.

It was chosen a geometric configuration suitable for transfer length method (TLM) measurements with 200 *nm*-to-2 *μm* large leads with a separation of up to 15 *μm* from each other. The Ni and Ti leads were 70 *nm* thick and were coated with a 50-70 *nm* Au layer to prevent oxidation and to favor good electrical connection to the probes. We observe that any couple of leads on the device is suitable to realize a FET configuration, the Si substrate being the back-gate, the two leads being source and drain, and the geometrical parameters of the transistor being the channel length (i.e. the separation between the two leads) and the width (i.e. the width of the flake delimited by the two leads).

Electrical measurements were performed at room temperature under ambient conditions with a Keithley 4200 Semiconductor Parameter Analyzer interconnected to a probe station allowing micrometric movements of four metallic probes used to directly connect devices without any bonding process. The systematic measurement routine for each device consisted in recording transfer characteristics (drain current I_{DS} vs. gate voltage V_{GS}) and output characteristics (drain current I_{DS} vs. drain bias V_{DS}) for any transistor resulting from the permutation of any possible couple of leads deposited on the flake and the Si substrate fixed as back-gate on which it was possible to apply a bias sweep in the range ±80*V*.

2.2.2 Results and discussion

2.2.2.1 Transfer characteristics

Transfer characteristics of GFETs typically display a symmetric V-shape, with a hole dominated conductance (p-branch) at lower V_{GS} and electron-type transport at more positive gate voltages (n-branch), separated by a valley corresponding to the charge neutrality condition (the Dirac point) with equal electron and hole concentrations. This V-shape reflects the energy distribution of the density of states ($D(E) \propto |E|$), and a conductance dropping to zero at the Dirac point should be expected at low temperature; however, in actual devices, impurities and interaction with the surrounding dielectric introduce local fluctuations in the potential causing a finite density of states at the Dirac point; from the carrier viewpoint, these fluctuations result in localized puddles of electrons and holes which produce an appreciable conductance [71].

An example of measured transfer characteristics for a couple of leads for any device is reported in Fig. 2.2. The GFETs exhibit, in all cases, non-conventional transfer characteristics, with distortion in the positively gated region. In particular, a clear double-dip feature is measured for devices Ni#1 (Fig. 2.2(a)) and Ni#2 (Fig. 2.2(b)). For the devices of Fig. 2.2(c) and Fig. 2.2(d) (Ti#1 and Ti#2 respectively) the feature is probably appearing at voltage bias larger than our sweep range.

The asymmetry between p- and n-branches was explained in terms of the metal/graphene interaction at the contacts [19, 72–74]. It has been found in particular that, even in the case of weak adhesion, as with Au, the metal electrodes cause the Fermi level E_F to shift from the conical point in graphene bands, resulting in doping of graphene either with electrons or with holes. The amount of doping can be deduced from the difference of the metal and graphene work functions ($\Phi_M - \Phi_{G0}$) and from the potential step (ΔV) due to the metal/graphene chemical interaction ($E_F = \Phi_M - \Phi_{G0} - e\Delta V$). Depending on the polarity of carriers in the bulk of the graphene channel, charge transfer between metal and graphene leads to p–p, n–n or p–n junctions in the vicinity of the contacts which can cause asymmetry.

The double dip feature has been already reported [18] for GFETs contacted with Cr/Au where a wide hysteresis between the forward and reverse sweep and a higher inter-electrode distance created a clearer double-dip.

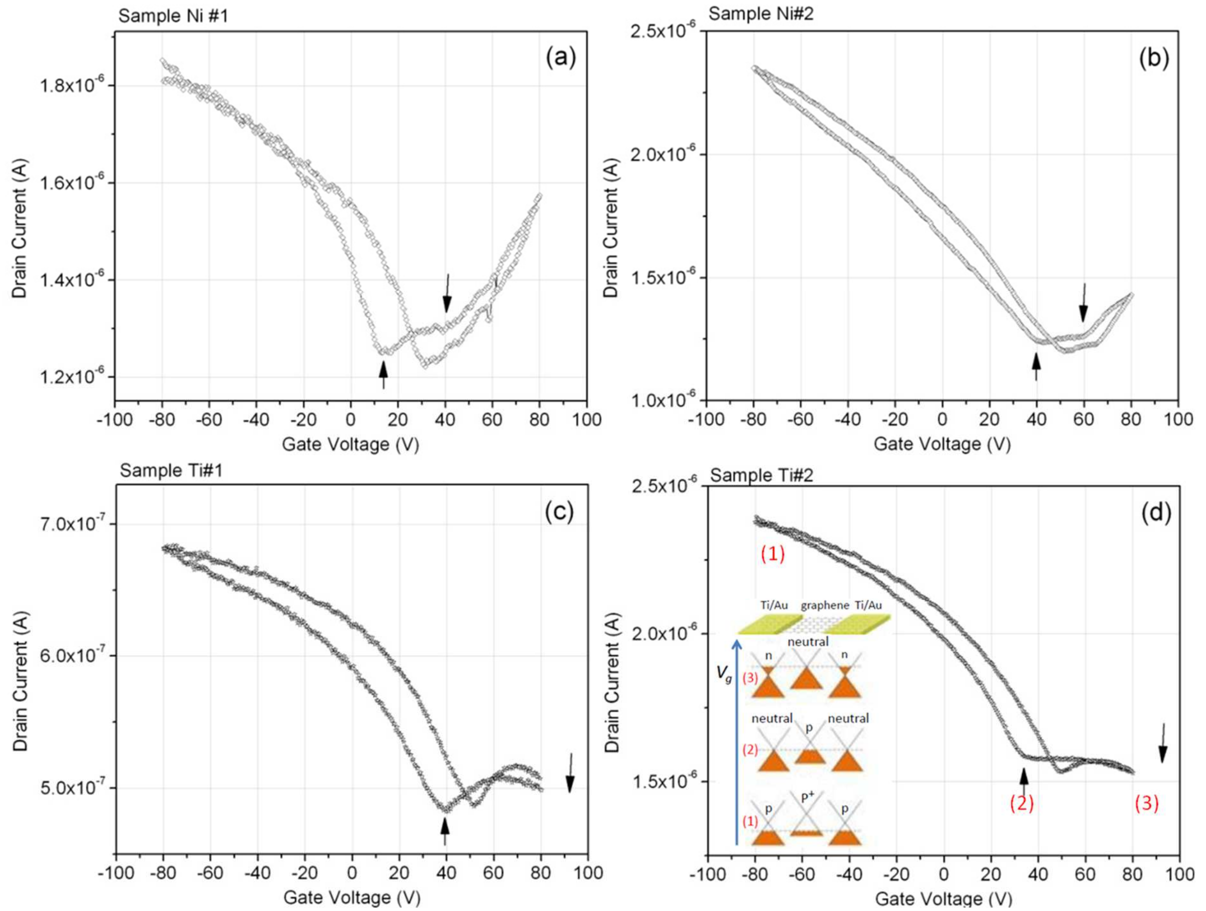

FIGURE 2.2: Transfer characteristics (I_{DS} vs V_{GS}) for the devices shown in Fig. 2.1(b)-(e). (a) Sample Ni#1 and (b) sample Ni#2 show a clear double-dip feature (indicated by arrows); (c) Sample Ti#1 and (d) sample Ti#2 show a first dip in the conductance curve and a slop that indicates the presence of a second dip at larger bias with respect our sweep range. The inset of figure (d) shows a model to explain the double dip feature.

The experimental observation can be interpreted as the effect of charge transfer and doping of the graphene layer under the contacts [19], which in long devices yield two conductance minima at the energies of the Dirac points of graphene in the clamped and channel regions. Indeed, electrons transfer from the graphene to the metal electrodes due to their different work functions, thus forming a gradient in the doping profile from the contacts to the bulk channel, and p-n junctions are spontaneously formed. The doping extends for 0.2–0.3 μm in the inner channel, making its effect barely detectable in shorter channel transistors. It has been proved [18] that metal doping and charge trapping at SiO_2/graphene interface, as well as partial pinning of the Fermi level at contacts, can fully explain the behavior of a whole I_{DS} - V_{GS} loop and in particular, account for the double dip feature.

We qualitatively summarize the key points of this model with the help of the inset of Fig. 2.2(d) that shows a simplified band diagram from source to drain for a device with Ti

leads, while forward sweeping the V_{GS} voltage. The electron transfer from Ti to graphene, due to the work function mismatch (4.33 *eV* for Ti and 4.5 *eV* for graphene), makes graphene less p-doped underneath the contacts than in the channel. The application of the back-gate voltage moves the Fermi level in the graphene band diagrams, determining different conduction regions between source and drain. At V_{GS}=-80V (point 1 in Fig. 2.2(d)), p-type conduction takes place everywhere, thus giving a high conductance p/p$^+$/p structure (source/channel/drain graphene doping). While rising V_{GS} to positive values, electrons are attracted to the channel and a charge neutrality condition is reached at the contacts, where the graphene is less p-doped; a low conductance neutral/p/neutral structure is achieved, which corresponds to the first valley in the I_{DS} - V_{GS} curve (point 2). A further increase in V_{GS} gradually reduces the p-doping in the channel and increases the n-doping at contacts, until a charge neutrality condition is reached in the channel and a low conductance n/neutral/n structure is achieved, which corresponds to the second valley in the I_{DS} - V_{GS} curve that we presume might appear at voltage bias larger than our sweep range (point 3).

With Ni leads a similar behavior is obtained with the difference that the graphene under the contacts is now more p-doped than that in the channel and a neutrality condition is first reached in the channel during the forward V_{GS}, making the first minimum deeper than the second one.

The hysteretic behavior between the forward and reverse sweeps in the transfer characteristics of Si/SiO_2 supported GFETs has been attributed mainly to charge trapping in silanol groups (Si–OH) with surface-bound H_2O molecules facilitating the process of charge transfer and trapping [75, 76]. Consequently the concentration, distribution and reactivity of the silanol groups of the underlying SiO_2 play a decisive role in the transfer characteristics of a GFET. Thermal annealing or vacuum pumping can also help to reduce hysteresis [74]. The hysteresis, enhanced by a double dip, can conveniently be exploited to built graphene-based memory devices [18].

2.2.2.2 Contact resistance

In order to characterize the contacts produced on each device, we measured the output characteristic (I_{DS} vs V_{DS}) for each couple of leads. In Fig. 2.3 we show as example a measurement for a selected couple of leads for any device introduced above. The drain voltage has been swept up to a maximum value of 20 *mV* while measuring the drain current, this for nine different values of the gate voltages between -80*V* and +80*V* with step of 20*V*. The output characteristics showed a linear behaviour for both Ni and Ti contacts, evidencing

that sufficiently good contact is established between the graphene and the metals.

When measuring a resistance with two probes, it is necessary to take into account the serial contribution of the channel resistance R_{ch} and the contacts R_{c1}, R_{c2}. For a sample with irregular shape, we consider geometrical parameters due to different lengths of the leads on the graphene (d_1 and d_2), different widths (W_1 and W_2) and the channel length L (a scheme is drawn in Fig. 2.4(a)).

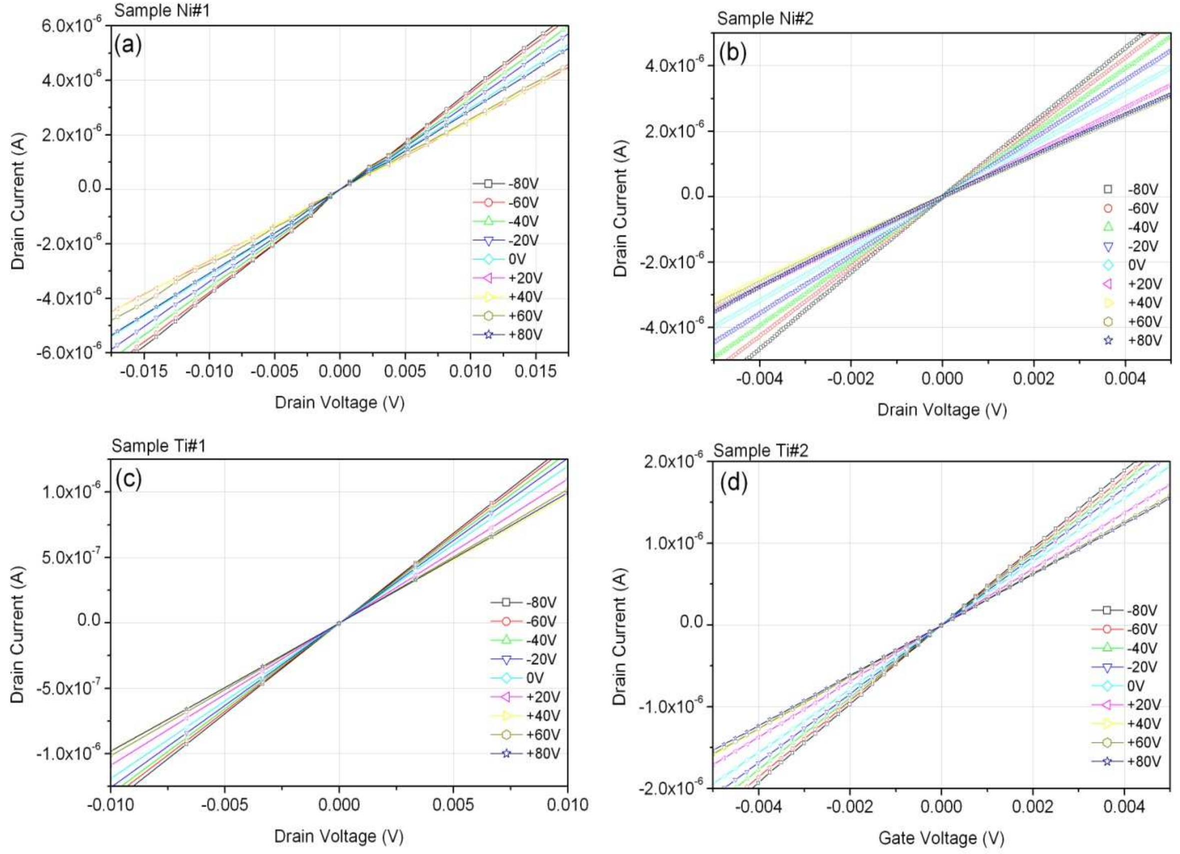

FIGURE 2.3: Output characteristics I_{DS} vs. V_{DS} measured for different gate voltages for each device of Fig. 2.1.

Comparing the contact length d_i with the transfer length $d_T = \sqrt{\rho_c / R_{sh}}$, i.e. the effective length contributing to the current flow [10], which is typically longer than 1 μm (R_{sh} is the sheet resistance of the graphene channel in $\Omega/\square$ and $\rho_c = R_c W d$ is the area specific contact resistivity), it results for our devices that $d_i < d_T$ and consequently we can characterize the contact resistance by evaluating ρ_c instead of the edge specific contact resistivity [10,75].

A generic graphene channel delimited by two parallel leads can be easily approximated as a trapezoid, and the total resistance for a two-probe measurement can be written as the sum of the channel resistance R_{ch} and the contacts R_{c1} , R_{c1}:

$$R = R_{c1} + R_{c2} + R_{ch}. \tag{2.1}$$

From the expression of the area specific contact resistivity we can write:

$$R = \frac{\rho_c}{W_1 d_1} + \frac{\rho_c}{W_2 d_2} + R_{sh}\int_0^L \frac{dx}{W_1 + \frac{(W_2 - W_1)x}{L}} =$$
$$= \frac{\rho_c}{W_1 d_1} + \frac{\rho_c}{W_2 d_2} + R_{sh}\frac{ln(W_2/W_1)}{W_2 - W_1}L, \tag{2.2}$$

where we assumed that ρ_c has the same value for the two leads when the same metal is used. By defining:

$$R_{eff} = R\left(\frac{1}{W_1 d_1} + \frac{1}{W_2 d_2}\right)^{-1}, \tag{2.3}$$

we can obtain an equation in which the specific contact resistivity ρ_c can be evaluated as the intercept of a plot of R_{eff} versus L for every couple of electrodes (TLM method):

$$R_{eff} = \rho_c + R_{sh}\left(\frac{1}{W_1 d_1} + \frac{1}{W_2 d_2}\right)^{-1}\frac{ln(W_2/W_1)}{W_2 - W_1}L. \tag{2.4}$$

R_{eff} has been obtained from the output characteristics measured at given back-gate voltages V_{GS} for all two-lead combinations on a flake. In Fig. 2.4(a) and Fig. 2.4(b) we report the values of R_{eff} for two of our samples, Ni#1 (V_{GS} = -80V) and Ti#1 (V_{GS} = +80V), respectively. The reduced number of experimental points for the Ni#1 sample is responsible for the relatively higher error in the estimation of the intercept value, being about 5% for Ni#1 (7.0 ± 0.3 $k\Omega\mu m^2$).

By applying the TLM method, we can extract the ρ_c vs. V_{GS} and we can compare it with the R_{eff} (V_{GS}) for a couple of leads for sample Ni#1 (Fig. 2.4(c)) and Ti#1 (Fig. 2.4(d)). The data are a clear experimental evidence that the specific contact resistivity is modulated by the back-gate voltage. Furthermore, they show that the specific contact resistivity dependence on the back-gate voltage has the same qualitative behaviour as the total source-to-drain resistance, with a peak around the Dirac point (≈ 20 - 40V) and a decrease when the channel is field-doped by the back gate. A similar result has been reported for Pd-contacted GFETs [15] and confirms the gate modulation of the Fermi level relative to the energy at the Dirac point for the graphene underneath the metal [76].

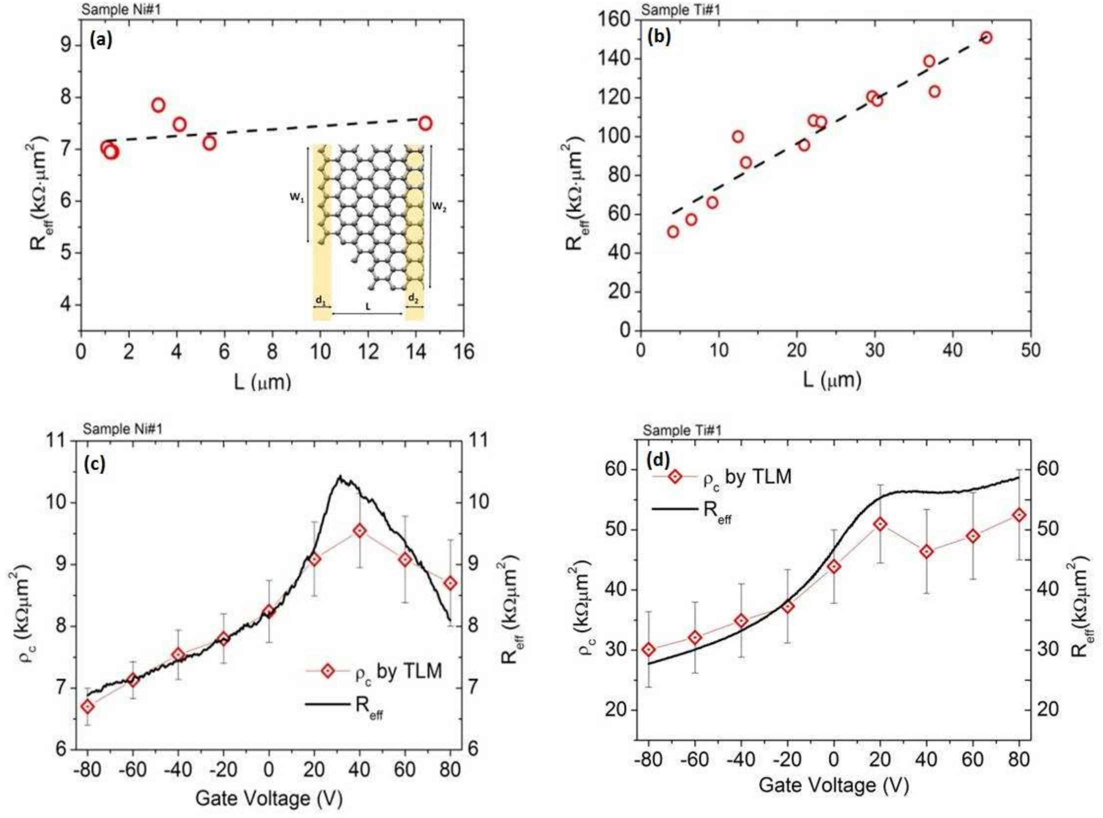

FIGURE 2.4: (a) - (b) TLM plot of R_{eff} (L) at a given V_{GS} for sample Ni#1 (V_{GS} = - 80V) and Ti#1 (V_{GS} = + 80V) respectively. The dashed lines represent linear fit of experimental data. The inset of plot (a) shows a scheme of a graphene device with varying channel width and with contacts of different lengths. (c) - (d) Contact resistivity ρ_c and effective resistance R_{eff} as a function of the back-gate voltage V_{GS} for sample Ni#1 and Ti#1 respectively.

From the comparison of $\rho_c(V_{GS})$ and $R_{eff}(V_{GS})$ it is evident that the resistance of the TLM device is principally due to the contact resistance. The relatively high values measured for ρ_c (~ 7 $k\Omega\mu m^2$ for Ni-contacted devices and ~30 $k\Omega\mu m^2$ for Ti-contacted devices) could be a result of our fabrication procedure, in which we did not perform any treatment before metal sputtering or any annealing post fabrication. We also realized the metal electrodes by sputtering, a process that usually results in higher contact resistance with respect to evaporation technique [17]. Moreover, we cannot exclude the possibility that some oxidation took place at the contacts due to oxygen diffusion and that we have somehow overestimated the effective contact area.

On sample Ti#1 (Fig. 2.1(d)) we have one electrode (the fourth contact from the left side) deposited on a monolayer graphene area. Consequently, we also had the opportunity to consider the case with both leads on bi-layer graphene (third and fifth contact, for example) and make a comparison with the case in which one lead is on a monolayer (third and fourth contacts). We experimentally measured R_{eff} at V_{GS} = - 80 V in both cases and we found that

there are no significant differences, the R_{eff} value being about 44 $k\Omega\mu m^2$ for both electrodes on bi-layer and about 42 $k\Omega\mu m^2$ for one electrode on monolayer, thus confirming that the contact resistance does not depend on the number of graphene layers [77].

2.3 GFETs with Niobium contacts

2.3.1 Devices fabrication and measurement setup

Graphene flakes were obtained from highly oriented pyrolytic graphite by scotch tape method and transferred onto SiO_2/Si substrates. We used moderately doped p-Si (resistivity 1-10 Ωcm) covered by 300 *nm* of thermally grown SiO_2 to maximize the color contrast for optical identification of few-layer graphene [78]. A short dip (~ 60 *s*) in warm acetone was used to remove glue residuals. Graphene flakes have been produced and transferred to Si substrates at IHP-Microelectronics in Frankfurt.

Monolayers and few layers graphene were identified optically and further confirmed by Raman spectroscopy and SEM imaging [79]. Selected graphene monolayer were contacted using electron beam lithography on poly(methyl methacrylate) (PMMA) to define suitable metal patterns, followed by a standard lift-off technique. The graphene flakes were contacted by Nb/Au metallic bilayer (25 *nm* Nb/75 *nm* Au) with niobium contacting the graphene and gold working as a cap layer to prevent Nb oxidation and favor electrical connection with the probe tips. The metal electrodes were fabricated by a three cathode RF magnetron sputtering system for in-situ multilayer deposition. To effectively remove physisorbed molecules and processing residues as PMMA, the sample was subjected to several hours vacuum degassing at ~ $3\cdot10^{-7}$*mbar* before metal deposition. Metallic leads were sputtered at low power density (< 0.7 Wcm^{-2}) and small deposition rates (0.3 *nm/s* for Nb and 1.2 *nm/s* for Au) to prevent graphene damages. The sputtering was made in 99.999% pure Argon at pressure of $4\cdot10^{-3}$*mbar* with substrate at room temperature. The target purity was 99.98% for Nb and 99.95% for Au. To ensure good purity of sputtered Nb, prior to the deposition, a quite energetic cathode pre-sputtering of 5 *min* at 3.5 Wcm^{-2} was performed. The metal electrodes Nb/Au have been grown at the University of Salerno.

Fig. 2.5(a) shows a 20× magnification of few ribbon-shaped graphene monolayers that were contacted in a 2-point configuration. The SEM images of Fig. 2.5(b) and Fig. 2.5(c) show details of the pads and metal leads of the final device. The study presented here is

referred to the graphene flake between the leads labeled 1 and 6 in Fig. 2.5(c). The flake is 19.91 μm long and 0.79 μm large. Similar results were found with the other graphene ribbons.

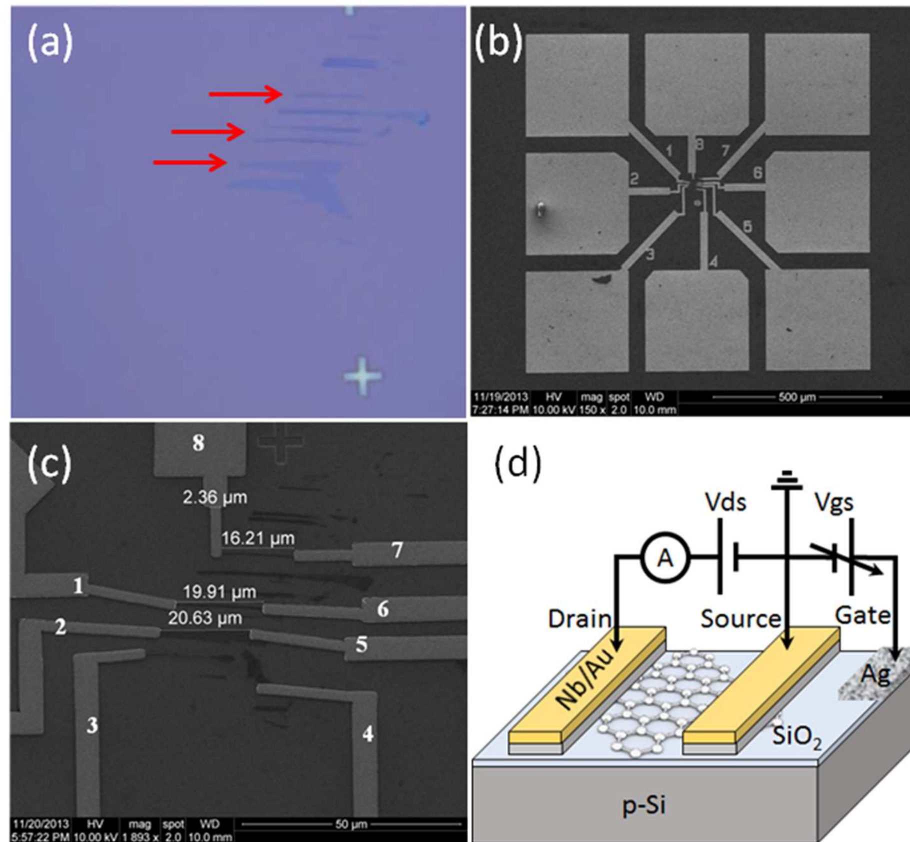

FIGURE 2.5: (a) Optical image of monolayer graphene ribbons under 20× magnification. (b) SEM image of Nb/Au pads and leads used to contact graphene ribbons of (a). (c) Zoom in the central part of (b) showing contacts on graphene ribbons. The graphene flake between leads 1 and 6 was used in this study. (d) Schematic of the transistor consisting of a layer of graphene used as channel with two Nb leads functioning as source and drain and the Si substrate acting as back-gate. The 3-terminal measurement consists in monitoring the source-to-drain current I_{DS} under constant bias, V_{DS} = 3 or 5 mV, while the gate voltage V_{GS} ranges in the interval (-70 V, 70 V).

Electrical measurements were performed at room temperature with the sample under controlled pressure inside a Janis Research ST-500 cryogenic probe station connected to a Keithley 4200 Semiconductor Characterization System (SCS) working in wide ranges of current (100 fA to 0.1 A) and voltage (10 μV to 200 V). The 3-terminal measurement setup is shown in Fig. 2.5(d), which shows also a schematic of the device under study consisting of a layer of graphene used as channel of a FET with two Nb leads functioning as source and drain, kept at constant bias V_{DS} (= 3 or 5 mV). The Si substrate acts as the transistor back-gate and is swept in the voltage interval (-70 V, 70 V). Higher gate voltages were avoided to prevent oxide damage as stresses at $|V_{GS}| > 80$ V systematically cause either gate leakage or

complete oxide breakdown. The electrical measurements were performed after the sample was kept for given time periods under controlled pressure (down to $2.7\cdot10^{-4} mbar$). Prior, the sample had been subjected to other measurements which had the effect of stabilizing electric annealing.

To study the effect of e-beam irradiation on transistors, the SCS was connected to a scanning electron microscope Zeiss LEO 1430 equipped with Kleindeik nanomanipulators MM3A, which allowed in-situ electrical measurements with the sample inside the high-vacuum SEM chamber to prevent adsorbate contamination.

2.3.2 Results and discussion

2.3.2.1 Transfer characteristics

Fig. 2.6(a) shows the I_{DS} - V_{GS} transfer characteristics of the transistor 1-6 of Fig. 2.5, at decreasing pressures and at room temperature. These curves are the fixed drain-bias version of the $I_{DS} - V_{DS}$ output characteristics shown in Fig. 2.6(b), whose linear behavior confirms the ohmic nature of the contacts.

Fig. 2.6(a) evidences a factor-two gate modulation of the current originating from the vanishing density of states of graphene around the Dirac point. In air, the device has a clear p-type behavior with a positive Dirac point corresponding to the conductance minimum beyond +50 *V*. The heavy p-type doping is expected for air exposed graphene and is caused by adsorbed moisture [80] and other chemical residues, such as PMMA not completely removed by acetone during the cleaning process. H_2O, O_2, NO_2 molecules [81-83] and PMMA [84-85] are well known p-dopants. Keeping the sample for many hours in vacuum gradually removes physisorbed chemicals and residues [84,86] and has strong effects on the electrical characteristics of the device. Fig. 2.6(a) shows that vacuum degassing, even at room temperature, shifts the Dirac point towards negative V_{GS}, which corresponds to a gradual transformation of the FET in a device with n-type channel [21]. In our long device, the desorption of acceptor impurities allow the SiO_2 dielectric to take control of the channel doping, which is transformed in n-type. The n-doping is due to charge transfer from surface states in the SiO_2 dielectric to the graphene sheet [87]. After 6 days at low pressure ($\sim3\cdot10^{-4} mbar$) the device reaches a stable configuration and no appreciable changes are observed over time even with a further lowering of the pressure, indicating that most adsorbates and residues have been removed. Remarkably, simple vacuum degassing at room

temperature causes an increase of the mobility (corresponding to steeper V-shaped curves) and a reduction of the minimum conductance. This has been emphasized in Fig. 2.6(c) showing the pressure dependence of the mobility and of the Dirac point (V_{GS}, I_{DS}). Long range scattering by charged impurities [71,88], such as those related to O_2, H_2O or PMMA residues, has a significant impact on carrier motion and on the effective residual carrier density of graphene, n_0, which determines the Dirac point conductivity [89]. n_0 is due to electron/hole puddles induced by the local potential variations of charged impurities [90] rather than to thermal excitation of carrier above the Fermi level. Therefore, the removal of impurities leads to an increase of the carrier mobility for reduced scattering and to a lowering of n_0, i.e. of the minimum conductivity.

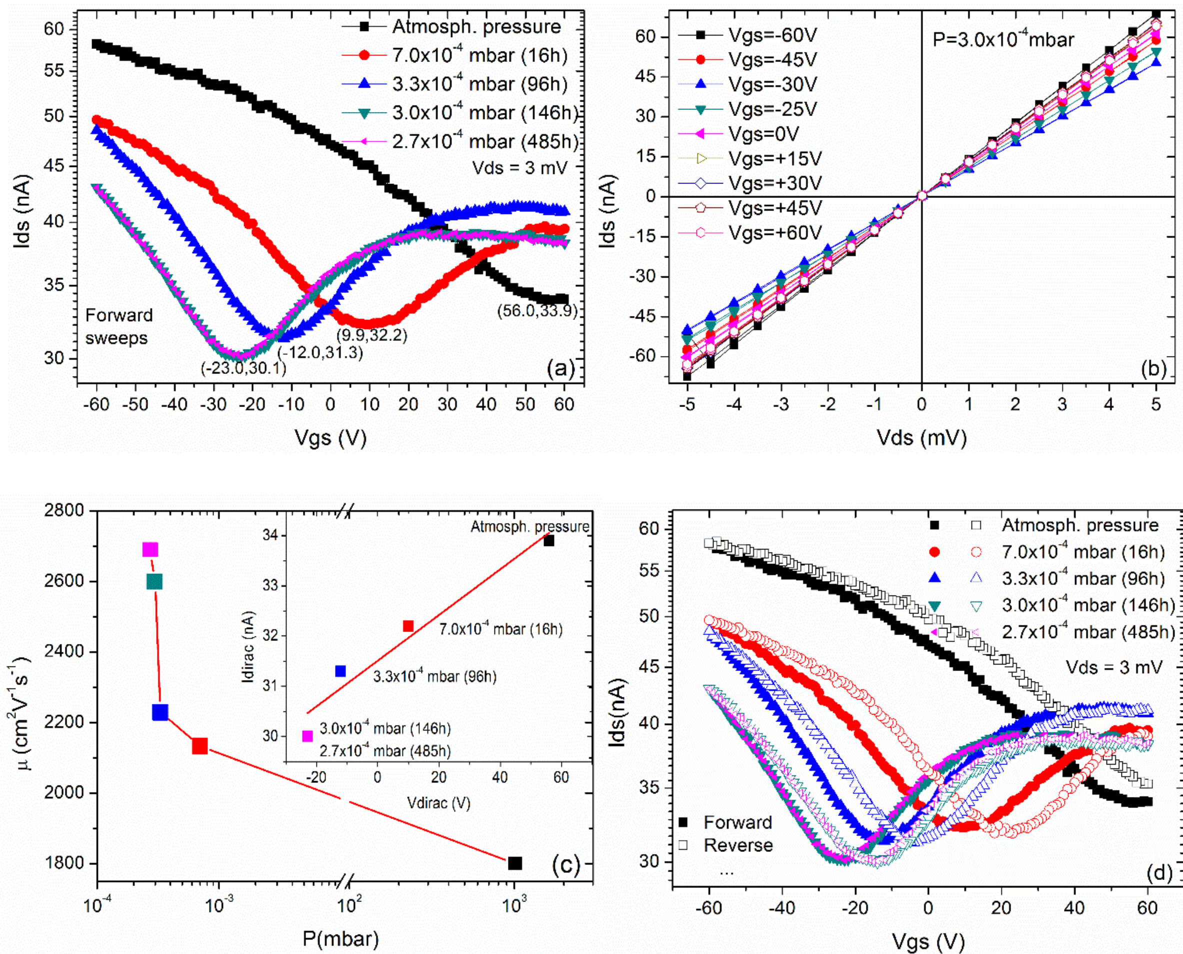

FIGURE 2.6: Electrical characteristics of transistor 1-6 of Fig. 2.5(c). (a) Transfer characteristics $I_{DS} - V_{GS}$ at different pressures and room temperature. (b) Output characteristics $I_{DS} - V_{DS}$ at $3{\cdot}10^{-4}$*mbar*. (c) Mobility and $I_{DS} - V_{GS}$ of the Dirac point at different pressures. (d) Full loop $I_{DS} - V_{GS}$ curves at different pressures showing a decreasing hysteresis with higher vacuum.

Another effect of vacuum degassing is the decreased hysteresis of the $I_{DS} - V_{GS}$ curves as can be observed in Fig. 2.6(d) where full loops with forward and reverse V_{GS} sweeps are plotted.

As we explained before, hysteresis is known to be caused by charge trapping at the graphene/SiO_2 interface and in the dielectric layer [91]. Removal of impurities, and in particular of H_2O which plays a key role in the charge transfer during a V_{GS} sweep [92], obviously results in reduced hysteresis.

2.3.2.2 Contact resistance

As already mentioned, with a two-point setup, the total resistance between source and drain of the graphene FET, calculated as $R_{tot}=V_{DS}/I_{DS}$, is the sum of the metal resistance (which is here negligible), the total contact resistance R_{con} and the graphene channel resistance R_{ch} (both R_{con} and R_{ch} can depend on V_{DS}), $R_{tot} = R_{con}+ R_{ch}$.

The measured R_{tot} is shown in Fig. 2.7(a), where two main features can be noted: an asymmetry between the n and the p-branch and a resistance plateau in the n-branch, which does not have a counterpart in p-branch.

The asymmetry can be characterized by introducing an “odd resistance” R_{odd} defined as:

$$R_{odd} = \frac{R_{tot}(\Delta V_{GS}) - R_{tot}(-\Delta V_{GS})}{2}, \tag{2.5}$$

for $\Delta V_{GS} = V_{GS} - V_{Dirac} > 0$. R_{odd}, shown in Fig. 2.7(b), is positive and has a quadratic dependence on the gate voltage. As we will discuss in detail later, asymmetry is mainly caused by additional p-n junctions created by doping at the contacts [93-94]. Then, since R_{odd} is an effect of the contacts and is well fitted by a 2nd order polynomial, we admit a quadratic dependence of R_{con} on V_{GS}:

$$R_{con} = R_c + \alpha(V_{GS} - V_{Dirac}) + \beta(V_{GS} - V_{Dirac})^2, \tag{2.6}$$

with R_c, α and β parameters that we experimentally determine. Such dependence can be easily justified considering the non-linear gate dependence and the spatial inhomogeneity of carrier density in the contact region [11]. We follow the model of Kim et al. [95] to write the conductivity of graphene in the channel as:

$$\sigma_{ch} = en_{tot}\mu\,, \tag{2.7}$$

where:

$$n_{tot} = \sqrt{n_0^2 + n^2}\,, \tag{2.8}$$

$$n = \frac{C_{ox}(V_{GS} - V_{Dirac})}{e}. \quad (2.9)$$

n_{tot} is the gate-dependent total carrier concentration, n_0 is the carrier density at the Dirac point, n is the excess carrier induced by V_{GS}, μ is the mobility (that, in graphene, should be the same for electrons and holes) and $C_{ox}=\varepsilon_{SiO2}/d=1.15\cdot 10^{-8} F/cm^2$ is the capacitance per unit area of the SiO_2 layer of thickness d.

Using eqs. (2.6) - (2.9), we express the total resistance as:

$$R_{tot} = R_c + \alpha(V_{GS} - V_{Dirac}) + \beta(V_{GS} - V_{Dirac})^2 + \\ + \frac{L}{W}\frac{1}{e\mu\sqrt{n_0^2 + [(V_{GS} - V_{Dirac}) \cdot C_{ox}/e]^2}}, \quad (2.10)$$

where L and W are the channel length and width, respectively. The fit of (2.10) to the experimental data, shown in Fig. 2.7(a), yields $R_c \approx 60\ k\Omega$ (i.e. ~30 $k\Omega$ at each contact, corresponding to a specific contact resistivity $\rho_c=R_cW \approx 24\ k\Omega\mu m$) with less than 10% variation due to the gate-dependent terms and a mobility $\mu \approx 2600\ cm^2V^{-1}s^{-1}$. The fit results quite accurate also in the plateau region at $V_{GS} > 35\ V$.

Fig. 2.7(c) shows the channel conductivity obtained by eliminating R_{con} (V_{GS}), as expressed by eq. (2.6), from the total measured resistance:

$$\sigma_{ch} = en_{tot}\mu = \frac{1}{R_{tot} - R_{con}}\frac{L}{W}. \quad (2.11)$$

Following the common practice of using the slope of σ_{ch} - V_{GS} away from the Dirac point (where $n_0 < n$) to estimate the mobility as:

$$\mu = \frac{1}{C_{ox}}\frac{d\sigma_{ch}}{dV_{GS}}, \quad (2.12)$$

we obtain a hole mobility μ_h= 2850 $cm^2V^{-1}s^{-1}$ higher than the electron one μ_e= 2350 $cm^2V^{-1}s^{-1}$ in the channel. The average mobility $\mu_{avg}=(\mu_e + \mu_h)/2$ = 2602 $cm^2V^{-1}s^{-1}$ is consistent with the value previously estimated. Although the difference μ_h - μ_e may be exaggerated by the method which does not take into account the carrier inhomogeneity along the channel (which can be particularly important in the n-branch where a p-n-p structure is formed, as we will see later), this results suggests that there is a mobility contribution to the n and p branch asymmetry. Higher hole mobility has often been measured in graphene transistors [91,96-97]; one

plausible explanation is the different scattering cross section for electrons and holes by charged impurities, according to which the massless carriers are scattered more strongly when they are attracted to a charged impurity than when they are repelled from it [98]. In the case under study, after desorption of chemicals and residues, the charged impurities are mainly the positive charges stored in SiO_2 dielectric.

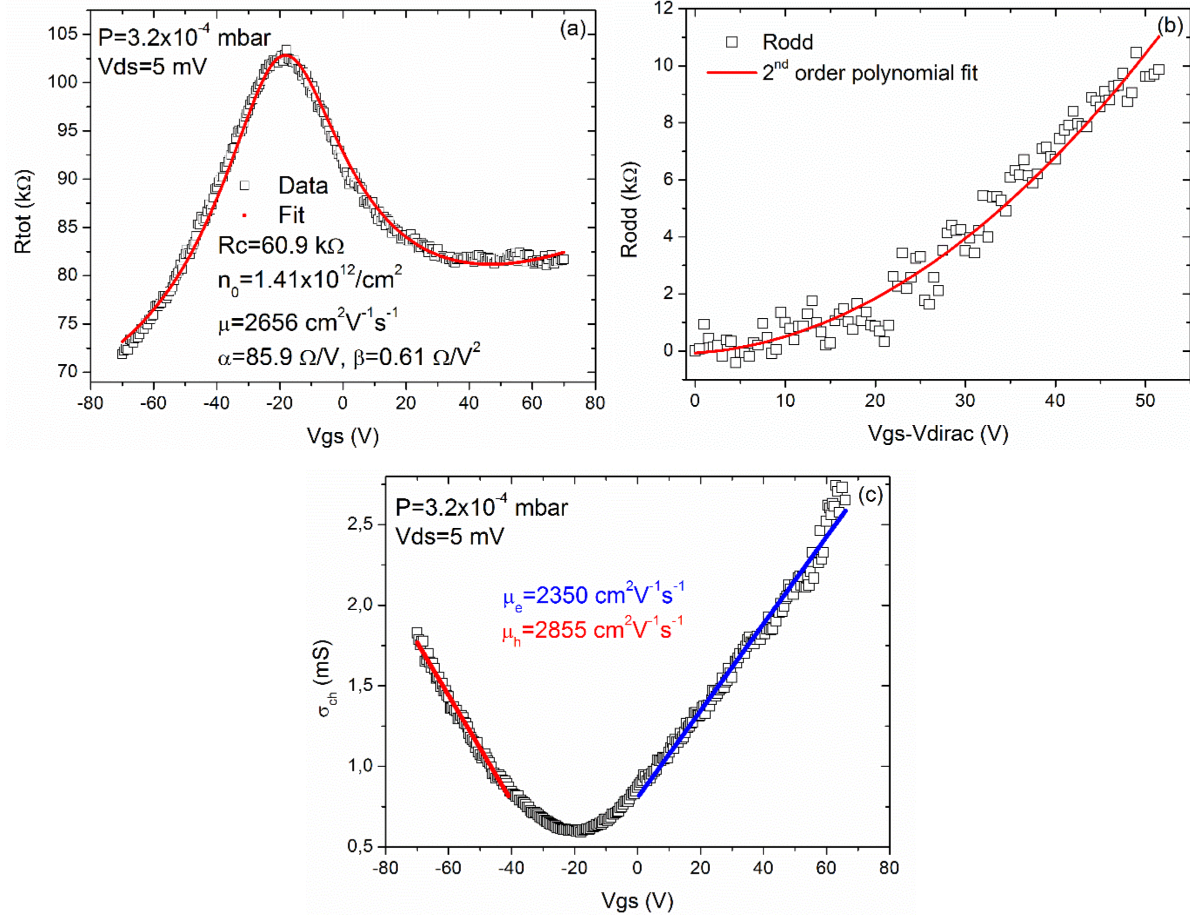

FIGURE 2.7: Electrical characteristics of transistor 1-6 of Fig. 2.5(c). (a) Total resistance R_{tot} as a function of V_{GS} (at V_{DS} =5 mV and $P = 3.2\cdot 10^{-4} mbar$) and eq. (2.10) fit (solid line). (b) R_{odd} vs V_{GS} with 2nd order polynomial fit. (c) σ_{ch} - V_{GS} curve obtained by subtracting the contact resistance contribution and linear fit to estimate electron and hole mobilities.

The relatively high specific contact resistance as compared to the benchmark of $\rho_c = 100\ \Omega\mu m$ for good contacts can barely be ascribed to the roughness and grain size of the Nb film, which can be only a minor contributor (large grains and rough surface go in the direction of reducing the effective contact area and increasing the contact resistance). Although expected in minimal amounts, impurities non-removed by the vacuum degassing and trapped under the metal as well as defects created by the sputtering process are possible additional sources. Nb is an easily-oxidizable metal and could easily react with residuals O_2 or

H_2O molecules. Indeed we believe that an important source of resistance is the strain induced in graphene by Nb/Au leads. Tensile strain in graphene has been observed to weaken the C-C bond and lower the vibration frequency, thus causing a red shift of the 2D and G bands [99]. Theoretically, it has been pointed out that uniaxial and shear strains may move the Fermi level crossing away from the K points while preserving the cone-like energy dispersion [100]. Scanning tunneling microscopy (STM) studies on graphene have revealed a correlation between local strain and increased tunneling resistance [101]. Uniaxial tensile strain greater than 3% has been proven to cause a dramatic increase of the graphene resistance [102]. A confirmation of stress in our Nb/Au film, which is transmitted to the graphene underneath, is the observation of metal peeling off which sometimes happened during the fabrication or the measurement process. The strain and the high contact resistance point towards a weak bonding between graphene and Nb, with a likely high Nb/graphene separation on the atomic scale (> 3 $\AA$). The weak bonding, which in the most severe case can pose practical adhesion problems, favors Fermi level depinning at the contact but preserves the conical electronic structure of graphene.

As we mentioned before, another important fact to consider is the Nb-graphene workfunction mismatch. Such a mismatch provokes charge transfer across the interface, forms an interface dipole with an accompanying potential step ΔV and shifts the graphene Fermi level [19]. The transferred charge, which results in local doping of graphene, is not confined under the contacts but can extend hundreds nanometers in the channel [103] and if the Fermi level is not pinned, the gate voltage is able to further tune the charge density of graphene in the contact region [18,104].

A positive R_{odd} is typically obtained when $\Delta\Phi=\Phi_M - \Phi_{G0} < 0$ where Φ_M and $\Phi_{G0} = 4.5eV$ are the workfunctions of the metal and of the intrinsic graphene, respectively [93]. Metals with a higher workfunction than graphene tend to subtract electrons from graphene, which becomes locally p-doped. Nb has a workfunction in the range 3.95 - 4.87 eV [105] and can behave both as acceptor and donor for graphene. According to Leblanc et al. [106] the electron workfunction of pure Nb highly depends on the crystal orientation, with the highest value belonging to the {1,1,0} orientations and the lowest one for the {001} orientations. An appreciable increase of a Nb film workfunction has also been reported for increasing oxygen content [107].

For the measured device the positive R_{odd} and the shape of the transfer characteristic strongly indicates that graphene at the contacts is p-type. A Nb film with lower workfunction and donor behavior can be expected as well and would result in a y-axis specular transfer

characteristic with a resistance plateau in the p-branch. Actually, as already mentioned, Nb contacted graphene FETs with such characteristic have been reported by Rickhaus et al. [24]. We remark that the sign and amount of doping is a multi-factor effect. Metal-graphene spacing, as affected by strain or impurities and defects, structural modifications, wave function hybridization, etc. may contribute to doping other than workfunction difference. Based on density functional calculations, Giovannetti et al. [19] showed that the formation of the interfacial dipole (experimentally proven by Pi et al. [108]) promotes n-type doping for strongly chemisorbed metals (metal graphene separation ~ 2Å) with a workfunction of up to 5.4 *eV*. The same model predicts that p-doping is dominant for most metals when a weak chemical interaction, corresponding to high metal-graphene separation (> 3-4 Å), takes place. The latter is the situation that we have been depicting for the device under study. As a matter of fact, p-doping has been observed even with Ti contacts despite the strong donor character given to it by its low workfunction [12,109].

A qualitative model explaining the whole I_{DS} - V_{GS} behavior of the device is presented in Fig. 2.8. It consider p-doping and Fermi level depinning as expected from the considerations made so far. For $V_{GS} < V_{Dirac}$, the band alignment of graphene under the contacts and in the channel is that shown in the inset (1), corresponding to a p-p$^+$-p structure.

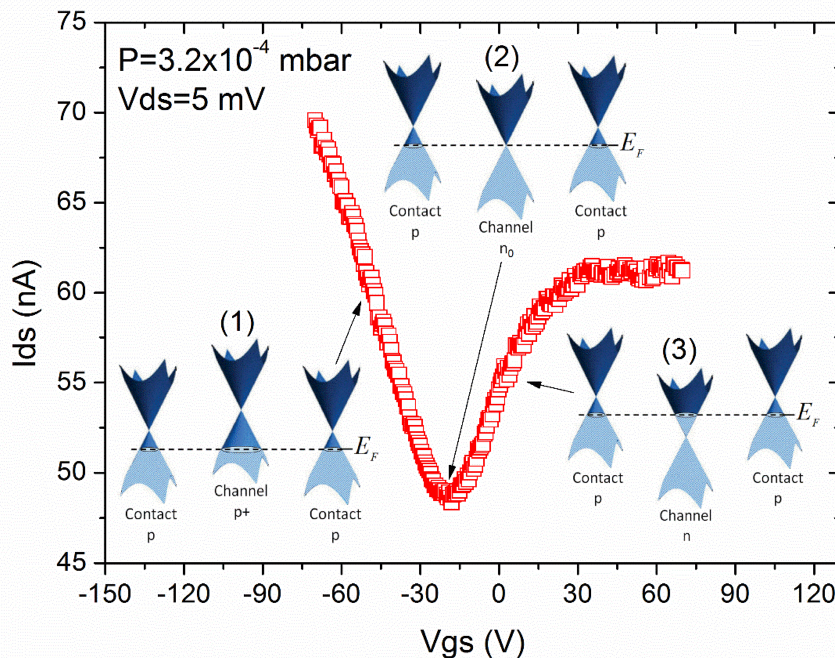

FIGURE 2.8: Fermi level for graphene at the contacts and in the channel accounting for the current behavior as a function of V_{GS}. It is assumed that the Fermi level is not pinned at the contacts, where p-doping occurs.

The p-type conductance of the device is strongly increased by the negative V_{GS} which augments the available *DOS* both in the channel and under the metal. In the contact region, the metal-graphene workfunction difference and the screening effect of the metal make the gate control of the carrier concentration less effective than in the channel. A minimum of conductance is achieved when, increasing V_{GS}, the graphene in the channel reaches the Dirac point, while the contact remains p-type for the effect of contact doping. A p-i-p structure (i=intrinsic) is formed as shown in inset (2). For $V_{GS} > V_{Dirac}$, n-doping is induced in the channel and the device becomes a p-n-p structure. The appearance of more resistive p-n junctions [110] in the n-branch as opposed to the p-p^+ counterparts in the p-branch is the origin of the observed asymmetry in the V-shaped transfer characteristics. The conductance is initially driven by the *DOS* of the channel, until the channel doping reaches a level comparable to that of the graphene near the contacts. From this point on, the limitation on the conductance is set by the contacts. The gate voltage tends to shift the Fermi level at the contacts upwards, that is to reduce the hole concentration and increase the contact resistance. The increasing contact resistance counter-balances the decreasing channel resistance and this compensation mechanism results in the observed plateau. In this interpretation, more push of the positive gate voltage would shift E_F further up, to the Dirac point at the contacts, and create a second conductance minimum. A careful look at the curves of Fig. 2.6(a) shows a gradual drop of the current towards high positive V_{GS} which seems to confirm this expectation.

At the plateau, $R_{tot} \approx 82\ k\Omega$. Assuming that the total resistance is dominated by the contacts, using the measured electron mobility ($\mu_e = 2350\ cm^2V^{-1}s^{-1}$), we can estimate a carrier density in graphene of ~ $3.4\cdot10^{12}/cm^2$, which for $n_0 = 1.41\cdot10^{12}/cm^2$ and from eq. (2.8) corresponds to a gate induced excess electrons of $3.1\cdot10^{12}/cm^2$. Such a carrier concentration is obtained when the graphene Fermi level with respect to the conical point is:

$$E_F = \hbar v_F \sqrt{\pi n} \approx 0.21\ eV \tag{2.13}$$

(here $v_F = 10^6\ m/s$ is the Fermi velocity in graphene). Considering $\Phi_{G0} = 4.5eV$ this suggests a Nb workfunction $\Phi_{Nb} \geq 4.7eV$. The inequality originates from the fact that, according to Giovannetti et al. model [19], the metal workfunction would be $\Phi_{Nb} = \Phi_{G0}+E_F+e\Delta V$, where the charge dipole voltage $\Delta V > 0\ V$ is a decreasing function of the metal/graphene separation (and should be close to zero in the present device).

2.3.2.3 Effect of electron beam irradiation

In the following, we consider the effect of electron beam irradiation on the transistor 1-6 of Fig. 2.5(c). In particular, we consider electron beam energy up to 10 *keV*, i.e. the energy range typically used for SEM imaging. Larger energy (about 30 *keV*) is normally used for e-beam lithography or imaging in STEM mode. The irradiation was performed on an area of 20 μm × 20 μm, covering most of the graphene channel, with constant beam current I_{beam} = 0.2 *nA*. We used an exposure time of 10 *s*, which resulted in an electron irradiation dose of about 30 e^{-}/nm^{2}. Differently from other works [45], we performed post-irradiation electrical measurements directly in the SEM chamber in high vacuum (10^{-7} *mbar*), thus avoiding the effects of air.

Results obtained in six successive electrical sweeps, after a 10 *s* electron irradiation at 10 *keV*, are reported in Fig. 2.9(a). The complete (forward and backward) sweeping between 0 *V* and -70 *V* evidences an important hysteresis that decreases with successive electrical sweeps.

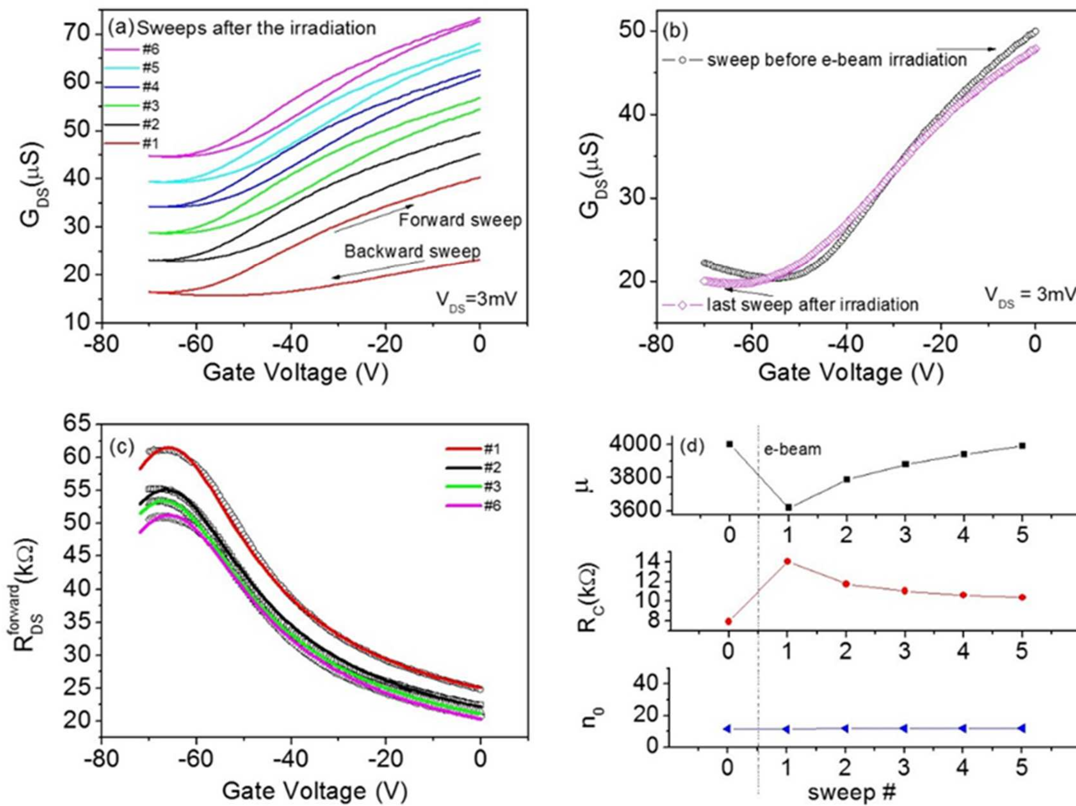

FIGURE 2.9: Effect of electron irradiation on R_{DS} vs. V_{GS} of the transistor 1-6 of Fig. 2.5(c). (a) Six successive sweeps recorded soon after the electron irradiation. Curves have been shifted for clarity. (b) Comparison of the sixth sweep after the 10 *s* e-beam exposure with that measured on unexposed device. (c) Forward sweep of selected measurements and relative fitting curves according to the model [95].(d) Summary of parameters extracted by fitting of the curves corresponding to forward sweeps.

The appearance of the hysteresis is easily explained by mobile electrons that are trapped in the gate oxide during e-beam exposure, which screen the gate voltage, while the hysteresis reduction can be caused by their withdrawal by the channel during the successive voltage sweeps [91,92]. By comparing the transfer characteristic before the electron irradiation to the sixth sweep measured after the 10 *s* exposure (Fig. 2.9(b)), we observe that the device has almost returned to its initial state apart a marginal shift of the Dirac point.

To quantitatively analyze the evolution after e-beam exposure (see Fig. 2.9(c)), we used the model of Kim et al. [95] to estimate the transport parameters, which are summarized in Fig. 2.9(d). The carrier mobility is reduced by the 10 *s* e-beam irradiation, from 4000 $cm^2V^{-1}s^{-1}$ to about 3600 $cm^2V^{-1}s^{-1}$ (as obtained from the first sweep measurement). The initial value is restored by the successive sweeps.

A consistent behavior is shown by the total resistance, which is increased by the irradiation and recovers with increasing number of sweeps. The increase in total resistance, as a consequence of the e-beam irradiation, has also been observed on chemical vapor deposition (CVD) grown graphene [111]. Fig. 2.9(d) reports the effect of irradiation on the contact resistance that is increased by about 70% by the exposure and is smoothly restored by successive sweeps.

Noticeably, the irradiation seems to have a negligible effect on the intrinsic carrier concentration n_0.

Mobility and resistance degradation can be explained as increased long-range coulomb scattering [88] by electrons stored in the gate oxide during e-beam exposure (damaging of graphene seems to have a minor contribution); such electrons are gradually removed by voltage application during successive sweeps and pristine conditions are partially recovered.

2.4 Side-gate GFETs

2.4.1 Devices fabrication and measurement setup

Devices have been produced at Exeter University (UK). They were fabricated by standard electron-beam lithography (EBL) on heavily p-doped Si substrates (resistivity is 0.001--0.005 *Ωcm*) capped with a 290 *nm* thermally grown SiO_2 layer. Single and bilayer graphene flakes were exfoliated from highly oriented pyrolytic graphite and identified under optical microscope using contrast analysis under green light [22-23]. The selected graphene flakes

(Fig. 2.10(a)) were patterned in a single lithographic step to define channel and gate. Unwanted graphene was removed by O_2 plasma etch (Fig. 2.10(b) and Fig. 2.10(c)). Metal contacts (20 *nm* Cr/90 *nm* Au) were defined in a successive EBL step by metal evaporation and lift-off (Fig. 2.10(d)). To achieve low contact resistance, metal was evaporated at a low rate (0.2-0.4 *Å/s* for the Cr adhesion layer and at 0.4-0.9 *Å/s* for the capping Au) and at a pressure of $4\text{-}8 \cdot 10^{-6}$ *Torr*.

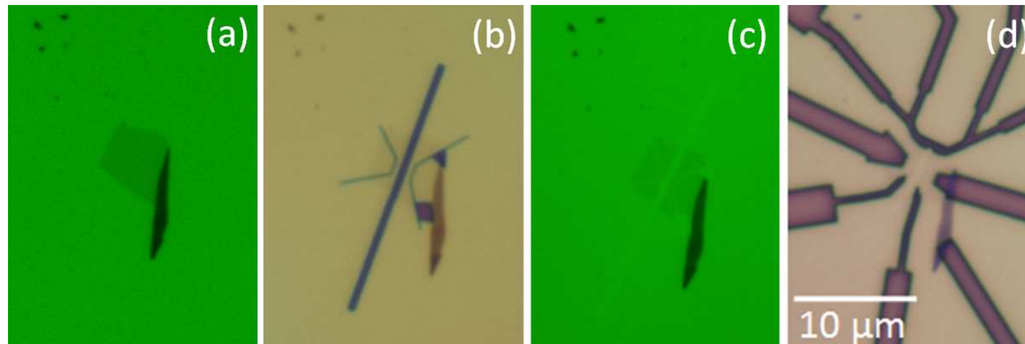

FIGURE 2.10: Optical image (under green light and magnification 50×) of an exfoliated graphene bilayer as deposited (a), covered by developed PMMA after e-beam exposure to define gate and source/drain regions (b), as patterned after O_2 plasma exposure and PMMA removal (c), covered by developed PMMA after e-beam exposure for contact definition (d).

The layout/schematic and the scanning electron microscope (SEM) image of a typical device are shown in Figs. 2.11(a) and 2.11(b). The device consists of two side-gated transistors on a Si substrate (back gate), connected in series by a metal line. The two side gates are controlled separately and can be biased to make the two transistors p- and n-type, respectively, thus enabling a CMOS graphene device.

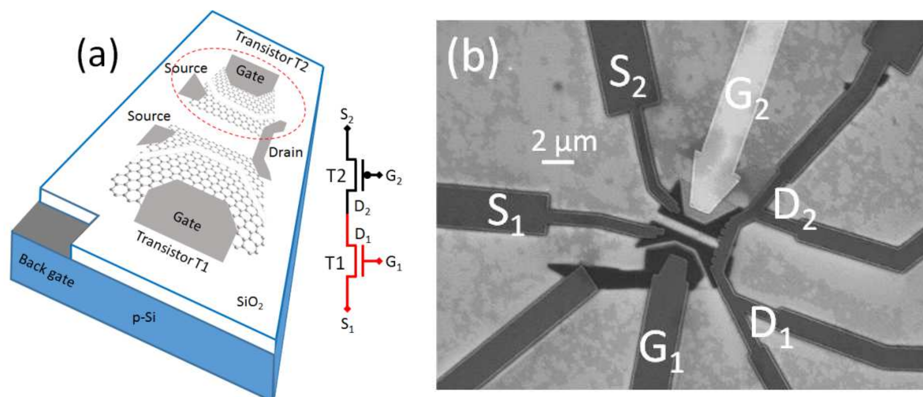

FIGURE 2.11: (a) Layout and schematic of two side-gated graphene transistors (T1 and T2) connected in series. The transistors share the back-gate and are endowed with independent side-gates. (b) SEM image of the device in (a) showing electrically connected metal leads (darker lines; the gate G_2 of T2 is floating, thus appears lighter in the SEM image).

The side-gate architecture offers easy control of the transistor dimensions, as the gate-to-channel distance or the channel width, which are only limited by the resolution of the lithography/etching process. In our design, we enlarged the source/drain regions to reduce the external resistance. Furthermore, we shaped the gate to maximize its overlapping and prevent the formation of unwanted high resistive paths, often included in top-gated devices. To achieve devices for low-power applications working with biases below 1 *V* and maximize the modulation effect of the side-gate, we chose a gate-to-channel distance d = 100 *nm* and a channel width w = 500 *nm*.

Electrical measurements were performed in a Janis probe station at a pressure of ~ 1 *Torr*. To desorb adsorbates and achieve a clean SiO_2/vacuum interface as gate dielectric, we applied vacuum annealing at ~10^{-6} *Torr* and room temperature for more than 3 days in a nanoprobe-equipped high-vacuum Zeiss SEM chamber. The gate leakage and field emission measurements were then performed in-situ. In both cases, we used a Keithley 4200 SCS as source-meter unit.

2.4.2 Results and discussion

2.4.2.1 Transfer characteristics

Fig. 2.12 shows the effect of the side-gate, and of the back-gate for comparison, on the channel conductance of the transistor T1 of Fig. 2.11. The drain current-voltage relation (I_{DS}-V_{DS} curve, Fig. 2.12(a)), measured at different side-gate biases V_{GS} and for grounded source and floating back-gate, shows a linear behavior. The minimum source-to-drain resistance, which includes the channel and the two contact resistances, is ~ 50 $k\Omega$ and is dominated by the channel. Measurements on test structures fabricated simultaneously and on the same chip of the device of Fig. 2.11 confirmed a contact resistance of the order of 1 $k\Omega/\mu m$, consistently with previous experiments [16-17,27-28,30]. The modulation of the graphene conductance G by the side-gate is shown by the transfer characteristic (G-V_{GS} curve) displayed in Fig. 2.12(b), which shows a 35% variation on an interval of ~ 0.5 *V*. As common for air and PMMA exposed graphene transistors [28], the neutrality (Dirac) point is located at positive V_{GS} (~ 0.35 *V*), which indicates a p-channel device. The inset of the Fig. 2.12(b) shows the conductance behavior in a full loop of V_{GS} values and shows a significant hysteresis between the forward and the reverse sweep. We characterize the hysteresis by the ratio of the forward-reverse voltage shift δV_{GS} to the width ΔV_{GS} of the V-shaped curve, at a given G,

and find $\delta V_{GS}/\Delta V_{GS}\big|_{G=15\mu S} \approx 20\%$. For comparison, Fig. 2.12(c) shows the transfer characteristic generated by the back-gate, with floating side-gate, and we observe a similar hysteretic behavior with higher $\delta V_{GS}/\Delta V_{GS}\big|_{G=15\mu S} \approx 39\%$ (see inset of Fig. 2.12(c)). As we stated many times, the hysteresis is attributed to charge transferred and stored in traps present in the gate dielectric as well as induced by polymer residues in the processing or by unwanted contamination, e.g. adsorbates or moisture [18,91-92]. Residues, adsorbates or moisture may result particularly dangerous for side-gate devices, especially if localized at the graphene edges or in the channel-gate spacing, since they can form dipoles, which disturb the local electrical field and deteriorate the gating effect, or contribute to the gate leakage current at higher electric fields. We performed measurements in vacuum and kept the side-gate bias low to prevent leakage, which was always below the floor noise of the experimental setup.

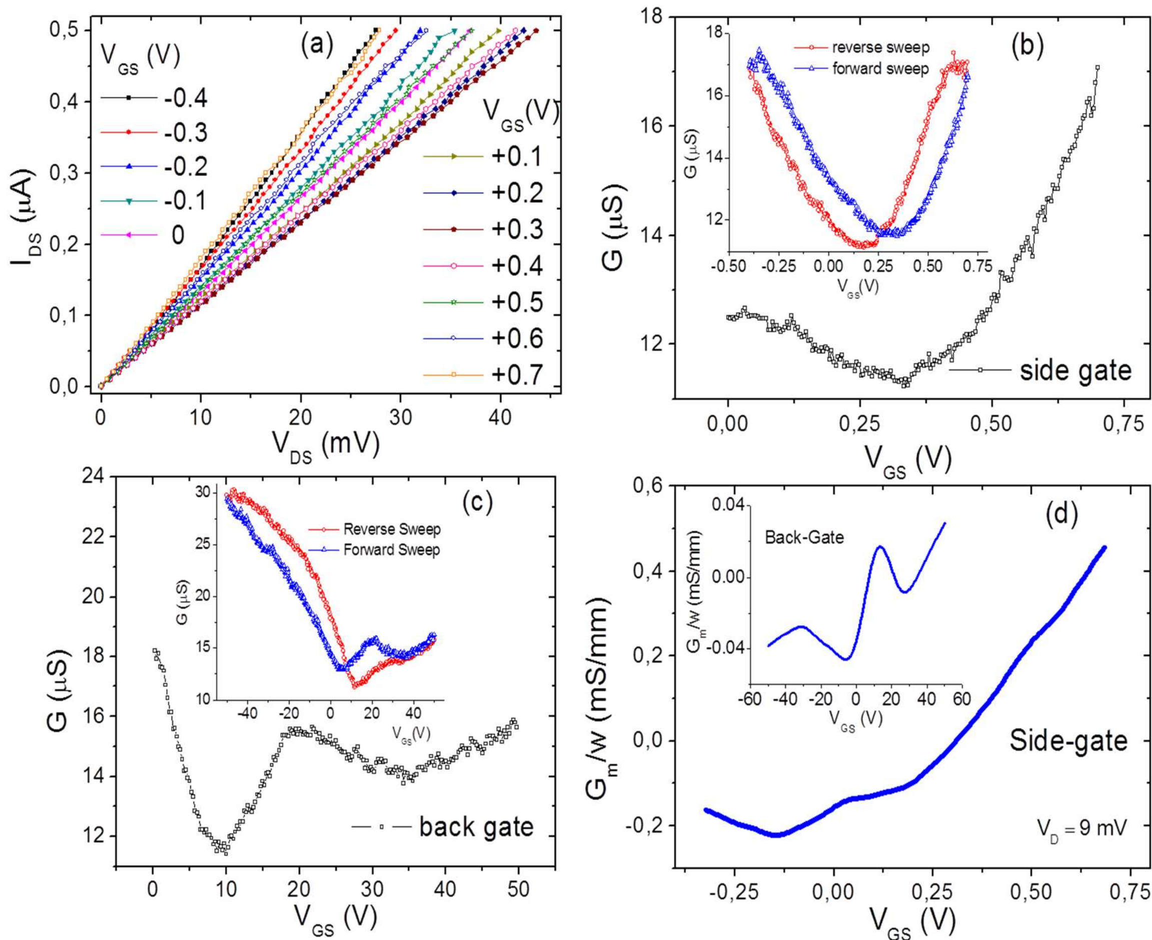

FIGURE 2.12: Electrical characteristics of the transistor T1 of Fig. 2.11. (a) Output characteristics (I_{DS}-V_{DS} curves) for floating back-gate. (b) Transfer characteristic (G-V_{GS} curve) obtained at V_{DS} =9 mV and floating back-gate. (c) Transfer characteristic as a function of the back-gate for floating side-gate. Insets of (b) and (c) show the transfer characteristics in a reverse-forward loop. (d) Side-gate and back-gate transconductance, normalized by channel width.

Fig. 2.12(d) shows the transconductance, $G_m = dI_{DS}/dV_{GS}\big|_{V_{DS}=9mV}$, normalized by channel width [55], for side- and back-gate. The transconductance is a useful parameter in the saturation regime, when a FET is used as an amplifier [114]. Here, saturation is not achieved; nonetheless, we use the transconductance to compare the side- and back-gate ability to convert a voltage to current. Fig. 2.12(d) shows that in the narrow interval $|V_G|<1V$ the side-gate efficiency is 5 to 10 times higher than the back-gate on a 50 times larger voltage interval.

The back-gate sweep (Fig. 2.12(c)) confirms the p-type behavior of graphene with a Dirac point at $V_{GS} \approx 10\ V$ and the wider sweeping range evidences a second Dirac point. As we stated many times, this feature has been explained in terms of graphene doping by the contacts and Fermi level de-pinning [15,18,22,115-118]. A careful comparison of the shape of the curves in the insets of Fig. 2.12(b) and Fig. 2.12(c), over the same current range, seems to exclude the appearance of a second dip in the side-gate transfer characteristics, and, in fact, we did not find any evidence of it over a sweep up to 3 *V*.

2.4.2.2 Leakage current and field emission

To gain insight on the side-gate voltage that the device can withstand and to investigate the dielectric rigidity of the SiO_2/vacuum gate dielectric, we measured the planar current across the channel-gate gap till the appearance of a breakdown and beyond it. Such experiment was realized in high vacuum to remove surface moisture and adsorbates, which could provide extra leakage paths.

We started checking the vertical leakage, which is the current between the channel or the side-gate and the Si substrate, and we found it below the noise limit of 100 *pA* of our setup for biases up to 50 *V*. We did not perform measurements at higher voltages to avoid long and aggressive electrical stresses, which could trigger SiO_2 degradation mechanisms. For the same reason, to apply a higher voltage in the planar direction, between the channel and the side-gate, we decided to bias the back-gate at 50 *V* and then ramp the drain voltage V_{DG} up to 100 *V*, while the side-gate was grounded (Fig. 2.13(a)). In such a way, the maximum vertical stress was never higher than 50 *V*; besides, the back gate bias made graphene n-type, a favorable condition for leakage and electron emission measurements.

Fig. 2.13(b) shows the current in the planar direction measured across the 100 *nm* gap between the side-gate and channel. The current is below the noise floor of the experimental setup up to ~ 15 *V* and increases rapidly at higher V_{DG}, while the back gate current keeps practically constant below 100 *pA*.

The curve labelled as 2nd sweep in Fig. 2.13(b) represents the first full sweep after a few stabilizing cycles at lower voltages. The current emerges from the noise floor and increases over 3 decades up to ~ 60 *V*, before going through a dramatic change with a steeper rise up to 10 μA at 70 *V*. After that, a slow degradation happens. The appearance of a degradation mechanism is confirmed by the following sweep (3rd sweep), where the current appears at a higher voltage, V_{DG} ~ 35 *V*, and increases steadily and at a similar rate of the first part of the 2nd cycle without any significant change.

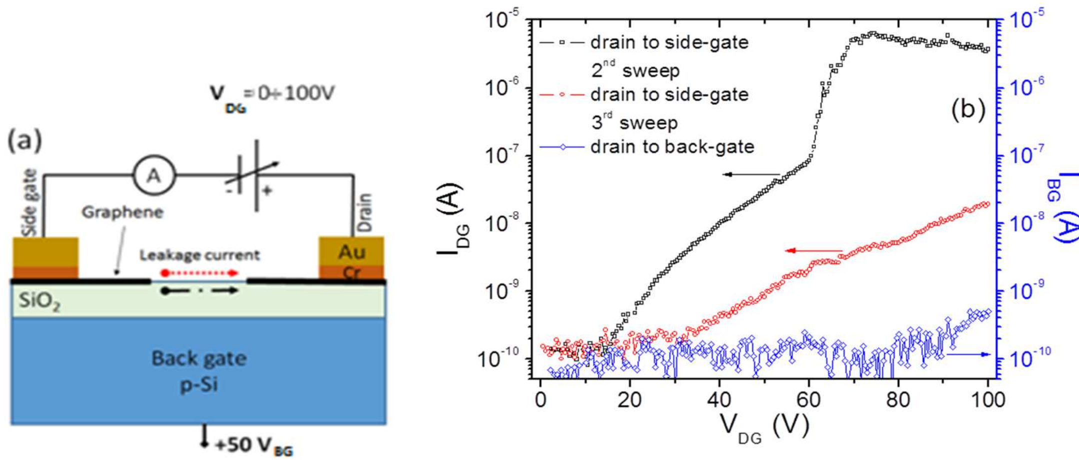

FIGURE 2.13: (a) Measurement schematic of the side gate-channel leakage current. Measurements were performed in a SEM chamber at high vacuum (10^{-6} *Torr*). (b) Planar current between channel and side-gate (I_{BG}, left axis) and back-gate current (I_{BG}, right axis) vs. drain bias (V_{DG}) for the transistor T1 of Fig. 2.11. The 2nd sweep shows two transport regimes, before a high current degradation, which occurs at $V_{DG} > 70$ *V* and results in reduced current in the following 3rd sweep.

The rapid increase of the current is typical of tunneling phenomena. However, the slower growing rate of the current below 60 *V* in the 2nd sweep, and after degradation in the 3rd cycle, seems to indicate that a different mechanism is taking place. We compared the experimental data of Fig. 2.13(b) to the predictions of different transport models, as thermionic, Fowler-Nordheim (FN) and Frenkel-Poole (FP) emission or ohmic and space-charge-limited conduction [114,119].

Differently from Wang et al. [66], who reported current-voltage characteristics governed by the space-charge limited flow of current at low biases, on a device with similar layout but different fabrication process, which can affect the SiO_2 surface, we found that a far-better fit for $V_{DG} < 60$ *V* is provided by the FP model [114]:

$$I_{DG} \propto V_{DG} \exp\left(\frac{q}{kT}\left(2a\sqrt{V_{DG}} - \Phi_B\right)\right), \tag{2.14}$$

where q is the electron charge, k is the Boltzmann constant, T the temperature, $a = \sqrt{q/(4\pi\varepsilon_0\varepsilon_r d)}$ is the Frenkel-Poole constant, ε_r the dielectric constant of SiO_2, d the insulator thickens and Φ_B is the trap barrier. The good fit is shown in the plot of $ln(I_{DG}/V_{DG})$ vs. $\sqrt{V_{DG}}$ of Fig. 2.14, corresponding to a straight-line whose intercept can be used to evaluate $\Phi_B \sim 0.8\ eV$, both when using the 2nd or the 3rd sweep. According to FP model, electrons can be injected in trap states in the bandgap of the SiO_2, where they can move in a sequence of trapping and de-trapping events, facilitated by the electric field, which reduces the barrier on one side of the trap. For the FP conduction mechanism to occur, the trap must be neutral when filled with an electron, and positively charged when the electron is emitted, the interaction between positively charged trap and electron giving rise to a Coulombic barrier.

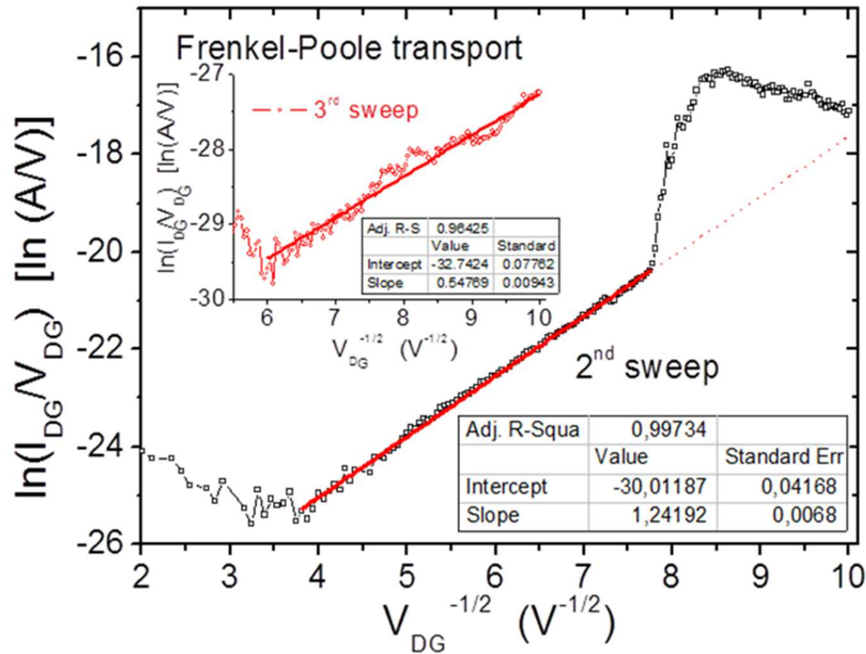

FIGURE 2.14: Fit of Frenkel-Poole model to data of Fig. 2.13(b). The model is in excellent agreement with experimental data in the range 15-60V for 2nd sweep and in the range 35-100 V for 3rd sweep.

At higher voltages, $V_{DG} > 60\ V$, the FN emission in vacuum becomes the model giving the best description of the data. The FN current, as already exposed in chapter 1, is described by [67]:

$$I_{DG} \propto a\frac{1}{\Phi}\left(\frac{\beta V_{DG}}{d}\right)^2 exp\left(-\frac{b\Phi^{3/2}d}{\beta V_{DG}}\right), \tag{2.15}$$

where $a = 1.54\cdot10^{-6}\ AeVV^{-2}$ and $b = 6.83\cdot10^{9}\ eV^{-3/2}Vm^{-1}$ are constants, Φ is the barrier height (graphene workfunction), d is the inter-electrode distance and β is the field enhancement factor on the sharp edge of graphene. According to eq. (2.15), a plot of $ln(I_{DG}/V^{2}_{DG})$ vs. $1/V_{DG}$ (Fig. 2.15) is straight-line whose slope and intercept are related to β and Φ.

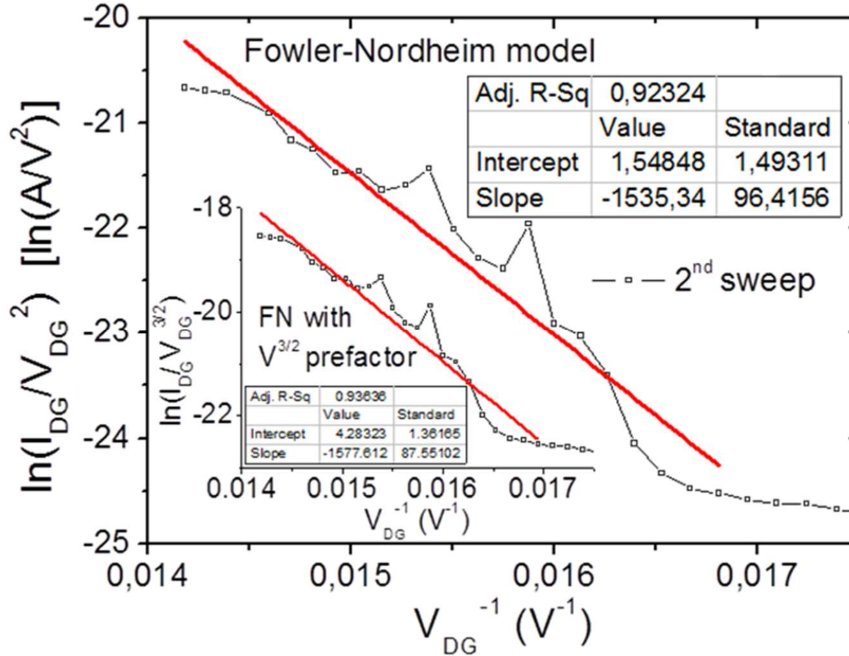

FIGURE 2.15: Fit of Fowler-Nordheim field emission model to the data of the 2nd sweep in the range 60-70 *V* of Fig. 2.13(b).

Even though eq. (2.15) is typically used, it has been suggested that the pre-factor V^{2}_{DG} should be replaced by $V^{3/2}_{DG}$ for graphene [120]. We checked FN model against other possible mechanisms and, despite the low statistics, we found that eq. (2.15), both in the original or modified version, is the closest to the experimental behavior. Hence, we concluded that FN injection in vacuum is the main leakage mechanism at high fields. The field enhancement factor at the edge of graphene, obtained from eq. (2.15) with $\Phi = 4.5\ eV$, is ~ 4.

Despite the atomically sharp edge only a modest amplification factor is achieved in our configuration, as confirmed also by a finite-element simulation of the field (MAXWELL software), shown in Fig. 2.16(a). The low value of β is caused by the non-favorable edge-to-edge configuration of the two graphene flakes on the substrate and is affected by the small channel-to-gate distance, since the field enhancement factor is known to grow with the spacing between the anode and the cathode [121-122].

As shown in Fig. 2.16, the electric field between the gate and channel lowers the graphene/SiO_2 and the graphene/vacuum barrier and enables two parallel paths for current

flow (Fig. 2.13(a)). As sketched in the band diagrams of Fig. 2.16(b), at lower biases, electrons can be injected in local trap energy levels of the SiO_2 forbidden bandgap, and move through SiO_2 in a sequence of trapping and de-trapping events. Traps are due to structural defects or stored charges. At higher biases, the additional Fowler-Nordheim tunneling in vacuum can take place (Fig. 2.16(c)) and become the dominating leakage mechanism, since electrons travel in vacuum from a graphene layer to the other without the capture and emission or any other scattering process limiting the current flow in the quasi-conduction band of SiO_2.

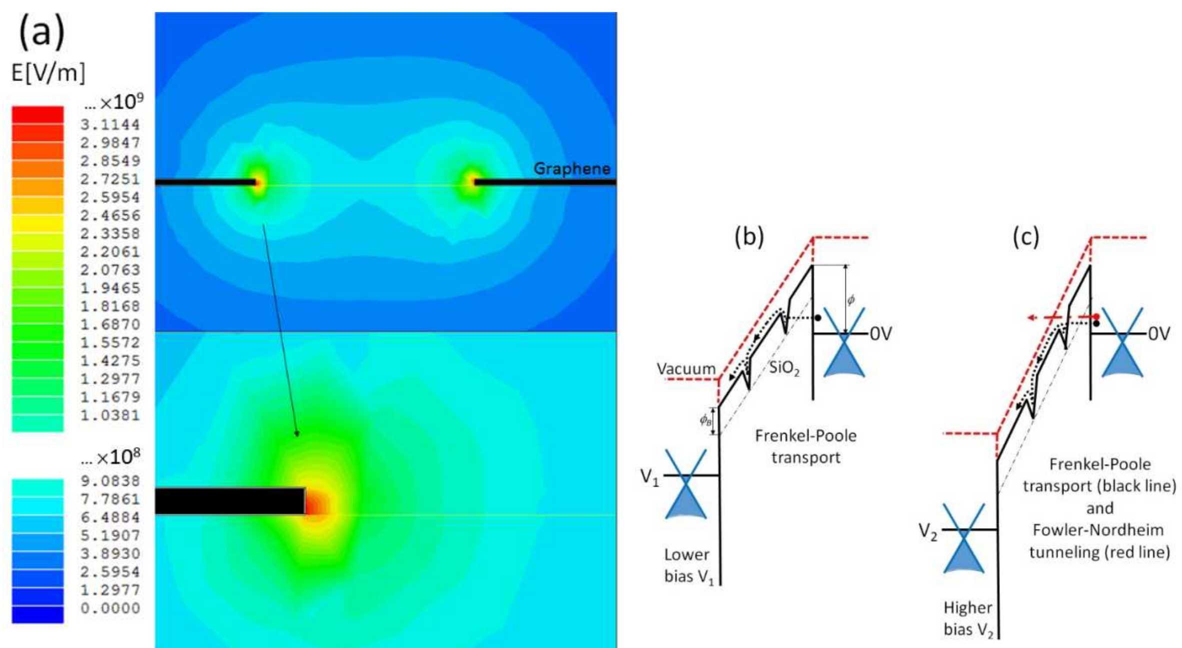

FIGURE 2.16: (a) Electric field between the graphene flakes forming channel and side-gate. A modest amplification factor ($\beta \sim 4$) is achieved at the graphene edge (the thickness of the graphene layers is set to 3 *nm* by software limitation). (b) Frenkel-Poole transport at lower bias (< 60 *V*). (c) Fowler-Nordheim tunneling and transport in vacuum, which dominates over Frenkel-Poole transport, at higher bias.

Considering the electric power dissipated at $V_{DG} > 70$ *V* and the area where tunneling occurs, a peak heat flux density around 80 kW/cm^2 can be estimated. This joule heating can cause desorption of remaining adsorbates (on graphene as well as on SiO_2 surface) and sublimation of carbon atoms, similarly to what has been reported for carbon nanotubes [122-123] and for graphene at high bias [124]. This modification results in enhanced spacing and suppression of the field emission, which makes the leakage current to return to the FP regime.

2.5 Conclusions

We characterized Ni- and Ti-contacted GFETs in order to analyze the channel conductance and the contact resistance due to the metal/graphene interface [22]. We measured the area specific contact resistivity and we demonstrated that, for untreated graphene, it is modulated by the back-gate voltage, showing the same dependence as the channel resistance. We also discussed distorted transfer characteristics presenting a double-dip feature in the positively gated region, systematically observed for long transistors. This feature is explained as corresponding to the two minima in the density of states of graphene, in the channel and under the metal respectively, which are different because of the metal doping induced by the metal-graphene interaction.

We studied the electric properties of graphene FETs with sputtered Nb contacts [30]. We clarified the role of adsorbates, PMMA residues and underlying SiO_2 on the channel doping and distinguished it from the doping at the contacts. We found that Nb acts as p-dopant but we clarified that graphene/Nb separation, controlled by stress or other factors, may turn Nb into a donor for graphene. We showed that the asymmetry observed in the transfer characteristics is naturally explained in terms of doping gradient from contact to channel which gives rise to a p-p^+-p structure in the p-branch and to a more resistive p-n-p structure in the n-branch. We discussed how Fermi level depinning at the contact can limit electron conductance and create a resistance plateau in the n-branch. We set a lower limit to the workfunction of Nb as $\Phi_{Nb} \geq 4.7eV$. We showed that Nb deposited with a low power sputtering forms contacts with graphene of resistivity ($\rho_c \approx 25\ k\Omega\mu m$) comparable to that achieved with evaporated metals such as Ti or Cr and about an order of magnitude higher than that typically achieved with Ni or Pd. We speculated that a non-negligible contribution to the contact resistance arises from strain. Our finding suggests that further reduction of the Nb/graphene contact resistance is achievable with a careful pre-deposition cleaning, a stress-free design of the metal leads as well as a more gentle deposition, such as that of electron beam evaporation. Further improvements, such as those needed for the search of new physics or new devices from the superconductor/graphene interface, can be envisaged by using contact resistance reducing techniques, such as O_2 or ozone treatment or pitting/cutting of graphene, which have been successful in reducing the ρ_c of metals as Ni and Pd below the limit of 100 $\Omega\mu m$. The effect of 10 keV electron irradiation, with dose of 30 e^-/nm^2, on the transport properties has been reported evidencing a significant reduction in carrier mobility and an increase in contact resistance. We showed that, for low energy irradiation, the pristine

conditions are almost restored after several electrical sweeps, which we explained as gradual removal of electrons piled up in the gate oxide during e-beam exposure [48].

We characterized side-gated all-graphene field effect transistors with gate-to-channel distance of 100 *nm* and channel width of 500 *nm* on SiO_2/Si substrates [69]. We showed that the side-gate is far more efficient than the back gate in modulating the channel conductance, with a 35% conductance swing over 0.5 *V*. We studied the current leakage along the SiO_2/vacuum gap between the channel and the side-gate, and found that a rapidly increasing current appears for $V_{DG} > 15$ *V*. We clarified that the leakage current is caused by Frenkel-Poole transport at the SiO_2 surface at lower biases and becomes dominated by electron field emission in vacuum at higher bias. This study clarifies aspects of the side-gate approach, which is recently becoming popular for graphene nanoribbon transistors with high on-off ratio. It further provides background for the development of easy-to-fabricate planar field-emission devices for vacuum nanoelectronics.

Bibliography

[1] Keyes R W 2005 *Rep. Progr. Phys.* **68** 2701-2746.

[2] Bourianoff G, Brillouet M, Cavin R K, Hiramoto T, Hutchby J A, Ionescu A M and Uchida K 2010 *Proc. IEEE* **98** 1986–92.

[3] Schwierz F 2010 *Nature Nanotechnology* **5** 487-96.

[4] Meric I, Dean CR, Young AF, Baklitskaya N, Tremblay NJ, Nuckolls C, Kim P and Shepard KL 2011 *Nano Lett.* **11**(3) 1093-7.

[5] Castro Neto A H, Guinea F, Peres N M R, Novoselov K S and Geim A K 2009 *Rev. Mod. Phys.* **81** 109 -162.

[6] Du X, Skachko I, Barker A and Andrei E Y 2008 *Nat. Nanotechnol.* **3** 491-495.

[7] Moser J, Barreiro A and Bachtold A 2007 *Appl. Phys. Lett.* **91** 163513.

[8] Stallinga P, Roy V A L, Xu Z-X, Xiang H-F and Che C-M 2008 *Adv. Mater.* **20** 2120–4.

[9] Nagashio K, Nishimura T, Kita K and Toriumi A 2010 *Jpn J. Appl. Phys.* **49** 051304.

[10] Nagashio K, Nishimura T, Kita K and Toriumi A 2010 *Appl. Phys. Lett.* **97** 143514.

[11] Khomyakov P A, Starikov A A, Brocks G and Kelly P J 2010 *Phys. Rev. B* **82** 115437.

[12] Nagashio K, Nishimura T, Kita K and Toriumi A 2009 *IEEE IEDM Tech. Dig.* **7-9** 565–68.

[13] Parrish KN and Akinwande D 2011 *Appl. Phys. Lett.* **98** 183505.

[14] Grosse KL, Bae MH, Lian F, Pop E and King WP 2011 *Nature Nanotechnology* **6** 287-290.

[15] Xia F, Perebeinos V, Lin YM, Wu Y and Avouris 2011 *Nature Nanotechnology* **6** 179-84.

[16] Russo S, Craciun MF, Yamamoto M, Morpurgo AF and Tarucha S 2010 *Physica E* **42** 677-79.

[17] Robinson JA, LaBella M, Zhu M, Hollander M, Kasarda R, Hughes Z, Trumbull K, Cavalero R and Snyder D 2011 *Appl. Phys. Lett.* **98** 053103.

[18] Di Bartolomeo A, Giubileo F, Santandrea S, Romeo F, Citro R, Schroeder T and Lupina G 2011 *Nanotechnology* **22** 275702.

[19] Giovannetti G, Khomyakov PA, Brocks G, Karpan VM, van den Brink J and Kelly PJ 2008 *Phys. Rev. Lett.* **101** 026803.

[20] Lohman T, von Klitzing K and Smet J H 2009 *Nano Lett.* **9** 1973–9.

[21] Joshi P, Romero H E, Neal A T, Toutam V K and Tadigataba S A 2010 *J. Phys.: Condens. Matter* **22** 334214.

[22] Di Bartolomeo A, Giubileo F, Iemmo L, Romeo F, Santandrea S and Gambardella U 2013 *J. Phys.: Condens. Matter* **25** 155303.

[23] Heersche H B, Jarillo-Herrero P, Oostinga J B, Vandersypen L M K and Morpurgo A F 2007 *Nature* **446** 56-59.

[24] Rickhaus P, Weiss M, Marot L and Schönenberger C 2012 *Nano Lett.* **12** 1942–1945.

[25] Komatsu K, Li C, Autier-Laurent S, Bouchiat H and Gueron S 2012 *Phys. Rev. B* **86** 115412.

[26] Mizuno N, Nielsen B and Du X 2013 *Nature Communications* **4** 2716.

[27] Liu W, Wei J, Sun X and Yu H 2013 *Crystals* **3** 257-274.

[28] Li W, Hacker C A, Cheng G, Liang Y, Tian B, Walker A R H, Richter C A, Gundlach D J, Liang X and Peng L 2014 *J. Appl. Phys.* **115** 114304.

[29] Zhong H, Zhang Z, Chen B, Xu H, Yu D, Huang L and Peng L 2015 *Nano Research* **8** 1669-1679.

[30] Di Bartolomeo A, Giubileo F, Romeo F, Sabatino P, Carapella G, Iemmo L, Schroeder T and Lupina G 2015 *Nanotechnology* **26** 475202.

[31] Buchowicz G, Stone P R, Robinson J T, Cress C D, Beeman J W and Dubon O D 2011 *Appl. Phys. Lett.* **98** 032102.

[32] Kalbac M, Lehtinen O, Krasheninnikov A V and Keinonen J 2013 *Adv. Mater.* **25** 1004–1009.

[33] Chen J H, Cullen W G, Jang C, Fuhrer M S and Williams E D 2009 *Phys. Rev. Lett.* **102** 236805.

[34] Compagnini G, Giannazzo F, Sonde S, Raineri V and Rimini E 2009 *Carbon* **47** 3201-3207.

[35] Guo B, Liu Q, Chen E, Zhu H, Fang L and Gong J R 2010 *Nano Lett.* **10** 4975-4980.

[36] Kotakoski J, Krasheninnikov A, Kaiser U and Meyer J 2011 *Phys. Rev. Lett.* **106** 105505.

[37] Teweldebrhan D and Balandin A A 2009 *Appl. Phys. Lett.* **95** 013101.

[38] Krasheninnikov A V and Banhart F 2007 *Nat. Mater.* **6** 723-733.

[39] Warner J H, Rummeli M H, Ge L, Gemming T, Montanari B, Harrison N M, Buchner B and Briggs G A D 2009 *Nat. Nanotechnol.* **5** 500-504.

[40] Xu M, Fujita D and Hanagata N 2010 *Nanotechnology* **21** 265705.

[41] Teweldebrhan D and Balandin A A 2009 *Appl. Phys. Lett.* **95** 246102.

[42] Murakami K, Kadowaki T and Fujita J 2013 *Appl. Phys. Lett.* **102** 043111.

[43] Jones J D, Mahajan K K, Williams W H, Ecton P A, Mo Y and Perez J M 2010 *Carbon* **48** 2335-2340.

[44] Jones J D, Ecton P A, Mo Y and Perez J M 2009 *Appl. Phys. Lett.* **95** 246101.

[45] Childres I, Jauregui L A, Foxe M, Tian J, Jalilian R, Jovanovic I and Chen Y P 2010 *Appl. Phys. Lett.* **97** 173109.

[46] He Y H, Wang L, Chen L, Wu Z F, Li W, Cai Y and Wang N 2011 *Appl. Phys. Lett.* **99** 033109.

[47] Yu X, Shen Y, Liu T, Wu T T and Wang Q J 2015 *Sci. Rep.* **5** 12014.

[48] Giubileo F, Di Bartolomeo A, Martucciello N, Romeo F, Iemmo L, Romano P and Passacantando M 2016 *Nanomaterials* **6** 206.

[49] Lemme MC, Echtermeyer TJ, Baus M and Kurz H. A 2007 *IEEE Electron Device Letters* **28** 282-284.

[50] Meric I, Han MY, Young AF, Ozyilmaz B, Kim P and Shepard KL 2008 *Nat. Nanotech.* **3** 654-659.

[51] Di Bartolomeo A 2016 *Phys. Rep.* **606** 1-58.

[52] Russo S, Craciun MF, Yamamoto M, Tarucha S and Morpurgo AF 2009 *New J. of Phys.* **11** 095018.

[53] Molitor F, Güttinger J, Stampfer C, Graf D, Ihn T and Ensslin K 2007 *Phys. Rev. B* **76** 245426.

[54] Li X, Wu X, Sprinkle M, Ming F, Ruan M, Hu Y, Berger C and deHeer WA 2010 *Phys. Stat. Sol. A* **207** 286-290.

[55] Hähnlein B, Händel B, Pezoldt J, Töpfer H, Granzner R and Schwierz F 2012 *Appl. Phys. Lett.* **101** 093504.

[56] Chen C-T, Low T, Chiu H-Y and Zhu W 2012 *IEEE Elec. Dev. Lett.* **33** 330–332.

[57] Tung L-T and Kan EC 2015 *J. Elec. Dev. Soc.* **3** 144-148.

[58] Tian JF, L. Jauregui LA, Lopez G, Cao H and Chen YP 2010 *Appl. Phys. Lett.* **96** 263110.

[59] Malesevic A, Kemps R, Vanhulsel A, Chowdhury MP, Volodin A and Van Haesendonck C 2008 *J. Appl. Phys.* **104** 084301.

[60] Eda G, Unalan HE, Rupesinghe N, Amaratunga JAJ and Chhowalla M 2008 *Appl. Phys. Lett.* **93** 233502.

[61] Lee SW, Lee SS and Yang E-H 2009 *Nanoscale Res. Lett.* **4** 1218–1221.

[62] Wu Z-S, Pei S, Ren W, Tang D, Gao L, Liu B, Li F, Liu C and Cheng H M 2009 *Adv. Mater.* **21** 1756–1760.

[63] Xiao Z, She J, Deng S, Tang Z, Li Z, Lu J and Xu N 2010 *ACS Nano* **4** 6332–6336.

[64] Santandrea S, Giubileo F, Grossi V, Santucci S, Passacantando M, Schroeder T, Lupina G and Di Bartolomeo A 2011 *Appl. Phys. Lett.* **98** 163109.

[65] Kleshch VI, Bandurin DA, Orekhov AS, Purcell ST and Obraztsov AN 2015 *Appl. Surf. Sci.* **357** 1967–1974.

[66] Wang HM, Zheng Z, Wang YY, Qiu JJ, Guo ZB, Shen ZX and Yu T 2010 *Appl. Phys. Lett.* **96** 023106.

[67] Fowler RH and Nordheim L 1928 *Proc. R. Soc. A* **19** 173-181.

[68] Kumar S, Duesberg GS, Pratap R and Raghavan S 2014 *Appl. Phys. Lett.* **105** 103107.

[69] Di Bartolomeo A, Giubileo F, Iemmo L, Romeo F, Russo S, Unal S, Passacantando M, Grossi V and Cucolo A M 2016 *Appl. Phys. Lett.* **109** 023510.

[70] Ferrari AC, Meyer J C, Scardaci V, Casiraghi C, Lazzeri M, Mauri F, Piscanec S, Jiang D, Novoselov K S, Roth S and Geim A K 2006 *Phys. Rev. Lett.* **97** 187401.

[71] Adam S, Hwang E H, Galitski V M and Das Sarma S 2007 *Proc. Natl. Acad. Sci.* **104** 18392–7.

[72] Huard B, Sulpizio J A, Stander N, Todd K, Yang B and Goldhaber-Gordon D 2007 *Phys. Rev. Lett.* **98** 236803.

[73] Lee E J H, Balasubramanian K, Weitz R T, BurghardM and Kern K 2008 *Nat. Nanotechnol.* **3** 486–90.

[74] Khomyakov P A, Giovannetti G, Rusu P C, Brocks G, van den Brink J and Kelly P J 2009 *Phys. Rev. B* **79** 195425.

[75] Schroeder DK 2006 *Semiconductor material and device characterization* John Wiley & Sons, Hoboken, NJ, p.138.

[76] Berdebes D, Low T, Sui Y, Appenzeller J and Lundstrom M *IEEE Transaction on Electron Devices* **11** 3925-32.

[77] Venugopal A, Colombo L and Vogel EM 2010 *Appl. Phys. Lett.* **96** 013512.

[78] De Marco P, Nardone N, Del Vitto A, Alessandri M, Santucci S and Ottaviano L 2010 *Nanotechnology* **21** 255703.

[79] Ferrari A C, Meyer J C, Scardaci V, Casiraghi C, Lazzeri M, Mauri F, Piscanec S, Jiang D, Novoselov K S, Roth S and Geim A K 2006 *Phys. Rev. Lett.* **97** 187401.

[80] Freund J, Halbritter J and Hörber J K 1999 *Microsc. Res. Tech.* **44** 327-38.

[81] Schedin F, Geim A K, Morozov S V, Hill E V, Blake P, Katsnelson M I and Novoselov K S 2007 *Nature materials* **6** 652-655.

[82] Ryu S, Liu L, Berciaud S, Yu Y J, Liu H, Kim P, Flynn G W and Brus L E 2010 *Nano Lett.* **10** 4944.

[83] Leenaerts O, Partoens B and Peeters F M 2008 *Phys. Rev. B* **77** 125416.

[84] Pirkle A, Chan J, Venugopal A, Hinojos D, Magnuson, McDonnell S, Colombo L, Vogel E M, Ruoff R S and Wallace R M 2011 *Appl. Phys. Lett.* **99** 122108.

[85] Suk J W, Lee W H, Lee J, Chou H, Piner R D, Hao Y, Akinwande D and Ruoff R S 2013 *Nano Lett.* **13** 1462-1467.

[86] Ni Z H, Wang H M, Luo Z Q, Wang Y Y, Yu T, Wu Y H and Shena Z H 2010 *J. Raman Spectrosc.* **41** 479-483.

[87] Romero H E, Shen N, Joshi P, Gutierrez H R, Tadigadapa S A, Sofo J O and Eklund P C 2008 *ACS Nano* **2** 2037-2044.

[88] Chen J H, Jang C, Adam S, Fuhrer M S, Williams E D and Ishigami M 2008 *Nature Physics* **4** 377-381.

[89] Cho S and Fuhrer M S 2008 *Phys. Rev. B* **77** 081402R.

[90] Adam S, Jung S, Klimov N N, Zhitenev N B, Stroscio J A and Stiles M D 2011 *Phys. Rev. B* **84** 235421.

[91] Wang H, Wu Y, Cong C, Shang J and Yu T 2010 *ACS Nano* **4** 7221–7228.

[92] Di Bartolomeo A, Rinzan M, Boyd A K, Yang Y, Guadagno L, Giubileo F and Barbara P 2010 *Nanotechnology* **21** 115204.

[93] Liu W J, Yu H Y, Xu S H, Zhang Q, Zou X, Wang J L, Pey K L, Wei J, Zhu H L and Li M F 2011 *IEEE Electron Device Letters* **32** 128-129.

[94] Huard B, Stander N, Sulpizio J A and Goldhaber-Gordon D 2008 *Phys Rev B* **78** 121402R.

[95] Kim S, Nah J, Jo I, Shahrjerdi D, Colombo L, Yao Z, Tutuc E and Banerjee S K 2009 *Appl. Phys. Lett.* **94** 062107.

[96] Lv H, Wu H, Liu J, Yu J, Niu J, Li J, Xu Q, Wu X and Qian H 2013 *Appl. Phys. Lett.* **103** 193102.

[97] Chen F, Xia J and Tao N 2009 *Nano Letters* **9** 1621-1625.

[98] Novikov D S 2007 *Appl. Phys. Lett.* **91** 2779107.

[99] Ni Z H, Yu T, Lu Y H, Wang Y Y, Feng Y P and Shen Z X 2008 *ACS Nano* **2** 2301-2305.

[100] Li Y, Jiang X, Liu Z and Liu Z 2010 *Nano Research* **3** 545-556.

[101] Teague M L, Lai A P, Velasco J, Hughes C R, Beyer A D, Bockrath M W, Lau C N and Yeh N C 2009 *Nano Lett.* **9** 2542-2546.

[102] Fu X-W, Liao Z-M, Zhou J-X, Zhou Y-B, Wu H-C, Zhang R, Jing J, Xu J, Wu X, Guo W and Yu D 2011 *Appl. Phys. Lett.* **99** 213107.

[103] Mueller T, Xia F, Freitag M, Tsang J and Avouris Ph 2009 *Phys. Rev. B* **79** 245430.

[104] Nouchi R and Tanigaki K 2010 *Appl. Phys. Lett.* **96** 253503.

[105] Haynes W M (ed), *CRC Handbook of Chemistry and Physics, 95th edition* 2014 CRC Press, ISBN 9781482208689.

[106] Leblanc R P, Vanbrugghe B C and Girouard F E 1974 *Canadian Journal of Physics* **52** 1589-1593.

[107] Kobyakov V P, Menabde N E, Sirenko A M, Tsekhladze D L and Tskhakaya V K 1987 *Poverkhnost': Fizika, Khimiya, Mekhanika* **2** 145-147.

[108] Pi K, McCreary K M, Bao W, Han W, Chiang Y F, Li Y, Tsai S-W, Lau C N and Kawakami R K 2009 *Phys. Rev. B* **80** 075406.

[109] Xu S and Zhang Q 2010 *IEEE 978-1-4244-5869.*

[110] Low T, Hong S, Appenzeller J, Datta S and Lundstrom M S 2009 *IEEE Trans Electron Devices* **56** 1292.

[111] Iqbal M Z, Singh A K, Iqbal M W, Seo S and Eom J 2012 *J. Appl. Phys.* **111** 084307.

[112] Wang X, Zhao M and Nolte DD 2009 *Appl. Phys. Lett.* **95** 081102.

[113] Craciun MF, Russo S, Yamamoto M, Oostinga JB, Morpurgo AF and Tarucha S 2009 *Nat. Nanotech.* **4** 383-388.

[114] Sze SM and Ng KK. *Physics of semiconductor devices*, Third edition 2007, John Wiley & Sons: Hoboken, New Jersey. 227-229.

[115] Knoch J, Chen Z and Appenzeller J 2012 *IEEE Trans. on Nanaotech.* **2** 513-519.

[116] Song SM and Cho BJ 2013 *Carbon Letters* **14** 162-170.

[117] Feng T, Xie D , Xu J, Zhao H, Li G, Ren T and Zhu H 2014 *Carbon* **79** 363-368.

[118] Nouchi R and Tanigaki K 2015 *Appl. Phys. Lett.* **106** 083107.

[119] Chiu F-C 2014 *Adv. Mat. Sci. Eng.* **2014** 578168.

[120] Forbes RG and Deane JHB 2007 *Proc. R. Soc. A* **463** 2907-2927.

[121] Edgcombe CJ and Valdrè U 2001 *J. Microsc.* **203** 188-194.

[122] Di Bartolomeo A, Scarfato A, Giubileo F, Bobba F, Biasiucci M, Cucolo AM, Santucci S and Passacantando M 2007 *Carbon* **45** 2957-2971.

[123] Passacantando M, Bussolotti F, Santucci S, Di Bartolomeo A, Giubileo F, Iemmo L, and Cucolo AM 2008 *Nanotechnology* **19** 395701.

[124] Barreiro A, Börrnert F, Rümmeli MH, Büchner B and Vandersypen LMK 2012 *Nano Lett.* **12** 1873−1878.

Chapter 3

Graphene/Si-nanotip Schottky diode

3.1 Introduction

Graphene/silicon (Gr/Si) heterojunctions are key elements of many graphene-based devices such as photodetectors [1-3], solar cells [4-6], chemical-biological sensors [7-9], and high frequency transistors [10-14]. Such heterostructures are gaining interest from the semiconductor industry also for the potentiality to replace ultra-shallow doped junctions in modern complementary-metal-oxide-semiconductor (CMOS) technologies.

The zero-bandgap and linear energy-momentum relationship of graphene, which result in finite density of states (DOS), have been shown to enable energy Fermi level tuning and hence Schottky barrier height control by a single anode-cathode bias [15]. Adding an electrostatic gate can further improve the barrier control in a three-terminal barristor (variable barrier device) [11].

In this chapter, we perform the electrical characterization of a new-concept of Gr/Si photodiode with graphene on nano-patterned Si surfaces and we demonstrate that this device is more performant than their large area, planar counterparts. In our approach, the coexistence on the same graphene layer of junction areas with much bigger graphene regions exposed to the field of the substrate, which acts as well-coupled back-gate especially near the tips, enables improved control of the Schottky barrier height by a single applied bias. This peculiarity makes the device an effective two-terminal barristor with linear control of the barrier height. More importantly, while preserving the barrier uniformity, the nano-textured surface enhances light collection due to multiple reflections and the tip-enhanced field favors photo-charge separation with internal gain due to impact ionization. These features result in record responsivity, which is one to two orders of magnitude higher than in planar Gr/Si junctions [1] and about one order of magnitude better than in commercial semiconductor photodetectors. This work [16] represents a significant advance in the realization and characterization of graphene/Si Schottky devices for optoelectronic applications.

3.2 Device fabrication and measurement setup

The device has been produced at IHP-Microelectronics in Frankfurt. Si-tip arrays (Fig. 3.1(a)) were prepared on degenerately doped (~ 10^{18} cm^{-3}) n-type Si wafers. Fabrication of the Si-tip array includes a SiO_2 or Si_3N_4 hardmask with photo-resist patterned by lithography, reactive ion etching (RIE) of Si, plasma-enhanced chemical vapor deposition (PECVD) of a thick SiO_2 layer completely covering the formed Si-tips, and a chemical-mechanical planarization step to reduce the SiO_2 thickness till revealing circular Si-tips surface of given diameter. Further details on the fabrication process can be found elsewhere [17]. Just before the graphene transfer, the Si-tip substrates were dipped in a 0.5% hydrofluoric acid solution for 10 seconds to remove only the native SiO_2 on Si-tips [18-19] and enable formation of clean Gr/Si junctions. Graphene was transferred from commercially available Cu foils using a wet transfer process [20]. Immersion in deionized water and subsequent dry process by nitrogen-gas blowing helped in H-passivating the surface dangling bonds.

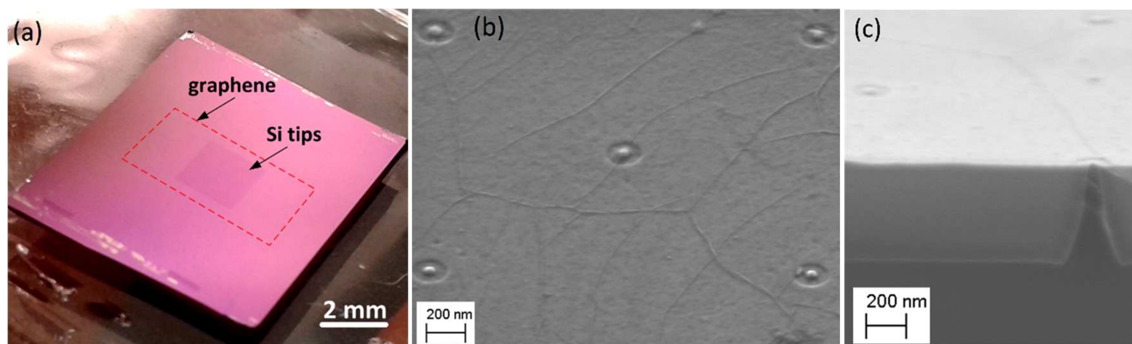

FIGURE 3.1: (a) Photograph of a single chip with a 2.5×2.5 mm^2 Si-tip array covered by a monolayer graphene transferred from Cu. (b) SEM top view of the tips emerging from the SiO_2 insulating layer and covered by graphene. The diameter of the emerging tips is ~ 50 *nm*. Graphene wrinkles characteristic of graphene transferred from Cu are visible. (c) SEM cross-section image showing one of the Si-tips embedded in SiO_2 and covered by graphene. The tip pitch size is 1.41 μm and the tip height is ~ 0.5 μm.

Fig. 3.1(b) shows a scanning electron microscopy (SEM) image taken after graphene transfer: Five Si-tips with a diameter of about 50 *nm* are seen underneath the graphene layer and wrinkles, characteristic of CVD graphene grown on Cu, can be clearly identified. Fig. 3.1(c) shows a SEM cross-section of one of the Si-tips with graphene.

To evaluate the quality of graphene, Raman spectroscopy measurements with a 514 *nm* laser source (spot size ~ 600 *nm*) were performed. Fig. 3.2(a) shows a representative spectrum taken from the area between the Si-tips. Beside the characteristic 2D and G bands, a typical

feature of monolayer graphene, a very small D peak related to defects is seen at about 1350 cm^{-1}. As shown by peak intensity mapping measurements presented in Fig. 3.2(b), the intensity of the D peak does not correlate with the positions of the Si-tips. The observed local increase in the D band intensity is most probably related to the presence of multilayer graphene islands [21]. Similarly, no particular correlation between the 2D/G peak intensity ratio and the positions of the Si-tips was revealed (Fig. 3.2(c)). Another small peak appears at 2450 cm^{-1}, generally indicated as D+D", and interpreted as a combination of D and D" phonons, the latter belonging to the in-plane longitudinal acoustic branch [22].

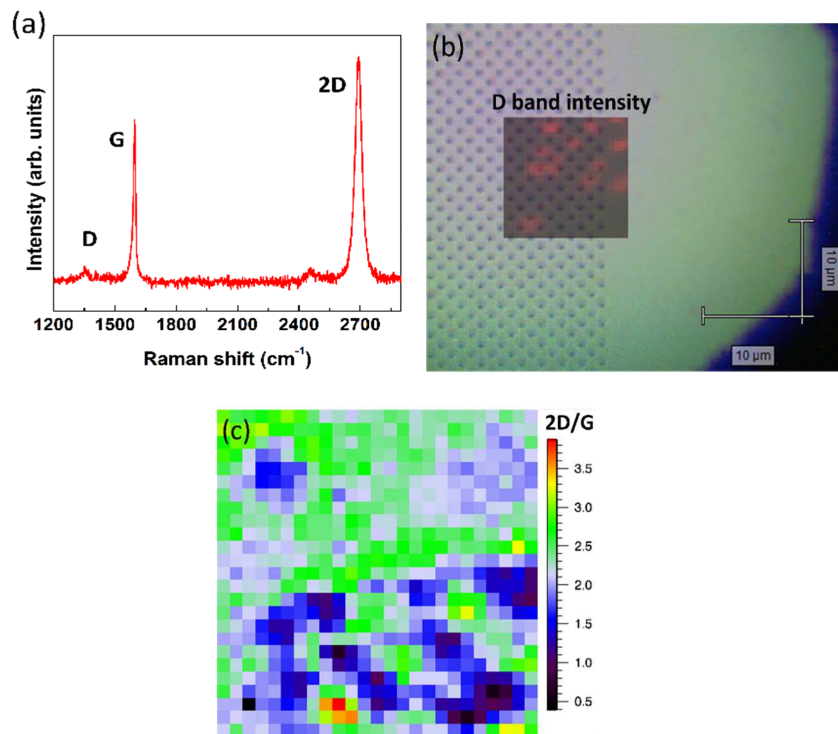

FIGURE 3.2: (a) Representative µRaman spectrum taken after graphene transfer. (b) D band intensity distribution extracted from Raman mapping measurement on an area of 12×12 μm^2 overlaid on optical image. (c) 2D/G intensity map taken from the same 12×12 μm^2 area indicated in (b).

Sheet resistance of the graphene layer measured using 4-point technique beyond the Si-tip array was ~ 0.9 $k\Omega/$, a value in the range typically reported for CVD graphene on Cu [23].

The setup used for electrical measurements of the Gr/Si heterojunction is illustrated in Fig. 3.3(a). The top graphene layer was contacted with evaporated Au, while ohmic contact with the scratched bottom Si substrate was made with Ag paste. Electrical measurements were performed in a Janis probe station with pressure and temperature control. The top-injection configuration was adopted, with the biasing lead on graphene and the Ag electrode grounded. The measurements were carried out at atmospheric pressure.

3.3 Results and discussion

3.3.1 Schottky barrier

The dark *I-V* characteristics of the Gr/Si-tip heterojunction in the temperature range 120-390 *K* are shown in Fig. 3.3(b). The device exhibits a rectifying behavior with the forward current at positive bias, as expected for p-type graphene on n-Si. The p-type doping is usually observed in air-exposed graphene [10,24]. The current for a given voltage increases with rising temperature, which is typical of thermionic emission in this kind of devices. At modest positive bias, the room and higher temperature forward *I-V* curves show an almost ideal diode behavior. At lower temperatures, namely $T < 250$ *K*, a new feature appears in the lower bias part of the forward *I-V* curves, where the current is dominated by a leakage component that adds non-linearity to the semi-log *I-V* plot. This leakage component is usually attributed to generation and recombination of carriers in the charge space region, field emission and thermionic field emission or surface/edge effects that may lead to local barrier lowering [25-26]. Such component becomes relevant when the low-temperature suppresses the thermionic emission, e.g. at $T = 121$ *K*, where it manifests on the interval $0 < V < 0.25$ *V*.

To gain insight into carrier transport across the Gr/Si-tip device, we focus on the *I-V* curve at $T = 300$ *K*. Fig. 3.3(c) shows the measured data together with the best fitting curve as predicted by the Schottky model [27-29], which is described by the following *I-V* relation:

$$I = I_0\left[e^{q(V-R_sI)/nkT} - 1\right], \tag{3.1}$$

with:

$$I_0 = AA^*T^2e^{-\Phi_B/kT}, \tag{3.2}$$

where I_0 is the reverse saturation current, A the contact area, $A^* = 4\pi qm^*k^2/h^3$ the effective Richardson constant with m^* the electron effective mass, T the absolute temperature, Φ_B the Schottky barrier height, k the Boltzmann constant, q the electronic charge, n the ideality factor that takes into accounts deviations from the pure thermionic regime, and R_s the series resistance. More specifically, R_s is the lump sum of bulk Si, graphene, metal leads and contact resistances, and is dominated by graphene. The equivalent circuit, consisting of the series of a diode with ideality factor n and a resistor R_s, is shown in the inset of Fig. 3.3(c).

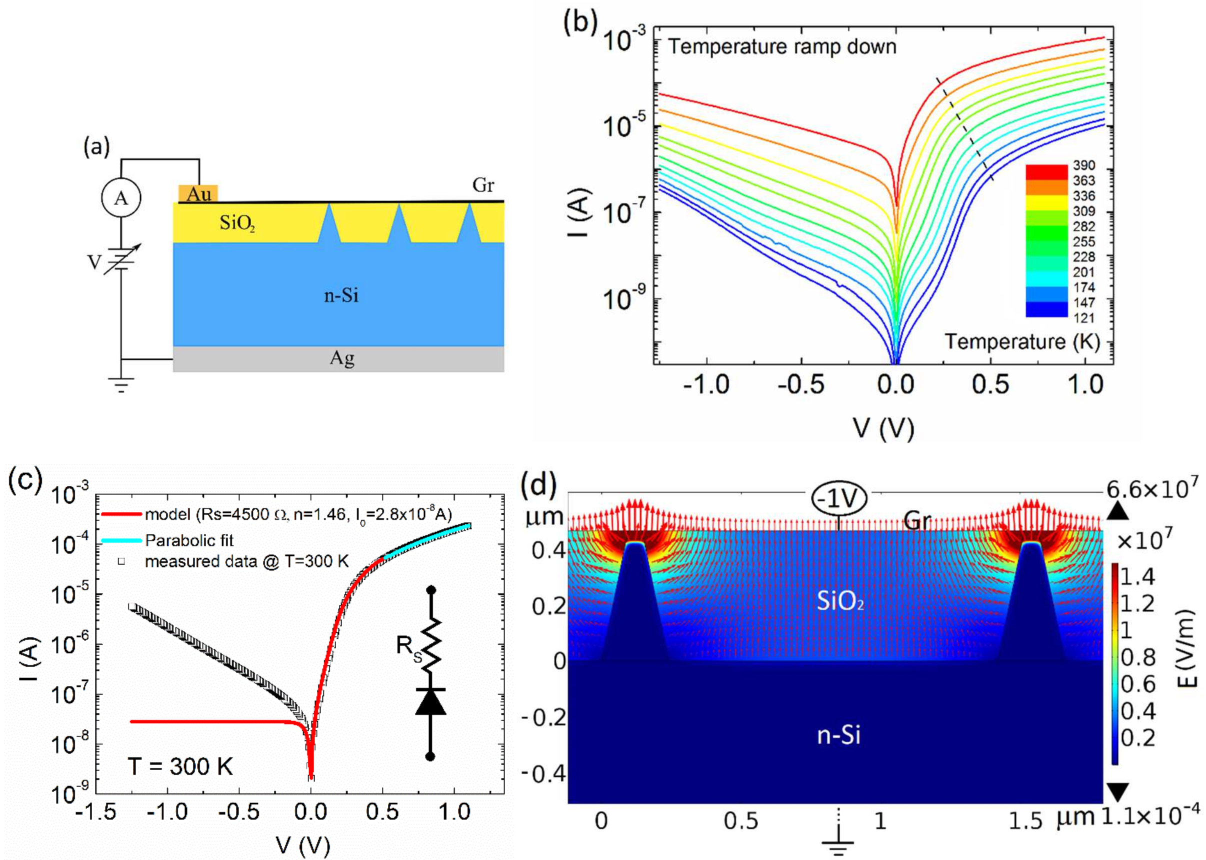

FIGURE 3.3: (a) Layout and measurement setup of the Gr/nSi-tip device. (b) I-V characteristics in the temperature range 120 - 390 K and in steps of ~ 30 K measured in dark and at atmospheric pressure. (c) *I-V* curve measured at T = 300 K (black squares) and fit of the Schottky diode model of eq. (3.1) (red line). In flat-band condition, that is for $V > 0.5\ V$, the *I-V* curve is better described by a SCLC model, $I \sim V^2$ (cyan line). The inset shows the equivalent circuit consisting of a diode with ideality factor n and a series resistance Rs. (d) Numerical simulation (by COMSOL software) of the electric field in the region between two Si-tips for the device under reverse bias (-1V), showing field amplification (cyan to reddish color) near the tip edge, where the gating effect of the substrate is more effective. Field arrows (red) are shown in logarithmic scale. In the simulation, graphene is considered as a metal contact with 4.6 eV workfunction and at -1V bias with respect to the bottom n-Si substrate, which is grounded; the Gr/Si-tip junctions are assumed as Schottky junctions with Schottky barrier height of 0.36 eV.

As seen in Fig. 3.3(c), eq. (3.1) provides a perfect fit in the range $0 < V < 0.5\ V$; at higher bias, the Gr/Si-tip diode enters a high injection regime, where the voltage drop across the series resistance strongly limits the exponential increase of the current, until the barrier reaches the flat-band condition and the *I-V* characteristic is dominated by the series resistance. In this region, henceforth referred as flat-band, the current is better described by a quadratic relation, $I \sim V^2$, typical of space charge limited conduction (SCLC). The gating effect of the substrate increases the p-doping of graphene when $V > 0\ V$ and this is the origin of the quadratic dependence. Indeed, in flat-band condition, $V \approx R_sI$, and the graphene-dominated R_s is

proportional to the inverse bias ($R_s \sim (qn_q)^{-1} \sim (CV)^{-1}$) (where n_q is the graphene carrier density and C the gate capacitance per unit area), which makes the current to scale as V^2. The gating effect of the substrate is particularly effective around the tips, where the electric field is stronger, as shown in Fig. 3.3(d).

Fig. 3.3(c) also evidences that, in reverse bias ($V < 0$ V), the current dramatically deviates from the constant behavior predicted by eq. (3.1), implying that it is not the usual saturation current of a diode. Since lnI increases linearly with $|V|$, the common modeling by a simple shunt resistance seems not appropriate in this case. A better explanation is provided by a bias dependence of the Schottky barrier, due to a combination of image force lowering and low density of states of graphene in the absence of Fermi level pinning, as we will discuss in the following.

Fig. 3.4 shows the rectification factor r, the series resistance R_s and the ideality factor n over the explored temperature range. The rectification factor r is here defined as the ratio of the on/off current at $V = \pm V_{FB}$, $I(V_{FB})/I(-V_{FB})$, where V_{FB} is the voltage corresponding to the onset of the flat-band region (that is the region to the right of the dashed-black line in Fig. 3.3(b). Both r and V_{FB} decrease with increasing temperature. In particular, r, which is ~120 at room temperature, has a monotonic behavior with two possible regimes crossing at $T \sim 260$ K. Below this temperature, there is a reduced rate dr/dT, likely correlated with the deviation from the pure thermionic emission. V_{FB} linearly decreases with temperature with a slope $|dV_{FB}/dT| \approx 1$ mV/K, a behavior similar to the forward voltage drop of a typical pn-diode. As the temperature increases, the flat-band condition, $V \approx R_sI$, is reached at lower bias due to the strong $I(T)$ dependence, as described by eq. (3.2). Indeed, the linear behavior of V_{FB} implies a strongly decreasing $R_s(T)$ to counterbalance the exponential growth of $I(T)$ with temperature.

We used I-V data below and around V_{FB}, and followed the Cheung method [30-31] to extract R_s and n at a given temperature from the slope and the intercept of the corresponding $dV/d(lnI)$ vs. I plot, since:

$$\frac{dV}{d(lnI)} = \frac{nkT}{q} + R_sI. \tag{3.3}$$

R_s and n were also obtained from $(dI/dV)/I$ vs. dI/dV plots (Werner method [32]), considering that:

$$\frac{dI/dV}{I} = \frac{q}{nkT}\left[1 - R_s\left(\frac{dI}{dV}\right)\right]. \tag{3.4}$$

Both eqs. (3.3) and (3.4) are valid in the limit of $V \geq 3nkT/q$. The consistent results are shown in Fig. 3.4(b) and 3.4(c). Remarkably, R_s exhibits the expected exponential decrease with T ($R_s \sim exp(-\alpha T)$), that is a semiconductor behavior with negative temperature coefficient of resistance, dR_s/dT. Neither Si [33,34] nor metals or ohmic contacts [35] can account for the negative dR_s/dT in the temperature range under investigation. The semiconductor behavior can only originate from graphene. Indeed, the resistivity of graphene, especially at the lower carrier density close to the Dirac point and in the presence of defects or impurities, has been reported to decrease with rising temperature on exfoliated or CVD monolayer graphene, both suspended [36] or deposited on substrate [37-39]. A semiconductor behavior has been reported also for bilayer and few layer graphene on substrate over a wide temperature range [40-42]. The negative temperature coefficient in graphene is the result of competing mechanisms, with the thermally activated transport through inhomogeneous electron-hole puddles as the main recognized cause [39]. CVD graphene is more vulnerable to impurities or charged defects during the transfer process, and is particularly prone to develop electron-holes puddles that tend to produce a negative dR_s/dT.

The ideality factor was further estimated from the slope of straight-line fitting the thermionic part of the $ln(I)$ vs. V plot (i.e. the part between 0 and ~ V_{FB}, after excluding the leaky portion at lower biases), which according to eq. (3.1) and for leaky V » R_sI is described by:

$$lnI = lnI_0 + \frac{q}{nkT}V. \tag{3.5}$$

While the temperature dependence of n is the same (Fig. 3.4(c)), eq. (3.5) provides values which are 10% to 20% higher than those obtained with Cheung and Werner methods. The slope of a fitting straight line is usually more accurate than the intercept for the estimation of diode parameters, so the method based on eq. (3.5) is considered more reliable. n decreases with increasing temperature ($n = c + T_0/T$, with c and T_0 constants, as shown in the inset of Fig. 3.4(c)) and approaches the ideal value of 1 at the highest temperatures. This behavior confirms that the thermionic emission is the dominant carrier conduction process at high temperatures. On the contrary, at lower temperatures, the growing n indicates that other transport phenomena, as generation-recombination in the space charge region or thermionic field emission, add to thermionic emission. Furthermore, the observed temperature dependence of the ideality factor is a signature of Schottky barrier spatial inhomogeneity and of deformation of the barrier when a bias voltage is applied [43].

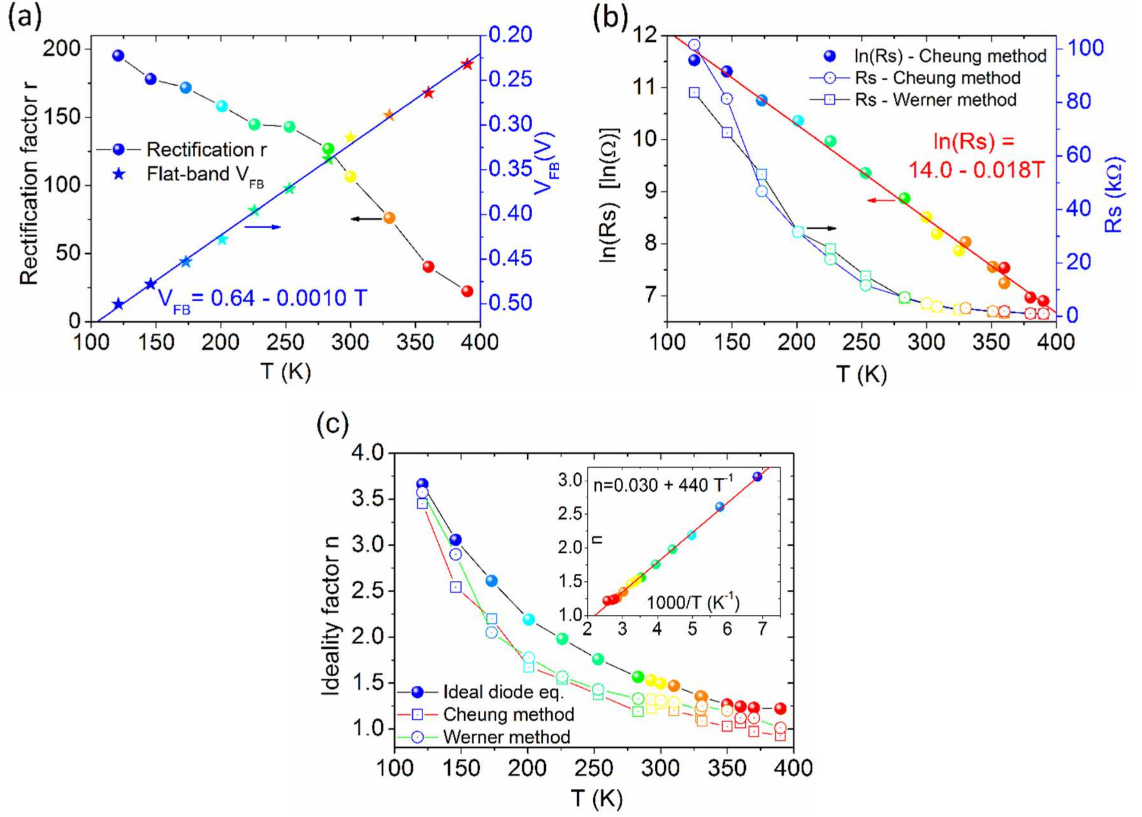

FIGURE 3.4: (a) Rectification factor r and flat-band voltage V_{FB} (in reverse scale) as a function of temperature T. The ideality factor is defined as $r = I(V_{FB})/I(-V_{FB})$, where V_{FB} is the voltage corresponding to the flat-band condition. (b) Series resistance R_s (right scale) and lnR_s (left scale) as a function of the temperature T, obtained from Cheung and Werner methods. (c) Comparison of the temperature dependence of the diode ideality factor n extracted from eq. (3.1) (full circles), Cheung (empty squares) and Werner (empty circles) methods. The inset shows the linear dependence of n on T^{-1}.

According to eq. (3.2), a plot of $ln(I_0/T^2)$ vs. $1/T$ (Richardson plot) is a straight line, whose slope and intercept are used to evaluate the Schottky barrier height Φ_B and $ln(AA^*)$ at a given bias:

$$ln\left(\frac{I_0}{T^2}\right) = ln(AA^*) - \frac{\Phi_B}{k}\frac{1}{T}. \quad (3.6)$$

In reverse bias, when $e^{q(V-R_sI)/nkT} \ll 1$, $I_0(T)$ is directly measured on the curves of Fig. 3.3(b). At zero bias, I_0 is extrapolated to $V = 0$ V as the intercept of the straight line fitting the thermionic part of the forward I-V characteristics. In forward bias, when $e^{qV/nkT} \gg 1$ and $V \gg R_sI$, eqs. (3.1) and (3.2) combine to yield a slightly modified Richardson equation, that requires n to estimate the Schottky barrier height:

$$ln\left(\frac{I}{T^2}\right) = ln(AA^*) - \frac{(\Phi_B - qV\ /\ n)}{k}\frac{1}{T}. \quad (3.7)$$

Examples of Richardson plots for a subset of applied biases are shown in Fig. 3.5(a), while a more complete set of measured $\Phi_B(V)$ is summarized in Fig. 3.5(b). Remarkably, $\Phi_B(V)$ exhibits a linear increase with V, and has the value $\Phi_B(V) \approx 0.36$ eV at zero bias. Fig. 3.5(b) depicts $ln(AA^*)$ with a very weak dependence on V. Considering the average value $ln(AA^*) \approx -16$ and an effective junction area of 6.079×10^{-5} cm^2 (estimated from the number of tips and conservatively assuming a circular junction area with mean radius of 25 nm and no micro-areas with missing graphene), the Richardson constant results $A^* = 0.002$ $A/(K^2cm^2)$, a value significantly lower than the theoretical 112 $A/(K^2cm^2)$ for electrons in Si. Similar low values, ranging from 10^{-3} to $10^{-1} A/(K^2cm^2)$ have been reported for Gr/Si planar heterojunction [44-46] and revised Schottky diode equations, based on Landauer formalism [45] or including the massless Dirac fermion nature of carriers in graphene [47-48], have been proposed to explain this anomaly.

The low value of A^*, the temperature dependence of n, the linear bias dependence of Φ_B as well as the deviation from linearity of the Richardson plot at low temperatures, can be ascribed to spatial inhomogeneities in the Schottky barrier height [43], as already mentioned. Since the Gr/Si-tip device under study is made of more than 3×10^6 nanojunctions, minimal tip-to-tip variation could result in significant barrier height fluctuations. Hills and valleys in the barrier height distribution can be caused e.g. by local effective barrier lowering due to field emission from tips with narrower radius of curvature, by inadvertent interfacial layers, by electron-hole puddles in graphene, or by surface defects or contaminates, possibly introduced during the fabrication process. An applied bias deforms the lower and higher barrier patches, causing $\Phi_B(V)$ dependence [43]. Indeed, a major disadvantage of the tip approach could be the limited shape control. Rather than a simple Si(001) plateau facet region, a tip could be a multi-facetted round shape Si structure. Different Si facets might have different work function values and further contribute to Schottky barrier inhomogeneities. Hence, to check the Schottky barrier spatial distribution, we calculated $\Phi_B(V)$ using eq. (3.2) with the extrapolated values of $I_0(T)$ at zero bias, and studied its temperature dependence (Fig. 3.5(c)).

The decreasing barrier height with lowering temperature is easily understood considering that the current becomes gradually dominated by electrons able to surmount the lower barrier patches, and this gives a reduced apparent barrier height. Assuming a Gaussian spatial distribution for Φ_B, with mean Φ_{Bm} and the standard deviation σ_B, the temperature dependence of the measured (apparent) barrier height Φ_B at zero applied bias is expected to follow the relation [43]:

$$\Phi_B = \Phi_{Bm} - \frac{q\sigma_B^2}{2kT}\,. \tag{3.8}$$

The standard deviation σ_B is a measure of the inhomogeneity of the Schottky barrier height (the lower σ_B the more uniform is Φ_B), and, according to eq. (3.8), can be extracted from the plot of Φ_B vs. 1/2kT, as shown in the inset of Fig. 3.5(c).

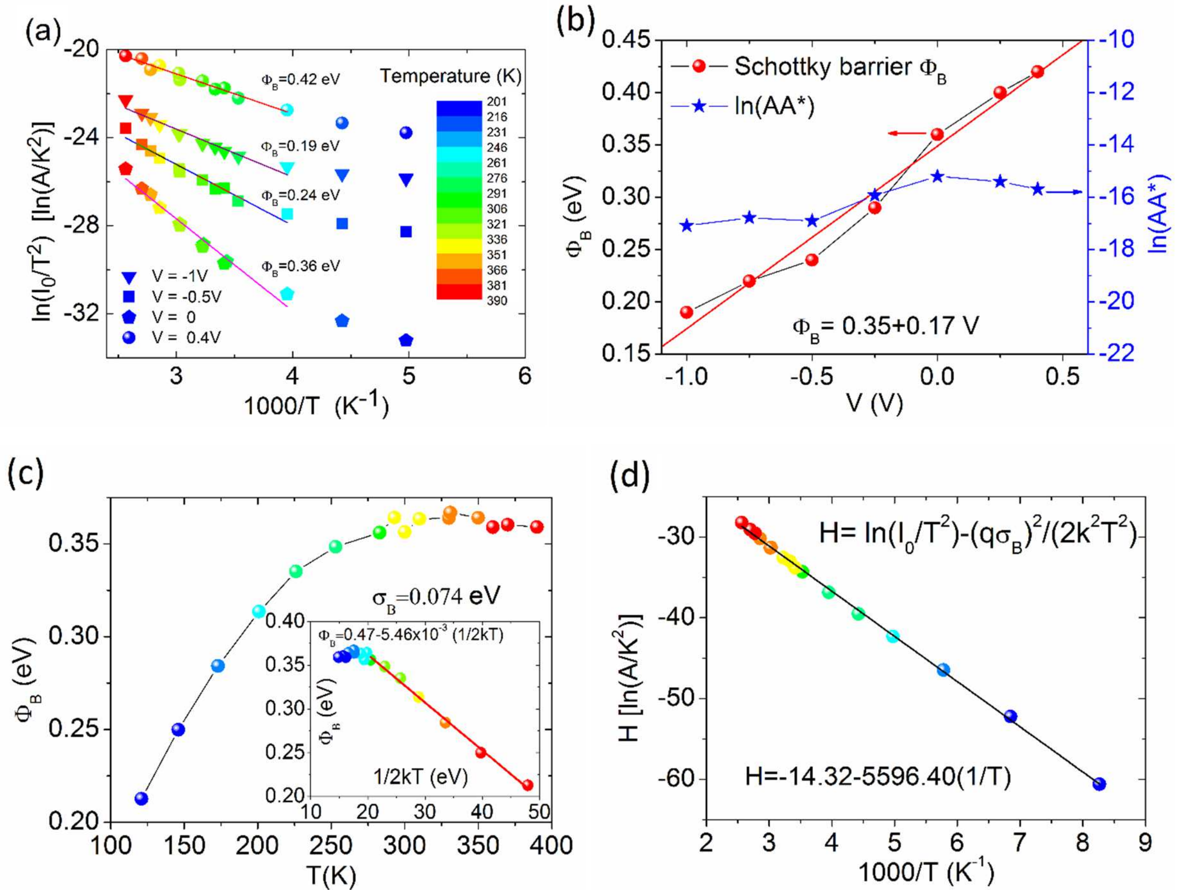

FIGURE 3.5: (a) Plot of $ln(I_0/T^2)$ vs. 1000/T (Richardson plot) with linear fit to extract the Schottky barrier height Φ_B at different bias V. Richardson plots show non-linearity at low temperature due to Schottky barrier inhomogeneities and deviation from the pure thermionic emission theory; accordingly, to estimate Φ_B, the two lowest temperature points were excluded from the fit. (b) Dependence of Schottky barrier height Φ_B and $ln(AA^*)$ on V. (c) Φ_B at zero bias as a function of temperature; the inset shows the fit of eq. (3.8) from which a value of the Schottky barrier inhomogeneity $\sigma_B \approx 74$ meV is obtained. (d) Modified Richardson plot according to the Gaussian distribution of the Schottky barrier height (eq. (3.9)).

As already mentioned, the Schottky barrier distribution can be deformed by the applied bias. In particular, Werner et al. [43] have demonstrated that a linear $\Phi_B(V)$ implies a voltage independent ideality factor and that a linear n vs. $1/T$ results from the narrowing of the Gaussian barrier distribution (i.e. of σ_B) with forward bias, meaning that the application of a

forward bias homogenizes the barrier fluctuations. The value of $\sigma_B \sim 74\ meV$ at zero bias is in agreement or below what has been reported for planar Gr/semiconductor heterojunctions [44,46,49]. This lead to the remarkable result that the tip-geometry and the transfer process do not introduce extra-inhomogeneity. However, we point out that the measured σ_B, despite its low value, is still enough to affect the low temperature part of the *I-V* characteristics and the Richardson plots.

As consistency check, we notice that $\Phi_{Bm} = 0.47\ eV$ extracted from eq. (3.8) is within 1.5 σ_B from the apparent Φ_B at high temperature estimated using eq. (3.2). Together, eqs. (3.2) and (3.8), give:

$$H \equiv ln\left(\frac{I_0}{T^2}\right) - \frac{q^2\sigma_B^2}{2k^2T^2} = ln(AA^*) - \frac{q\Phi_{Bm}}{kT}, \tag{3.9}$$

which suggests a modified Richardson plot of H vs. $1000/T$ (Fig. 3.5(d)) from which a more accurate and higher value of $A^* = 0.015\ A/(K^2cm^2)$ can be estimated, while $\Phi_{Bm} = 0.48\ eV$ remains practically unaffected. We remark here that A^* is possibly underestimated, given our conservative assumption of constant full-contact area between Gr and Si-tips; we also underline that Φ_{Bm} is consistent with other reported evaluations [11,50-51] and, as we discuss in the following, matches the prediction of Schottky-Mott theory.

The Schottky barrier height depends on the graphene work function, the Si electron affinity as well as on the interface states density and on the thickness of an inadvertent interfacial layer of atomic dimension, often due to native oxide, that is transparent to electrons but able to withstand a potential drop [27,29,52]:

$$\Phi_B = \Phi_{Gr} - X_{Si} - q\Delta, \tag{3.10}$$

where $\Phi_{Gr} = 4.5 \div 4.6\ eV$ is the work function of graphene [53-54], $X_{Si} = 4.05\ eV$ is the electron affinity of Si and Δ is the potential drop across the interfacial layer. High density of interface states at a given energy in the Si bandgap usually leads to pinning of the Fermi level and can result in a significant discrepancy from eq. (3.10). However, due to negligible interaction with chemically inert graphene, the formation of interface states is suppressed in graphene-semiconductor junctions if the Si-surface is defects-free and with saturated dangling bonds [55]. An ideal, trap free interface would result in unpinned Fermi level and yield a Schottky barrier height:

$$\Phi_B = \Phi_{Gr} - X_{Si}, \tag{3.11}$$

(Schottky-Mott relation) in the range 0.45÷0.55 eV for undoped graphene. The Fermi level unpinning enables easy modulation of the Schottky barrier, a feature that can be exploited to tune Gr/Si devices to match specific performance requests [11,56]. Deviations from the Schottky-Mott prediction are mainly due to image force lowering [57] or hot electrons barrier lowering [58-59]. Neglecting the field enhancement by the tip (values of the field up to 10^7 V/cm can be achieved, as shown in Fig. 3.3(d)), the maximum built-in electric field at the Gr/Si junction [29], is:

$$E_m = \sqrt{(2qN|\phi_i\,|)/\varepsilon_{Si}} \approx 3 \times 10^5\ V/cm, \tag{3.12}$$

(N = 10^{18} cm^{-3} is the Si doping density, $\phi_i \approx 0.3$ V is the built-in potential and $\varepsilon_{Si} = 12\varepsilon_0$ is the dielectric constant of Si) which corresponds to a Schottky barrier lowering by image force:

$$\Delta\Phi_B^I = q\sqrt{qE_m/(4\pi\varepsilon_{Si})} = q\sqrt[4]{q^3N|\phi_i|/\left(8\pi^2\varepsilon_{Si}^3\right)} \approx 0.06\ eV. \tag{3.13}$$

When a bias is applied to the junction, $|\phi_i\,|$ is replaced by $|\phi_i - V/m|$ in eqs. (3.12) and (3.13) (m is an ideality factor, see the following), and $\Delta\Phi^I_B$ is increased (decreased) by a reverse (forward) bias, as depicted in Fig. 3.6(a). At zero bias, adding $\Delta\Phi^I_B$ from eq. (3.13) to the measured $\Phi_B \approx 0.36$ eV brings the Schottky barrier height close to the ideal Schottky-Mott value. This result confirms the good quality of the Gr/Si-tip interfaces in the device under study.

A good quality interface also excludes the chance of Fermi level pinning. In graphene, the Fermi energy, E_F, at room temperature, is approximately related to the free carrier density n_q by a quadratic relation:

$$n_q \approx n_{q0} + E_F^2/(\pi\hbar^2 v_F^2), \tag{3.14}$$

(n_{q0} is the intrinsic carrier density and $v_F \approx 10^6$ m/s is the Fermi velocity of graphene). Eq. (3.14) enables fine tuning of E_F via n_q, which can be easily controlled by an electric field (electrostatic doping). In heterojunctions with unpinned Fermi level, E_F modifies the graphene work function and hence the Schottky barrier height. p-doping of graphene increases Φ_B and n-doping decreases it, as displayed in Fig. 3.6(a) for graphene on n-type Si. The electrostatic Schottky barrier variation, $\Delta\Phi^E_B = -E_F$, adds to the image force barrier lowering $\Delta\Phi^I_B$, to set Φ_B (Fig. 3.6(a)). Noteworthy, in the device under study, E_F modulation by electrostatic doping is achieved via the electric field (Fig. 3.3(d)) generated by the same voltage used to bias the junction.

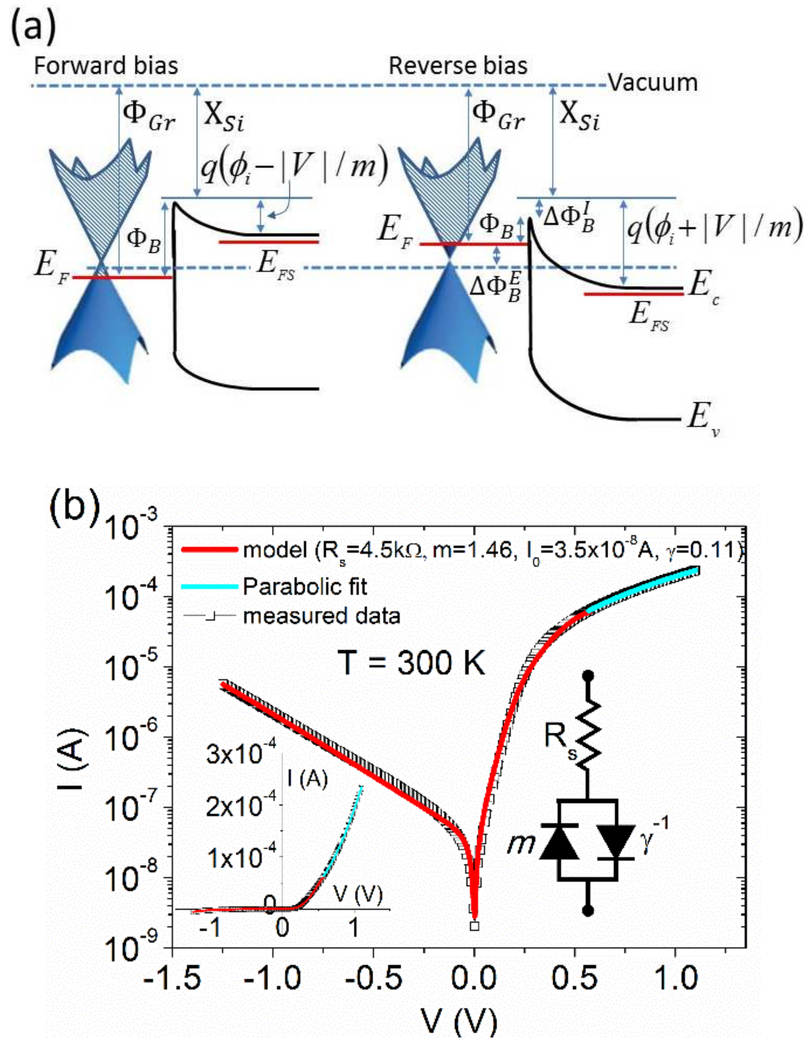

FIGURE 3.6: (a) Band diagrams of the Gr/Si-tip junction in forward and reverse bias. X_{Si}, Φ_{Gr} and E_F designate the Si electron affinity, the graphene work function and Fermi level, respectively; E_C/E_V are the bottom/top of the conduction/valence band and E_{FS} the Fermi level of Si (the dashed blue line represents the Fermi level at zero-bias, with an assumed graphene low p-doping). ϕ_i is the built-in potential and V the applied bias. In forward (reverse) bias the change of the graphene Fermi level leads to an increase (decrease) of the Schottky barrier height ($\Delta\Phi^E_B = - E_F$). The graphene Fermi level shift, which is required to allocate more and more charge to mirror the bias-dependent immobile charge of the semiconductor depletion layer, is due to the low DOS of graphene around the Dirac point. Also shown is the variation of Schottky barrier height, $\Delta\Phi^I_B$, caused by image force. (b) Fitting of eq. (3.19) to the *I-V* data measured at T=300 *K*. The left inset displays the *I-V* data in linear scale. The right inset shows the equivalent circuit, consisting of two opposite diodes with ideal factors m and γ^{-1} respectively, in parallel to each other and in series with the resistance R_s (we notice that the value of γ here is slightly lower that the one obtained in Fig. 3.5(b), where we did not take into account the effect of R_sI).

Both $\Delta\Phi^I_B$ and $\Delta\Phi^E_B$ introduce a sublinear dependence on the applied bias V in the Schottky barrier height (roughly as the $\sqrt[4]{|V|}$ from eq. (3.13) and $\sqrt{|V|}$ from eq. (3.14), respectively, since $|\Delta\Phi_B^E| = |E_F| \sim \sqrt{qn} \sim \sqrt{V}$), which can be written as:

$$\Phi_B(V) = \Phi_{B0} + \Delta\Phi_B(V). \tag{3.15}$$

$\Delta\Phi_B(V)$ is positive in forward bias and negative in reverse bias.

The effect of electrostatic doping, $\Delta\Phi^E{}_B$ was first included in the diode eqs. (3.1) and (3.2) by Tongay et al. [15] who obtained a reverse saturation current I_0 depending on the exponential of $\sqrt{|V|}$. A similar behavior was proposed with different approaches also by Sinha et al. [45] and Liang et al. [47-48]. However, for the Gr/Si-tip device under study, the measured barrier height of Fig. 3.5(b) shows that $\Phi_B(V)$ is better described by a linear relation. Accordingly, we write:

$$\Delta\Phi_B(V) = \gamma\, q(V - R_s I), \tag{3.16}$$

with γ a dimensionless constant, and the reverse saturation current as:

$$\overline{I}_0 = AA^*T^2 e^{-[\Phi_{B0}+\gamma q(V-R_sI)]/kT} = I_0 e^{-\gamma q(V-R_sI)/kT}. \tag{3.17}$$

By re-defining the ideality factor as:

$$\frac{1}{m} \equiv \frac{1}{n} - \gamma = \frac{1}{n} - \frac{1}{q}\frac{\partial\Phi_B}{\partial(V - R_sI)}, \tag{3.18}$$

eqs. (3.1) and (3.17) can be combined to obtain:

$$I = I_0 e^{q(V-R_sI)/mkT}\left[1 - e^{-q(V-R_sI)(1/m+\gamma)/kT}\right] =$$

$$= I_0\left[e^{q(V-R_sI)/mkT} - 1\right] - I_0\left[e^{-q(V-R_sI)\gamma/kT} - 1\right], \tag{3.19}$$

which includes an ideality factor for both the forward and reverse current. From a circuital viewpoint, eq. (3.19) corresponds to the parallel of two opposite diodes, with ideal factors m and γ^{-1} respectively, in series with the resistance R_s, as shown in the inset of Fig. 3.6(b). In forward bias, the current originates mostly from electrons injected from Si into graphene, and is controlled by the Si band-bending barrier, $q(\phi_i - V/m)$ (Fig. 3.6(a)). The ideality factor m (which the fit of Fig. 3.6(b) shows to be $\approx n$) is predominantly caused by inadvertent interface layers and other deviations from pure thermionic emission. In reverse bias, the Schottky barrier is significantly lowered by the applied voltage because of the limited DOS of graphene (Fig. 3.6(a)). This causes an exponential increase of the electrons flowing from graphene into Si, i.e. of the reverse current, which is modeled by a diode of ideality factor γ^{-1}, which obviously takes into account the strong bias dependence of the Schottky barrier height.

Fig. 3.6(b) shows that eq. (3.19) provides an excellent fit to the measured data at 300 K over the whole bias range (the flat-band regime obeys a quadratic law, as explained before). The dependence of I_0 as the exponential of a linear rather than a sub-liner function of $|V|$ is likely due to the effect of Si substrate which, especially in the vicinity of the tips (Fig. 3.3(d)), acts as strongly-coupled gate that would linearly shift E_F. Consequently, the Gr/Si-tip device behaves as a barristor, with linear control of the Schottky barrier height as for the device of Yang et al. [11], but without the need of a third gate electrode.

Another important effect which can lead to a stronger V-dependence of the reverse current is the Schottky barrier lowering caused by hot electrons [58-59] that might originate even a quadratic $\Delta\Phi_B(V)$. In this scenario, the gating effect induces abrupt band bending around the Schottky barrier that increases the lateral field, which in turn produces significant enhancement of hot carriers.

3.3.2 Photoresponse

We also studied the photoresponse of the Gr/Si-tip device by shining light from the top, on the graphene layer.

Fig. 3.7(a) compares the I-V curves obtained in darkness and under 3 mV/cm^2 white LED light; it shows clear photocurrent in reverse bias, and photovoltaic effect with 60 nA short circuit current (a factor ~ 50 higher than the dark current at zero bias) and 70 mV open circuit voltage. In reverse bias, the Gr/Si-tip device can be used as a photodetector: the electron-hole pairs generated by incident photons in the Si space-charge region and, in minor part, in the Si quasi-neutral region or in graphene are separated by the strong tip-enhanced electric field, leading to a photocurrent [19]. The inset of Fig. 3.7(a) shows the stable photoresponse when the light is switched on and off, at a bias of - 0.5 V, corresponding to a responsivity:

$$R_{ph} = I_{ph}/P_0 = \left(I_{ligth} - I_{dark}\right)/P_0 \approx 3\ A/W, \tag{3.20}$$

where I_{ph} is the photocurrent and P_0 the incident optical power.

Fig. 3.7(b) shows the photoresponse, at the same bias of - 0.5 V, to the near IR radiation produced by a 880 nm LED. The Gr/Si-tip device is expected to show high sensitivity around this wavelength, since Si has an absorption peak at ~ 930 nm [3]. The current plateaus of Fig. 3.7(b) and of its top inset are the response of the Gr/Si-tip device to stepwise changes of electrical power fed into the irradiating diode: the photocurrent displays a monotonic growth

with IR intensity (as seen also in the bottom insets of the figure). The radiation intensity in W/cm^2 reaching the Gr/Si-tip junction was measured to be ≤ 1% of the IR diode supply power. Hence, Fig. 3.7(b) shows that the minimum detectable IR intensity by the Gr/Si-tip heterojunction is less than 100 $\mu W/cm^2$ and its responsivity is $R_{ph} \geq 0.3$ A/W at intensity < 1 mW/cm^2. The measured responsivity is one or two orders of magnitude higher than the values reported to date for graphene/Si planar-junctions [3,60-63] (with maximum of 225 *mA*/*W* at 488 *nm*) [1].

The graphene/Si-tip device appears also competitive when compared to semiconductor photodiodes on the market, whose typical responsivity is around 0.5 *A*/*W*, both for visible and near IR light.

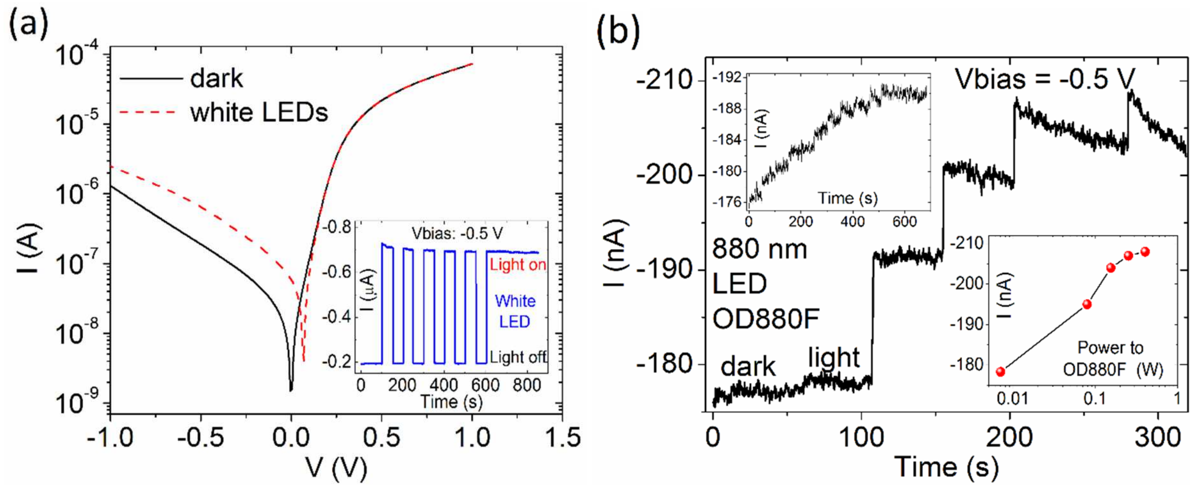

FIGURE 3.7: (a) *I-V* characteristics of the graphene/Si-tip device in dark and under white LED illumination. The inset show the current at $V = -0.5$ V in a sequence of light on/off cycles. (b) Reverse current at $V = -0.5$ V under 880 *nm* IR irradiation, increased in time by stepwise changes of the input electrical power to the emitting diode (OD880F). The top inset displays the monotonic increase of the photocurrent of the graphene/Si-tip device while the IR diode input power is changed in smaller steps. The bottom inset shows the current of the graphene/Si-tip vs. the IR diode input electrical power.

The high substrate doping reduces the space-charge region where most of the photoexcitation takes place and this should suppress the responsivity. This loss can be counterbalanced by the textured surface, which on the contrary favors multiple reflections and light absorption [64].

However, the high value of responsivity is rather a result of the peculiar device geometry. The tip-enhanced electric field, other than facilitating their separation, can provide photogenerated electron-hole pairs with enough kinetic energy to cause impact ionization and initiate charge multiplication, thus enabling device internal gain. The exponential increase of the photocurrent with reverse bias can be taken as signature of internal gain since smoother

rise is usually observed when the photocurrent is due only to increased photon absorption in the bias-widened depletion layer. Augmented photocharge separation and multiplication is also expected in graphene, especially in the areas near the tips.

We notice that very high responsivity of $10^7\ A/W$ have been reported by Liu et al. [51] in more complex three-terminal Gr/Si devices with quantum gain due to photocarriers borrowed into graphene and reinvested several times in the external circuit during their lifetime. However, these devices require more complex circuitry than our multi-purpose two-terminal photodiode.

3.4 Conclusions

We characterized extensively a novel Gr/Si heterojunction obtained by CVD graphene transfer over a nanotip patterned Si-substrate. We measured the relevant junction parameters and showed better performance of the Gr/Si-tip device with respect to its planar counterpart. Without adding barrier inhomogeneity, the tip geometry enables linear tuning of the Schottky barrier height, hence of the diode current, by a single applied bias, thus implementing a two terminal barristor. The textured surface improves light absorption and photocharge collection and enables internal gain through impact ionization leading to higher responsivity.

This study represents a step forward toward the integration of graphene into existing Si technology for new generation optoelectronic devices.

Bibliography

[1] An X, Liu F, Jung Y J and Kar S 2013 *Nano Lett.* **13** 909–916.

[2] Ferrari A, Bonaccorso F, Fal'ko V, Novoselov K S, Roche S, Bøggild P, Borini S, Koppens F H, Palermo V, Pugno N et al. 2015 *Nanoscale* **7** 4598-4810.

[3] Riazimehr S, Bablich A, Schneider D, Kataria S, Passi V, Yim C, Duesberg G S and Lemme M C 2016 *Solid-State Electronics* **115** 207-212.

[4] An X, Liu F and Kar S 2013 *Carbon* **57** 329–337.

[5] Behura S K, Nayak S, Mukhopadhyay I and Jani O 2014 *Carbon* **67** 766–774.

[6] Ruan K, Ding K, Wang Y, Diao S, Shao Z, Zhang X and Jie J 2015 *J. Mater. Chem. A* **3** 14370-14377.

[7] Kim H Y, Lee K, McEvoy N, Yim C and Duesberg G S 2013 *Nano Lett.* **13** 2182–2188.

[8] Singh A, Uddin A, Sudarshan T and Koley G 2014 *Small* **10** 1555-1565.

[9] Fattah A, Khatami S, Mayorga-Martinez C C, Medina-Sánchez M, Baptista-Pires L and Merkoçi A 2014 *Small* **10** 4193–4199.

[10] Di Bartolomeo A, Giubileo F, Santandrea S, Romeo F, Citro R, Schroeder T and Lupina G 2011 *Nanotechnology* **22** 275702.

[11] Yang H, Heo J, Park S, Song HJ, Seo DH, Byun K E, Kim P, Yoo IK, Chung H J and Kim K 2012 *Science* **336** 1140-1143.

[12] Mehr W, Dabrowski J, Scheytt J C, Lippert G, Xie Y H, Lemme M C, Ostling M and Lupina G 2012 *IEEE Electron Device Lett.* **33** 691–693.

[13] Di Bartolomeo A, Santandrea S, Giubileo F, Romeo F, Petrosino M, Citro R, Barbara P, Lupina G, Schroeder T and Rubino A 2013 *Diamond Rel. Mat.* **38** 19–23.

[14] Vaziri S, Smith AD, Östling M, Lupina G, Dabrowski J, Lippert G, Mehr W, Driussi F, Venica S, DiLecce V, Gnudi A, König M, Ruhl G, Belete M and Lemme M C 2015 *Solid State Commun.* **224** 64–75.

[15] Tongay S, Lemaitre M, Miao X, Gila B, Appleton BR and Hebard AF 2012 *Phys. Rev. X* **2** 011002.

[16] Di Bartolomeo A, Giubileo G, Luongo G, Iemmo L, Martucciello M, Niu G, Fraschke M, Skibitzki O, Schroeder T and Lupina G 2017 *2D Mater.* **4** 015024.

[17] Mehr W, Wolff A, Frankenfeld H, Skaloud T, Höppner W, Bugiel E, Lärz J and Hunger B 1996 *Microelectron. Eng.* **30** 395–398.

[18] Niu G, Capellini G, Lupina G, Niermann T, Salvalaglio M, Marzegalli A, Schubert MA,

Zaumseil P, Krause H M, Skibitzki O, Lehmann M, Montalenti F, Xie Y H and Schroeder T 2016 *ACS Appl. Mat. and Interf.* **8** 2017-2026.

[19] Niu G, Capellini G, Schubert MA, Niermann T, Zaumseil P, Katzer J, Krause H M, Skibitzki O, Lehmann M, Xie Y H, von Känel H and Schroeder T **2016** *Sci. Rep.* **6** 22709.

[20] Lupina G, Kitzmann J, Costina I, Lukosius M, Wenger C, Wolff A, Vaziri S, Ostling M, Pasternak I, Krajewska A et al. 2015 *ACS Nano* **9** 4776-4785.

[21] Lupina G, Lukosius M, Kitzmann J, Dabrowski J, Wolff A and Mehr W 2013 *Appl. Phys. Lett.* **103** 183116.

[22] Ferrari AC and Basko DM 2013 *Nat. Nanotech.* **8** 235-246.

[23] Lee J K, Park C S and Kim H 2014 *RSC Advances* **4** 62453-62456.

[24] Di Bartolomeo A, Giubileo F, Romeo F, Sabatino P, Carapella G, Iemmo L, Schroeder T and Lupina G 2015 *Nanotechnology* **26** 475202.

[25] Tung RT 2001 *Mat. Sci. and Eng.* **R35** 1-138.

[26] Tung RT 2014 *Appl. Phys. Rev.* **1** 011304.

[27] Di Bartolomeo A 2016 *Physics Reports* **606** 1-58.

[28] Schroder DK *Semiconductor material and device characterization*, 2007 Wiley Interscience, Hoboken, New Jersey.

[29] Sze SM and Ng KK *Physics of semiconductor devices,* 2007 Wiley Interscience, Hoboken, New Jersey.

[30] Cheung SK and Cheung NW 1986 *Appl. Phys. Lett.* **49** 85.

[31] Olikh OY 2015 *J. Appl. Phys.* **118** 024502.

[32] Werner JH 1988 *J. Appl. Phys.* **47** 291-300.

[33] Li SS and Thurber WR 1977 *Solid-State Electronics* **20** 609-616.

[34] Jacoboni C, Canali C, Ottaviani G and Alberigi Quaranta A 1977 *Solid-State Electronics* **20** 77-89.

[35] Swirhun SE and Swanson RM 1986 *IEEE Electr. Dev. Lett.* **7** 155-157.

[36] Bolotin KI, Sikes KJ, Hone J, Stormer HL and Kim P 2008 *Phys. Rev. Lett.* **101** 096802.

[37] Shao Q, Liu G, Teweldebrhan D and Balandin AA 2008 *Appl. Phys. Lett.* **92** 202108.

[38] Skákalová V, Kaiser AB, Yoo JS, Obergfell D and Roth S 2009 *Phys. Rev. B* **80** 153404.

[39] Heo J, Chung HJ, Lee S H, Yang H, Seo DH, Shin JK, Chung U I, Seo S, Hwang EH and Das Sarma S 2011 *Phys. Rev. B* **84** 035421.

[40] Liu Y, Liu Z, Lew WS and Wang QJ 2013 *Nano. Res. Lett.* **8** 335.

[41] Liu Y, Li W, Qi M, Li X, Zhou Y and Ren Z 2015 *Physica E* **69** 115–120.

[42] Fang X Y, Yu X X, Zheng H M, Jin H B, Wang L and Cao M S 2015 *Phys. Lett. A* **379**

2245–2251.

[43] Werner JH and Güttler HH 1991 *J. Appl. Phys.* **69** 1522-1533.

[44] Parui S, Ruiter R, Zomer PJ, Wojtaszek M, Van Wees BJ and Banerjee T 2014 *J. Appl. Phys.* **116** 244505.

[45] Sinha D and Lee JU 2014 *Nano Lett.* **14** 4660-4664.

[46] Tomer D, Rajput S, Hudy LJ, Li CH and Li L 2015 *Nanotechnology* **26** 215702.

[47] Liang S-J and Ang L K 2015 *arXiv:1503.02758v2*.

[48] Liang S-J and Ang LK 2015 *Phys. Rev. Applied* **3** 014002.

[49] Khurelbaatar Z, Kil Y H, Shim K H, Cho H, Kim M J, Kim Y T and Choi C J 2015 *J. Semicond. Techn. Sci.* **15** 7-15.

[50] Chen C C, Aykol M, Chang C C, Levi AFJ and Cronin SB 2011 *Nano Lett.* **11** 1863-1867.

[51] Liu F and Kar S **2014** *ACS Nano* **8** 10270-10279.

[52] Zhong H, Xu K, Liu Z, Xu G, Shi L, Fan Y, Wang J, Ren G and Yang H 2014 *J. Appl. Phys.* **115** 013701.

[53] Khomyakov PA, Giovannetti G, Rusu PC, Brocks G, van den Brink J and Kelly PJ 2009 *Phys. Rev. B* **79** 195425.

[54] Song SM, Park JK, Sul OJ and Cho BJ 2012 *Nano Lett.* **12** 3887-3892.

[55] Xu Y, He KT, Schmucker SW, Guo Z, Koepke JC, Wood JD, Lyding JW and Aluru NR 2011 *Nano Lett.* **11** 2735–2742.

[56] Lin Y J and Zeng J J 2014 *Appl. Surf. Science* **322** 225-229.

[57] Rideout VL 1978 *Thin Solid Films* **48** 261-291.

[58] Chang W, Shih C H, Luo Y X, Wu W F and Lien C 2014 *Jap. J. Appl. Phys.* **53** 094001.

[59] Mao L F, Ning H, Huo Z L and Wang J Y 2015 *Sci. Rep.* **5** 18307.

[60] Echtermeyer T J, Britnell L, Jasnos P K, Lombardo A, Gorbachev RV, Grigorenko, AN, Geim AK, Ferrari AC and Novoselov KS 2011 *Nat. Commun.* **2** 458.

[61] Furchi M, Urich A, Pospischil A, Lilley G, Unterrainer K, Detz H, Klang P, Andrews AM, Schrenk W, Strasser G and Mueller T 2012 *Nano Lett.* **12** 2773−2777.

[62] Amirmazlaghani M, Raissi F, Habibpour O, Vukusic J and Stake J 2013 *IEEE J. Quant. Electr.* ***49*** 589-594.

[63] Lv P, Zhang Xiujuan, Zhang Xiwei, Deng W and Jie J 2013 *IEEE Elect. Dev. Lett.* **34** 1337-1339.

[64] Khan F, Baek S H, Kaur J, Fareed I, Mobin A and Kim JH 2015 *Nano. Res. Lett.* **10** 376-384.

Chapter 4

Transport and field emission properties of CNTs

4.1 Introduction

Since their discovery, carbon nanotubes (CNTs) [1] have been considered exceptional elements to realize field emission devices, due to their very high aspect ratio, excellent electrical conductivity and important mechanical strength. Nowadays, CNT-based field emitters are used in vacuum electronics to produce electron sources [2], flat panels [3], X-ray sources [4,5], and microwave amplifiers [6], exploiting a low-threshold electric field and large emission current density. To increase the extracted current, CNT arrays are usually implemented [7,8] as free-standing well-aligned CNTs [9-11] or paper-like sheet of randomly oriented CNTs, named buckypaper [12,13].

Several reports focus on oriented samples grown on particular substrates to improve the control on dimension and spacing of CNT emitters and to get stable emitted current [14-16]. However, growth of oriented nanostructures needs carefully controlled fabrication process. The development of buckypaper field emitters is motivated by the extreme simplicity of fabrication process especially for large scale as well as ease to use. Buckypapers have a laminar structure with networks of CNTs held together by van der Waals forces. The CNTs are randomly oriented in the plane unless special techniques, as the application of electric and magnetic fields, are adopted [17] to obtain preferential alignment in one direction. The material results a good candidate for large scale emitters for the possibility to emit electrons from the whole length of the tubes [18]. Recently, buckypapers have been applied to develop supercapacitors [19,20], chemical sensors [21], flexible fibers [22] and actuators [23]. Enhancement of field emission in buckypaper has been also reported due to acid functionalization of nanotubes [24] and surface plasma treatment [19].

In this chapter, we study the field emission properties of 120 μm thick buckypaper obtained by pressing aligned CNTs whose original length was up to 200 μm. The temperature dependence of the buckypaper conductance was measured in the wide temperature range 4.2 K – 430 K evidencing the presence of thermal fluctuation induced tunneling contribution

as well as a linear contribution to the total conductance. The field emission characteristics are locally measured by using a piezoelectric driven metallic probe tip, with curvature radius of about 30 *nm*, in order to collect electrons emitted from areas as small as 1 μm^2 of the buckypaper. We analyze the turn-on field, the emission current intensity and its time stability as well as the possibility to modify the FE current by applying an additional planar current in the sample [25].

4.2 Samples fabrication and measurement setup

Samples have been produced at the University of Salerno. The chemical vapor deposition (CVD) method was used to grow CNTs on a quartz wafer in a two-step process consisting of a catalyst preparation followed by the actual synthesis of the CNTs. The quartz wafer cut into appropriate size was first heated in a furnace at 500 $°C$ for about 10 minutes. It was then cooled down to the room temperature and dipped in catalyst. The catalyst was basically a solution of ethanol and Fe-Mo in mole ratio of 10:1. The quartz substrate thus dipped in catalyst was then placed in a quartz tube in a tube furnace. The deposited Fe catalyst was then reduced at 800 $°C$ by passing hydrogen and argon gas. Finally, the substrate was subjected to source of carbon by passing ethylene gas which caused the decomposition of carbon and resulted in the synthesis of CNTs. As can be seen from the scanning electron microscope (SEM) images shown in Fig. 4.1(a), the CNTs produced with this procedure are aligned, with length ranging from several micrometers to about 200 μm with a narrow diameter distribution around 10 *nm*. Raman spectroscopy shows that the obtained aligned CNTs are a mixture of single and multiwalled carbon nanotubes (Fig. 4.1(b)). Subsequent steps were carried out to press the sample between two parallel plates to make the film denser and to separate it from the substrate in the form of buckypaper of about 120 μm thick (Fig. 4.1(c))

Even though this process is focused on making 100% multi-walled carbon nanotubes (MWCNTs) it produced a mixture of single-walled carbon nanotubes (SWCNTs) as well. This is shown by the 200 cm^{-1} peak in the Raman spectrum reported in Fig. 4.1(b). This peak corresponds to the Radial Breathing Mode (RBM), which is usually located between 75 and 300 cm^{-1} [26]. The D mode (located between 1330-1360 cm^{-1}) and the G mode, which corresponds to the stretching mode in the graphite plane, are typical of good quality MWCNTs [27].

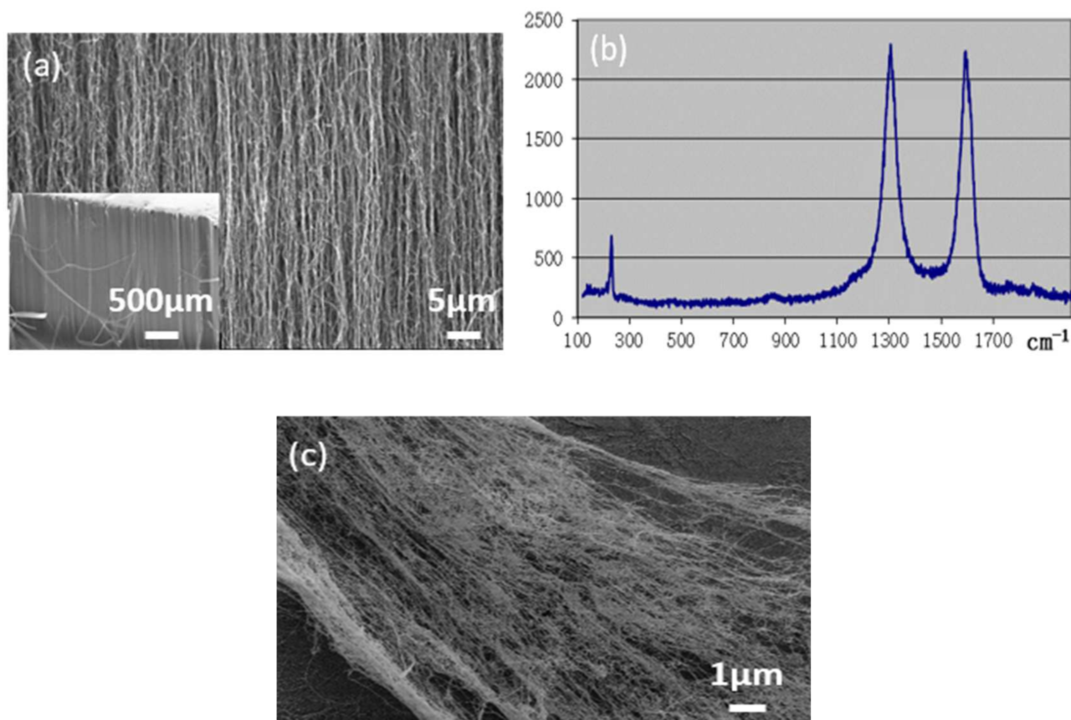

FIGURE 4.1: (a) SEM images of aligned carbon nanotubes on quartz substrate. (b) Raman spectrum of vertically aligned CNTs with peak at 200 cm^{-1} corresponding to RBM of single walled CNTs. The D mode (located between 1330-1360 cm^{-1}) and the G mode are typical of good quality MWCNTs. (c) SEM image of the surface of as pressed 120 μm thick CNT buckypaper.

A standard four-probe method was applied to perform the electrical characterization of the produced samples by means of Janis ST-500 Cryogenic probe station working in the temperature range from 4.2 *K* to 450 *K* and in vacuum (pressure range from 10^{-6} *mbar* to ambient atmosphere). A semiconductor parameter analyzer (Keithley 4200-SCS) with four source-measurement units was connected to the probe station via triaxial cabling to perform current biased measurements, while controlling/monitoring the sample temperature.

To study field emission properties, we connected the Keithley 4200-SCS to a nanoprobe system manufactured by Kleindeik Company (nanomanipulators MM3A), with two piezoelectric driven arms, installed inside a Zeiss LEO 1430 SEM, allowing electrical measurements in situ by means of nanometric metallic probes (tungsten tips with 30 *nm* curvature radius). To perform field emission characterization, current–voltage characteristics are measured by sweeping the voltage bias from 0 to 120 *V*. Larger bias was not applied to prevent damages to the nanomanipulator circuitry. The emitted current was measured with an accuracy better than 0.1 *pA*. All the field emission measurements were performed in a high vacuum (< 10^{-6} *mbar*) at room temperature.

4.3 Results and discussion

4.3.1 The temperature dependence of the conductance

We measured the temperature dependence of the resistance *R(T)* for several samples (randomly cut from the same source sample), and we observed a negative temperature coefficient of the resistance (*dR/dT* < 0) in the whole temperature range (4.2 - 300 *K* in Fig. 4.2(a) and 100 - 430 *K* in Fig. 4.2(b)). Measurements were performed by forcing a low constant current (0.5 *mA*) to prevent sample self-heating. For MWCNT bundles [28,29] or film [30] the temperature dependence of resistivity usually remains non metallic, *dR/dT* < 0, for the whole temperature range. A crossover temperature from metallic to non metallic has been reported in MWCNT buckypaper [31]. Differently, for SWCNTs a crossover temperature has been often observed with values varying from 35 *K* for a single well-ordered rope to 250 *K* for a rope with tangled regions [32]. It appears difficult to establish a consistent scenario for the MWCNTs also considering that below 20 *K*, both sharp increases in resistivity [28,33] and plateaus [29,34] have been reported for bundles and individual tubes.

From a theoretical viewpoint, for homogeneous disordered systems, the non metallic temperature dependence of the conductivity is explained in terms of variable range hopping (VRH) conduction [35], with:

$$\sigma(T) = \sigma_0 \cdot exp\left[-\left(\frac{T_0}{T}\right)^{\frac{1}{1+d}}\right], \quad (4.1)$$

where *d* is the dimension of the system.

Alternatively, according to the thermal fluctuation induced tunneling (FIT) model [36], the conductivity is:

$$\sigma(T) = \sigma_0 \cdot exp\left[-\frac{T_1}{T+T_0}\right], \quad (4.2)$$

where σ_0 is the conductance at room temperature, T_1 denotes the temperature below which the conduction is dominated by the charge carrier tunneling through the barrier and T_0 the temperature above which the thermally activated conduction over the barrier begins to occur. FIT model has been developed for disordered heterogeneous systems such as conductor/insulator composites, granular metals, and disordered semiconductors, characterized by large conductive filaments interconnected via small insulating gaps. Due to

small sizes of tunnel junction, thermal voltage fluctuation influences the electron tunneling probability through the barrier.

Electronic transport characterization measurements have sometimes shown that both VHR and FIT can give both reasonable fits; in real situations, it can be difficult to determine the dominant mechanism responsible for the observed electrical conduction.

By fitting the experimental data reported in Fig. 4.2(a), we found out that the best fit over the largest temperature range ($T \geq 20$ K) is obtained by the FIT model. For our system, the tunneling barriers originate from the inter-tubular contacts and the buckypaper can be considered a heterogeneously disordered system. For this reason, the FIT was used for describing the temperature dependence of conductivity of SWCNTs fibers [37] and networks [38] as well as for MWCNTs [39].

However, when considering our experimental data in the whole interval from 4.2 to 300 K, neither FIT nor VRH are able to reproduce the complete behavior.

To explain temperature dependence measured down to 4.2 K on CNT mats [40,41], a further negative linear term has been sometimes introduced [42]. A linear conductance has also been observed in gas-desorbed CVD-grown MWCNTs at high temperature, and it has been explained using a thermal activation picture of conduction channels. Moreover, such a linear dependence could imply a very short mean free path due to large number of defects [43]. Hence, to observe such a linear dependence, “dirty” MWCNTs with mean free path of few nanometers are necessary. Larger values up to two order of magnitude more can be obtained in “clean” MWCNTs, characterized by limited numbers of defect scatterers [44-46].

By considering a further linear contribution, we can express the total conductance as:

$$G(T) = G_0 \cdot exp\left[-\frac{T_1}{T+T_0}\right] + G_1 T, \tag{4.3}$$

obtaining a perfect fit of the experimental data in the whole temperature range from 4.2 to 300 K (inset of Fig. 4.2(a)).

The fitting parameters T_1 and T_0 are defined as:

$$T_1 = \frac{16\, \varepsilon_0 \hbar A V_0^{3/2}}{\pi\, e^2 k_B (2m_e)^2\, w^2}, \tag{4.4}$$

$$T_0 = \frac{8\, \varepsilon_0 A V_0^2}{e^2 k_B w}, \tag{4.5}$$

where ε_0 is the vacuum permittivity, $\hbar$ the reduced Planck constant, A the junction area, V_0 the height of the barrier, w the width of the tunnel junction, e the electronic charge, m_e the electron mass and k_B the Boltzmann constant. The linear correction to the total conductance is not used to fit the experimental data measured in the range (100 – 430 K) for another sample (Fig. 4.2(b),). By assuming a junction area $A \approx d^2$ with $d \approx 10$ nm the average MWCNT diameter, from the fitting parameters, we can estimate a junction width $w \approx 3.0$ nm and $V_0 \approx 24$ meV. V_0 is the tunnel barrier that electrons have to overcome to move from one nanotube to another one, and the tunnel probability depends on it as well as on the local density of states of each side of the junction. The effective barrier height depends on the bias current and on the temperature [47,48]. Small V_0 values have been reported when, at low temperatures, current bias above 100 μA are applied [49].

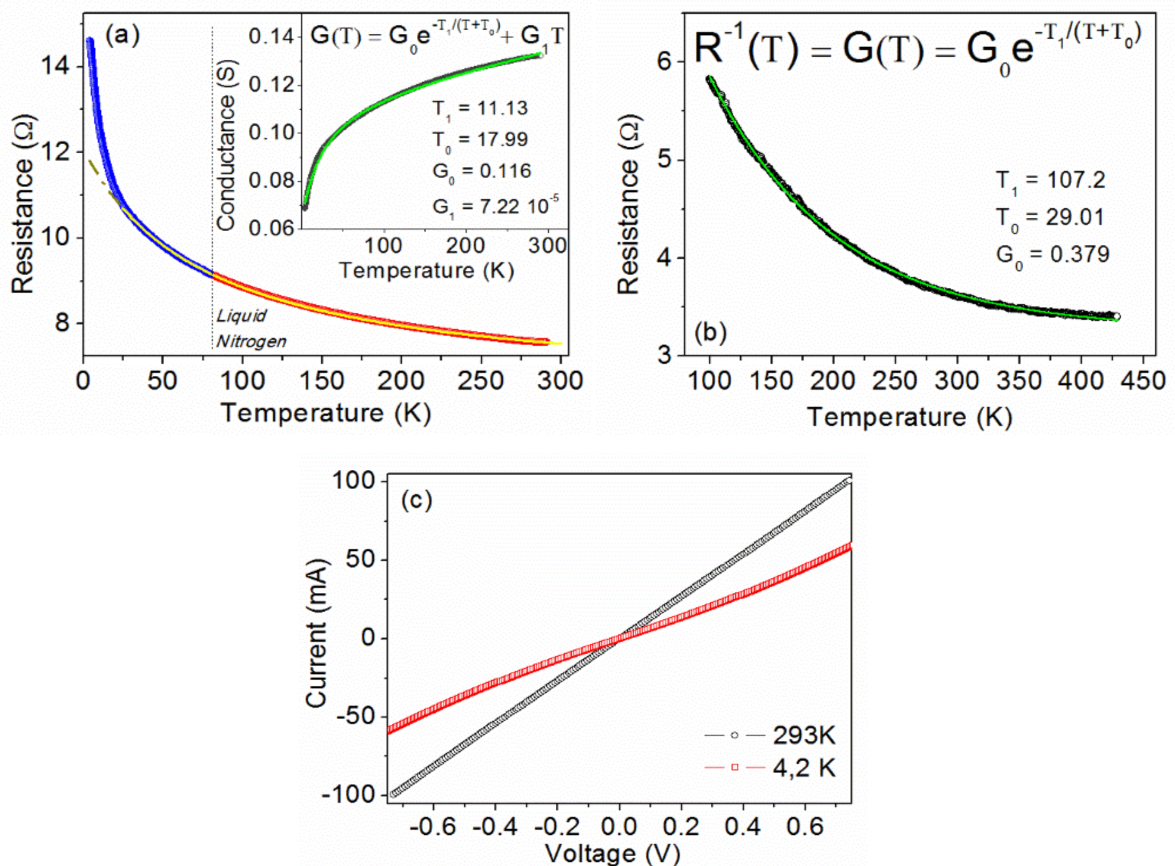

FIGURE 4.2: (a) Resistance vs. temperature for a MWCNT buckypaper measured in the temperature range from 4.2 to 300 K. Solid line (white and yellow) is the best fit by fluctuation induced tunneling model for data in the range 20 - 300 K. Inset: the whole set of data is plotted as $G = 1/R$ and is fitted by adding to the model a linear term $G_1 \cdot T$. Solid (green) line represents the best fit. (b) Resistance vs. temperature for another MWCNT buckypaper measured in the temperature range from 100 to 430 K. Solid line (green) is the best fit by fluctuation induced tunneling model. (c) Current-Voltage characteristics measured at room temperature and at 4.2 K.

We also measured the current-voltage characteristics at different temperatures. For both samples, we always found a linear ohmic dependence, except for low temperatures. We report in Fig. 4.2(c) the curve measured at low temperature (4.2 *K*) for the first sample, and it is compared to the room temperature characteristic. Such non-ohmic behavior of the *I-V* characteristic has been observed at low temperature in SWCNT network [38,50,51] and explained by developing an electrical model that considers series-parallel connections of junctions existing in the CNT bundles [51].

4.3.2 Field emission

In Fig. 4.3(a) we show the current-voltage characteristic of the buckypaper, measured by landing the two nanoprobes on macroscopic silver paint pads to favor very stable and low resistance contacts. This curve is compared to the case in which one contact is realized by pressing the metallic tip directly on the buckypaper. The experimental data confirm that silver paint is useful to reduce the contact resistance. This is not relevant for four-contact measurements (as for temperature dependence measurements of the resistance previously reported), but it is important for the two terminal measurements, discussed in this section.

The circuit configuration for field emission characterization is easily obtained by retracting one of the probes and adjusting its distance *d* from the buckypaper surface (far from the Ag pad). A schematic of the circuit is shown in Fig. 4.3(b). The piezoelectric control of the probe tips allows fine tuning of the cathode (buckypaper)-anode (metallic tip) distance with spatial resolution down to 5 *nm*.

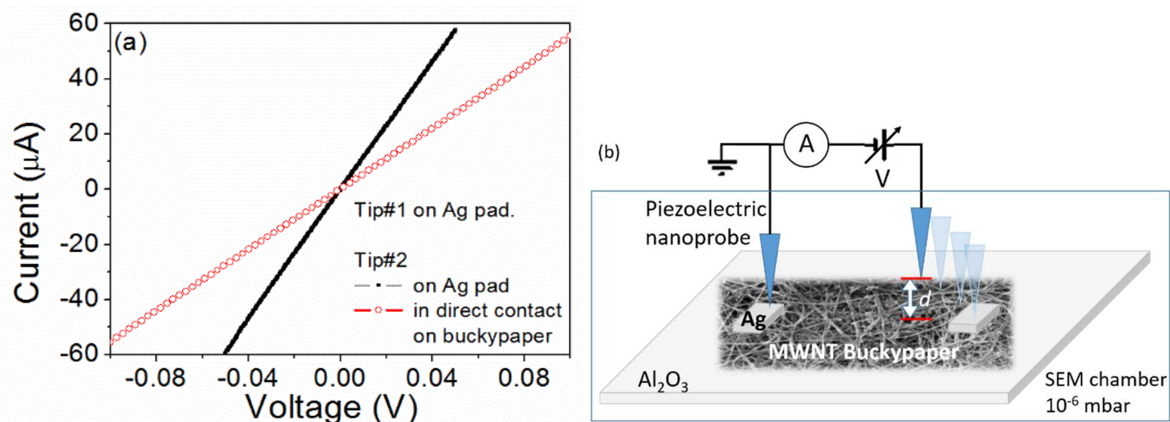

FIGURE 4.3: (a) Two-probe measurement of the Current–Voltage characteristics of the buckypaper inside the SEM chamber by means of nanoprobes. Solid circles refer to configuration in which both metallic tips contact the sample on silver pads; empty squares refer to the case of one tip in direct contact with the buckypaper surface. (b) Schematic of the experimental setup.

The use of a metallic tip as collector of the emitted electrons is a well established technique [9,10,12] that allows to get local information about the field emission properties, the electrons being emitted from a reduced area (of the order of 1 μm^2) with respect the standard parallel plate setup (generally probing areas up to several mm^2).

In Fig. 4.4(a) we report two successively measured FE current-voltage characteristics, in the voltage bias range from 0 to 120 V, under a vacuum better than 10^{-6} *mbar* at room temperature. As standard procedure, we typically perform at least two successive sweeps in order to verify the repeatability of the measurement that gives information about the robustness of the device against the electrical stress induced modifications. The experimental data of Fig. 4.4(a) show a current starting to flow around 50 V and exponentially growing for about eight order of magnitudes (up to several μA) from the setup floor noise of about 10^{-13} A.

To confirm the FE nature of the measured current, we analyze the data according to the Fowler-Nordheim (FN) theory [52], which, as already exposed in chapter 1, expresses the emitted current as:

$$I = a\frac{E_S^2}{\Phi}S \cdot exp\left(-b\frac{\Phi^{3/2}}{E_s}\right), \tag{4.6}$$

where Φ is the work function of the CNTs, S is the emitting area, $a = 1.54 \cdot 10^{-6}\ A \cdot eV \cdot V^{-2}$ and $b = 6.83 \cdot 10^9\ eV^{-3/2} \cdot V \cdot m^{-1}$ are constants, and E_S is the applied electric field that depends on the emitter geometry trough the field enhancement factor β as:

$$E_s = \frac{\beta V}{d}, \tag{4.7}$$

V being the applied bias voltage. The factor β represents the ratio between the local electric field on the sample surface and the applied field.

According to FN theory, for FE device we expect a linear relation in the so-called FN plot, $ln(I/V^2)$ versus $1/V$, whose slope $m = k_{eff} b \Phi^{3/2} d/\beta$, can used to estimate β. In the last expression, the tip correction factor k_{eff} takes into account the shape of the collector electrode [10,53]. The inset of Fig. 4.4(a) shows the FN plot for the second sweep reported in the figure. The clear linear dependence demonstrates the FE nature of the recorded current. From the linear fitting, we extract the field enhancement factor $\beta \approx 30$ by considering $k_{eff} \approx 1.6$ [10]. Consequently the turn-on field ($E_{Turn\text{-}ON}$, here defined as the applied field necessary to extract a current of 10^{-11} A) can be evaluated as $E_{Turn\text{-}ON} = 140\ V/\mu m$, a value significantly lower or comparable to what has been observed for other structures, such as aligned MWCNTs [10],

graphene flakes [54] or nanoparticles [55].

In Fig. 4.4(b) we report other FE current versus bias voltage characteristics measured for different values of the tip-sample distance *d*. As expected, increasing the distance, *d* = 550 *nm*, the FE starts at higher applied voltages (~ 65 *V*), while for reduced distance, *d* = 250 *nm*, the FE starts at lower applied voltages (~ 40 *V*). The inset of Fig. 4.4(b) shows the values of the turn-on field evaluated for each distance. We notice that for *d* = 250 *nm* the FE characteristics follow the usual exponential growth up to a voltage of about 60 *V*. Above this voltage, the current is strongly limited despite the increasing bias voltage. This is probably caused by the presence of a series resistance in the circuit causing a significant voltage drop that reduces the applied field when a significant current is flowing.

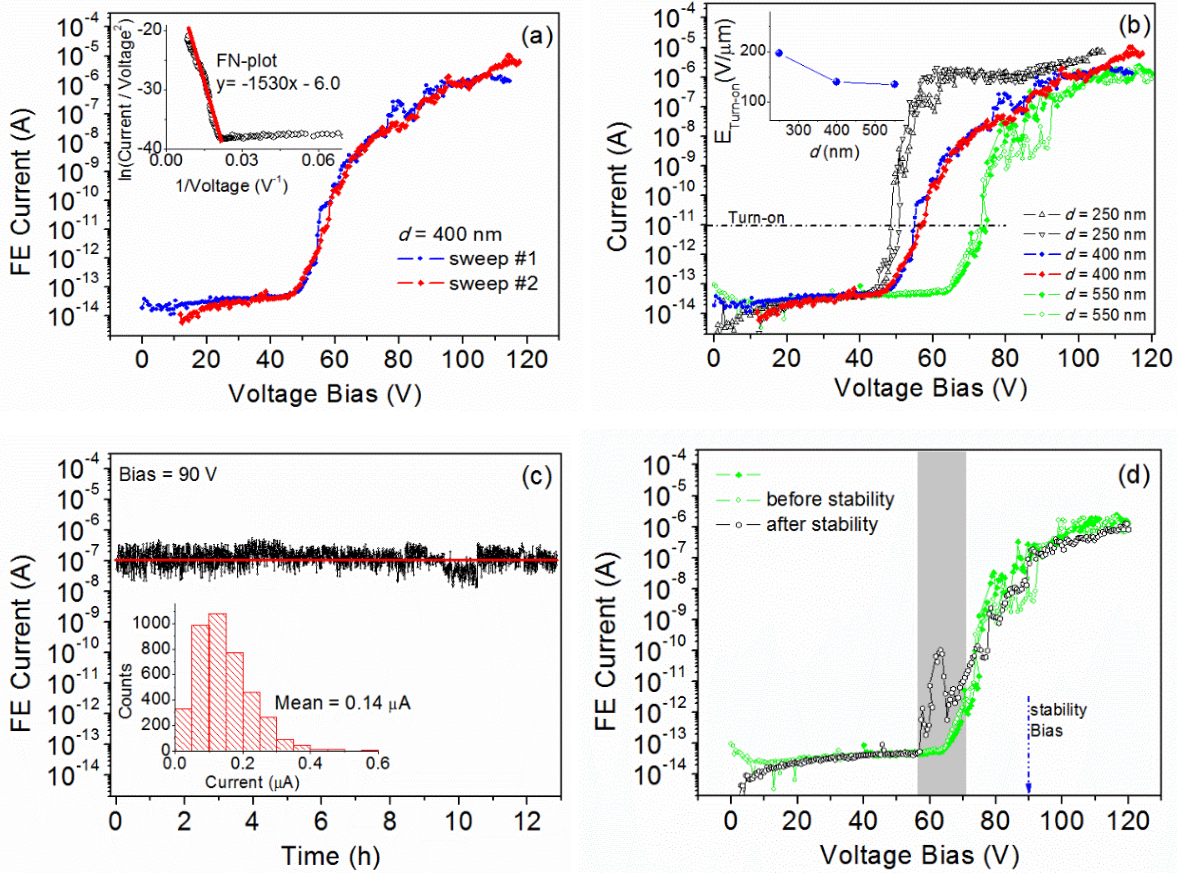

FIGURE 4.4: (a) FE current vs. voltage bias characteristics measured at a tip-sample distance of 400 *nm*. Two successive sweeps are compared. Inset: FN-plot for the second sweep and its linear fitting. (b) FE curves measured for different values of the tip-sample distance *d*. Dashed line represents the current values considered for the evaluation of the turn-on field. Inset: Values of the turn-on field vs. distance, evaluated for each curve of figure 4b. (c) Time stability of the FE current intensity, at fixed bias 90 *V*. Inset: histogram of the measured values with a rate of 1 point each 12 seconds. (d) Comparison of the FE curves measured before and after the stability test. The gray band identifies the region in which the two curves are different.

To study the FE current stability, we used the configuration with d = 550 *nm* and applied constant voltage bias of 90 *V* for measuring the FE current intensity versus time. The result is shown in Fig. 4.4(c). The current has been monitored for more than 12 hours (at a rate of 1 point each 12 seconds) without significant degradation with respect to the average value of 0.14 μA, demonstrating the high stability of the buckypaper with respect to the long duration current emission. After the stability experiment, we repeated the complete voltage sweep (from 0 to 120 *V*) to compare (see Fig. 4.4(d)) the FE characteristics before and after the continuous operation of the device for more than 12 hours. The curve measured after the current annealing was not affected by the long term emission almost in all the bias range. Only near the turn-on bias we observe a peak indicating an anticipated switch on of the emission process probably due to a light morphological modification, such as an elongated CNT out from the buckypaper, induced by the long exposition at high bias during the stability test. However, the high current density may burn it restoring the previous conditions. This demonstrates also the robustness and stability of buckypapers against local modifications during its operation, also better than the case of aligned CNTs, grown on Si wafer. Indeed, for aligned nanotubes, a more pronounced instability is due to the protrusion of tubes of different lengths, allowing higher current but provoking several modifications due to burning of single tubes. This is the reason why with aligned CNTs it is often necessary to perform longer electrical annealing to stabilize the emission [9, 10].

According to the theoretical prediction [56] for graphene-based field effect transistors [57-61], in the presence of a wedge tip, enhanced local electrical field can sensibly increase the probability of electron field emission from graphene toward top gate depending on the channel current. Experimentally, a possible effect of channel current on graphene field emission [56,62] has been also reported. For this reason, we tested the possibility to tune the emitted current from the buckypaper by applying an in-plane current in the sample. The schematic of the device is reported in the inset of figure Fig. 4.5(b).

We initially forced a current flowing in the buckypaper, along the alignment direction, in the range 0 – 100 μA by successive raising steps, while monitoring the FE current obtained at fixed bias of 85 *V*, as done for the usual stability experiment. In Fig. 4.5(a) we observe that the FE current remains insensible to the steps of the in-plane current. Moreover, we tried to apply higher currents (in the *mA* range) without significant modifications. We also compared the complete FE *I-V* characteristics measured with and without forced in-plane current in order to check whether only limited bias regions could be affected by the presence of the in-

plane current. However, experimental data reported in Fig. 4.5(b) show reproducible characteristics that confirm the absence of relevant effects of in-plane current on the spectra.

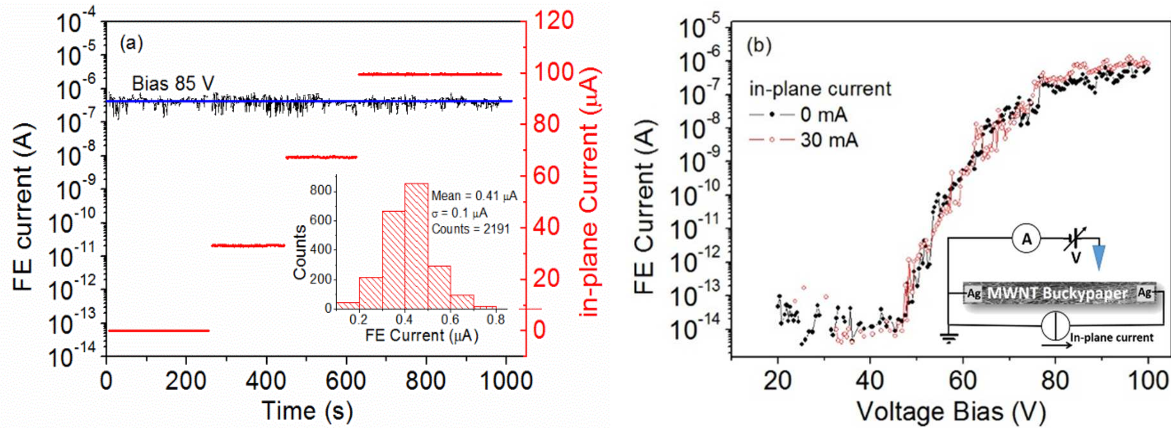

FIGURE 4.5: (a) Time stability of the FE current for voltage bias of 85 *V*. The right axis (red) refers to the applied in-plane current. The measurement starts with zero in-plane current and is raised up to 100 μA in three successive steps. Inset: histogram gives statistic information about the FE current values recorded during the measurement. (b) Comparison of FE curves measured with (30 *mA*) and without in-plane current flowing in the buckypaper. Inset: schematic of the circuit to apply in-plane current during FE experiment.

4.4 Conclusions

We performed a deep experimental characterization of the transport and field emission properties of buckypapers obtained from aligned carbon nanotubes. The temperature dependence of the conductance is described within the fluctuation induced tunneling model, but a further linear contribution is necessary in order to explain the behavior in the wide temperature range from 4.2 to 430 *K*. We demonstrated that our buckypapers are extremely stable emitters with emitted current almost unaffected after half day operating time, reporting also turn-on fields as low as 140 $V/\mu m$ at distance below 1 μm. We finally tested the possibility of FE tuning by forcing in-plane currents up to several *mA* in the buckypaper.

Bibliography

[1] Iijima S 1991 *Nature* **354** 56–8.

[2] Saito Y and Uemura S 2000 *Carbon* **38** 169-182.

[3] Wang Q H, Yan M and Chang R P H 2001 *Appl. Phys. Lett.* **78** 1294–1296.

[4] Zhang J, Yang J, Cheng Y, Gao B, Qiu Q, Lee YZ, Lu JP and Zhou O 2005 *Appl. Phys. Lett.* **86** 184104.

[5] Liu Z, Yang G, Lee YZ, Bordelon D, Lu J and Zhou O 2006 *Appl. Phys. Lett.* **89** 103111.

[6] Teo KBK, Minoux E, Hudanski L, Peauger F, Schnell JP, Gangloff L, Legagneux P, Dieumegard D, Amaratunga GAJ and Milne WI 2005 *Nature* **437** 968–968.

[7] Kim D, Bourée JE and Kim SY 2009 *J. Appl. Phys.* **105** 084315.

[8] Shahi M, Gautam S, Shah PV, Jha P, Khumar P, Rawat JS, Chaudhury PK and Tandon RP 2013 *J. App. Phys.* **113** 204304.

[9] Giubileo F, Di Bartolomeo A, Scarfato A, Iemmo L, Bobba F, Passacantando M, Santucci S and Cucolo AM 2009 *Carbon* **47** 1074–80.

[10] Di Bartolomeo A, Scarfato A, Giubileo F, Bobba F, Biasiucci M, Cucolo AM, Santucci S and Passacantando M 2007 *Carbon* **45** 2957–71.

[11] Liu H, Shi Y, Chen B, Li X, Ding Y and Lu B 2012 *Vacuum* **86** 933-937.

[12] Giubileo F, Di Bartolomeo A, Sarno M, Altavilla C, Santandrea S, Ciambelli P and Cucolo AM 2012 *Carbon* **50** 163-169.

[13] Chen YW, Miao HY, Lin RJ, Zhang M, Liang R, Zhang C and Wang B 2010 *Nanotechnology* **21** 495702.

[14] Rai P, Mohapatra DR, Hazra KS, Misra DS and Tiwari SP 2008 *Appl. Phys. Lett.* **93** 131921.

[15] Weng TW, Lai YH and Lee KY 2008 *Appl. Surf. Sci.* **254** 7755-7758.

[16] Seelaboyina R, Boddepalli, Noh K, Jeon M and Choi W 2008 *Nanotechnology* **19** 065605.

[17] Fischer JE, Zhou W, Vavro J, Llaguno MC, Guthy C, Haggenmueller, Casavant MJ, Walters DE and Smalley RE 2003 *J. Appl. Phys.* **93** 2157-2163.

[18] Knapp W and Schleussner D 2003 *J. Vac. Sci. Technol. B* **21** 557-561.

[19] Roy S, Bajpai R, Soin N, Bajpai P, Hazra KS, Kulshrestha N, Roy SS, McLaughlin JA and Misra DS 2011 *Small* **7** 688-693.

[20] Kaempgen M, Chan CK, Ma J, Cui Y and Gruner G 2009 *Nanoletters* **9** 1872-1876.

[21] Bonanni A, Esplandiu MJ and del Valle M. 2009 *Biosens Bioelectron* **24** 2885-2991.

[22] Behabtu N, Green MJ and Pasquali M 2008 *Nano Today* **3** 24–34.

[23] Baughman RH, Cui C, Zakhidov AA, Iqbal Z, Barisci JN, Spinks GM, Wallace GG, Mazzoldi A, de Rossi D, Rinzler AG, Jaschinski O, Roth S and Kertesz M 1999 *Science* **284** 1340-1344.

[24] Kakade BA, Pillai VK, Late DJ, Chavan PG, Sheini FJ, More MA and Joag DS 2010 *Appl. Phys. Lett.* **97** 073102.

[25] Giubileo F, Iemmo L, Luongo G, Raimondo M, Guadagno L, Passacantando M, Lafdi K and Di Bartolomeo A *Journal of Materials Science*, accepted for publication (doi: 10.1007/s10853-017-0881-4).

[26] Passacantando M, Grossi V and Santucci S 2012 *Appl. Phys. Lett.* **100** 163119.

[27] Heise HM, KucKUK R, Ojha AK, Srivastava A, Srivastava V and Asthana B 2008 *J. Raman Spectrosc.* **40** 344.

[28] Song SN, Wang XK, Chang RPH and Ketterson JB 1994 *Phys. Rev. Lett.* **72** 697-700.

[29] Langer L, Stockman L, Heremans JP, Bayot V, Olk CH, Van Haesendonck C, Bruynseraede Y and Issi J-P 1994 *J. Mater. Res.* **9** 927-932.

[30] de Heer W, Bacsa WS, Châtelain A, Gerfin T, Humphrey-Baker R, Forro L and Ugarte D 1995 *Nature* **268** 845-847.

[31] Di Bartolomeo A, Sarno M, Giubileo F, Altavilla C, Iemmo L, Piano S, Bobba F, Longobardi M, Scarfato A, Sannino D, Cucolo AM and Ciambelli P 2009 *J. Appl. Phys.* **105** 064518.

[32] Fisher JE, Dai H, Thess A, Lee R, Hanjani NM, Dehaas DL and Smalley RE 1997 *Phys. Rev. B* **55** R4921-R4924.

[33] Langer L, Bayot V, Grivei E, Issi JP, Heremans JP, Olk CH, Stockman L, Van Haesendonck C and Bruynseraede Y 1996 *Phys. Rev. Lett.* **76** 479-482.

[34] Kasumov AY, Khodos II, Ajayan PM and Colliex C 1996 *Europhys. Lett.* **34** 429-434.

[35] Mott NF 1967 *Adv. Phys.* **16** 49-144.

[36] Sheng P 1980 *Phys. Rev. B* **21** 2180-2195.

[37] Zhou W, Vavro J, Guthy C, Winey KI, Fisher JE, Ericson LM, Ramesh S, Saini R, Davis VA, Kittrell C, Pasquali M, Hauge RH and Smalley RE 2004 *J. App. Phys.* **95** 649-655.

[38] Kim GT, Jhang SH, Park JG, Park YW and Roth S 2001 *Synth. Met.* **117** 123-126.

[39] Simsek Y, Ozyuzer L, Seyhan AT, Tanoglu M and Schulte K 2007 *J. Mater. Sci.* **42** 9689.

[40] Grigorian L, Williams KA, Fang S, Sumanasekera GU, Loper AL, Dickey EC, Pennycook SJ and Eklund PC 1998 *Phys. Rev. Lett.* **80** 5560-5563.

[41] Kaiser B, Park YW, Kim GT, Choi ES, Düsberg G and Roth S 1999 *Synth. Met.* **103** 2547-2550.

[42] Ebbesen TW, Lezec HJ, Hiura H, Bennett JW, Ghaemi HF and Thio T 1996 *Nature* **382** 54-56.

[43] Zhou F, Lu L, Zhang DL, Pan ZW and Xie SS 2004 *Solid State Comm.* **129** 407-410.

[44] Liu K, Avouris Ph, Martel R and Hsu WK 2001 *Phys. Rev. B* **63** 161404R.

[45] Buitelaar MR, Bachtold A, Nussbaumer T, Iqbal M and Schönenberger C 2002 *Phys. Rev. Lett.* **88** 156801.

[46] Kim J, Lee JO, Park JW, So HM, Kim N, Kang K, Yoo K-H and Kim J-J 2003 *Phys. Rev. Lett.* **90** 166403.

[47] Gao B, Glattli DC, Plaçais B and Bachtoldet A 2006 *Phys. Rev. B* **74** 085410.

[48] Zeldov E, Amer NM, Koren G, Gupta A, McElfresh MW and Gambino RJ 1990 *Appl. Phys. Lett.* **56** 680-682.

[49] Salvato M, Cirillo M, Lucci M, Orlanducci S, Ottaviani I, Terranova ML and Toschi F 2008 *Phys. Rev. Lett.* **101** 246804.

[50] Ksenevich VK, Odzaev VB, Martunas Z, Seliuta D, Valusis G, Galibert J, Melnikov AA, Wieck AD, Novitski D, Kozlov ME and Samuilov VA 2008 *J. Appl. Phys.* **104** 073724.

[51] Salvato M, Cirillo M, Lucci M, Orlanducci S, Ottaviani I, Terranova ML and Toschi F 2012 *J. Phys. D Appl. Phys.* **45** 105306.

[52] Fowler RH and Nordheim L 1928 *Proc. Royal Soc. A* **119** 173-181.

[53] Passacantando M, Bussolotti F, Santucci S, Di Bartolomeo A, Giubileo F, Iemmo L and Cucolo AM 2008 *Nanotechnology* **19** 395701.

[54] Santandrea S, Giubileo F, Grossi V, Santucci S, Passacantando M, Schroeder T, Lupina G and Di Bartolomeo A 2011 *Appl.Phys. Lett.* **98** 163109.

[55] Di Bartolomeo A, Passacantando M, Niu G, Schlykow V, Lupina G, Giubileo F and Schroeder T 2016 *Nanotechnology* **27** 485707.

[56] Cao G, Liu W, Cao M, Li X, Zhang A, Wang X and Chen B 2016 *J. Phys. D Appl. Phys.* **49** 275108.

[57] Di Bartolomeo A, Giubileo F, Iemmo L, Romeo F, Russo S, Unal S, Passacantando M, Grossi V and Cucolo AM 2016 *Appl. Phys. Lett.* **109** 023510.

[58] Di Bartolomeo A, Giubileo F, Romeo F, Sabatino P, Carapella G, Iemmo L, Schroeder T and Lupina G 2015 *Nanotechnology* **26** 475202.

[59] Di Bartolomeo A, Santandrea S, Giubileo F, Romeo F, Petrosino M, Citro R, Barbara P, Lupina G, Schroeder T and Rubino A 2013 *Diamond Rel. Mat.* **38** 19–23.

[60] Di Bartolomeo A, Giubileo F, Santandrea S, Romeo F, Citro R, Schroeder T and Lupina G 2011 *Nanotechnology* **22** 275702.

[61] Schwierz F 2010 *Nat. Nanotechnol.* **5** 487–496.

[62] Wenger C, Kitzmann J, Wolff A, Fraschke M, Walczyk C, Lupina G, Mehr W, Junige M, Albert M and Bartha JW 2015 *J. Vac. Sci. Tech. B* **33** 01A109.

Conclusions

The present thesis work concerned the electrical characterization of different devices like field-effect transistors, diodes and field emission devices based on graphene and carbon nanotubes. The objective of this research was to study electronic properties and transport mechanisms of graphene and carbon nanotubes in these devices.

We presented the fabrication of graphene based field effect transistors (GFETs) with Ti, Ni, Nb and Cr contacts, in bottom and side gate configuration, and we performed their electrical characterization by measuring transfer and output characteristics in order to analyze the channel conductance and to study the physical effects due to the contact resistance between graphene and the metal electrode. We measured an area specific contact resistivity of $\sim 7\ k\Omega\mu m^2$ and $\sim 30\ k\Omega\mu m^2$ for Ni and Ti, respectively, and an edge specific contact resistivity of $\sim 25\ k\Omega\mu m$ for Nb. We showed that the contact resistance is a significant contributor to the total source-to-drain resistance and we proved that it is modulated by the back-gate voltage. We clearly observed the presence of a double-dip feature in the conductance curve for long transistors in bottom gate configuration. This feature is due to the two minima of the density of states of graphene respectively in the channel and under the metal, which are different because of the metal doping induced by the metal-graphene interaction. The transistor transfer characteristics showed a hysteresis that is attributed to charge trapping in silanol group at the gate oxide surface.

We also studied the effects of room temperature vacuum degassing and electron bombardment on the electric properties of graphene FETs with Nb contacts. We clarified the role of adsorbates, PMMA residues and underlying SiO_2 on the channel doping and distinguished it from the doping at the contacts. We showed that weakly chemisorbed Nb acts as p-dopant on graphene and that the asymmetry observed in the transfer characteristics is explained in terms of doping gradient from contact to channel. We discussed how Fermi level depinning at the contact can limit electron conductance and create a resistance plateau in the n-branch. We demonstrated that low energy irradiation is detrimental on the transistor current capability, resulting in an increase of the contact resistance and a reduction of the carrier mobility even at electron doses as low as 30 e^-/nm^2. We also showed that the irradiated devices recover by returning to their pristine state after few repeated electrical measurements,

which we explained as gradual removal of electrons piled up in the gate oxide during e-beam exposure.

Moreover, we characterized side-gated all-graphene field effect transistors with gate-to-channel distance of 100 *nm* and channel width of 500 *nm* on SiO_2/Si substrates. We demonstrated that the side-gate is far more efficient than the back gate in modulating the channel conductance, with a 35% conductance swing over 0.5 *V* and transconductance up to 0.5 *mS/mm* at 10 *mV* drain bias. We measured the planar leakage along the SiO_2/vacuum gate dielectric over a wide voltage range, reporting rapidly growing current above 15 *V*. We unveiled the microscopic mechanisms driving the leakage, as Frenkel-Poole transport through SiO_2 up to the activation of Fowler-Nordheim tunneling in vacuum, which becomes dominant at high voltages. We reported a field-emission current density as high as 1 *μA/μm* between graphene flakes. These findings are essential for the miniaturization of atomically thin devices.

The research activity about diodes focused on the study of a new-concept of Gr/Si photodiode made of a single-layer CVD graphene transferred onto a matrix of nanotips patterned on n-type Si wafer. Through an extensive characterization, we demonstrated tunable Schottky barrier height and record photo-responsivity, and we proved that the multi-junction approach does not add extra-inhomogeneity to the Schottky barrier height distribution. The original layout, where nano-sized graphene/Si heterojunctions alternate to graphene areas exposed to the electric field of the Si substrate, which acts both as diode cathode and transistor gate, results in a two-terminal barristor with single-bias control of the Schottky barrier. The nanotip patterning favors light absorption, and the enhancement of the electric field at the tip apex improves photo-charge separation and enables internal gain by impact ionization. These features render the device a photodetector with responsivity (3 *A/W* for white LED light at 3 mW/cm^2 intensity) almost an order of magnitude higher than commercial photodiodes. This study represents a step forward toward the integration of graphene into existing Si technology for new generation optoelectronic devices.

The research activity related to the carbon nanotubes concerned a deep experimental characterization of the transport and field emission properties of buckypapers obtained from aligned carbon nanotubes. Transport characteristics evidence ohmic behavior in a wide temperature range, non linearity appearing only close to 4.2 *K*. The temperature dependence of the conductance shows that transport is mostly due to thermal fluctuation induced tunneling, although to explain the whole temperature range from 4.2 *K* to 430 *K* a further linear contribution is necessary. The field emission properties were analyzed by means of a

nanocontrolled metallic tip as collector electrode to access local information about buckypaper properties from areas as small as 1 μm^2. Emitted current up to $10^{-5} A$ and turn-on field of about 140 $V/\mu m$ are recorded. We demonstrated that our buckypapers are extremely stable emitters with emitted current almost unaffected after half day operating time, and thus they can be considered excellent candidates for the realization of field emission devices.

Publications

1. Giubileo F, **Iemmo L**, Luongo G, Raimondo M, Guadagno L, Passacantando M, Lafdi K and Di Bartolomeo A, *Transport and field emission properties of buckypapers obtained from aligned carbon nanotubes*, Journal of Materials Science, accepted for publication (doi: 10.1007/s10853-017-0881-4).

2. Di Bartolomeo A, Giubileo F, Luongo G, **Iemmo L**, Martucciello M, Niu G, Fraschke M, Skibitzki O, Schroeder T and Lupina G, *Tunable Schottky barrier and high responsivity in graphene/Sinanotip optoelectronic device,* 2D Materials 4, 015024 (2017).

3. Giubileo F, Di Bartolomeo A, Martucciello N, Romeo F, **Iemmo L**, Romano P, Passacantando M, *Contact Resistance and Channel Conductance of Graphene Field-Effect Transistors under Low-Energy Electron Irradiation*, Nanomaterials 6, 206 (2016).

4. Di Bartolomeo A, Giubileo F, **Iemmo L**, Romeo F, Russo S, Unal S, Passacantando M, Grossi V and Cucolo A, *Leakage and field emission in side-gate graphene field effect transistors*, Applied Physics Letters 109, 023510 (2016).

5. Di Bartolomeo A, Giubileo F, Romeo F, Sabatino P, Carapella G, **Iemmo L**, Schroeder T, Lupina G, *Graphene field effect transistors with niobium contacts and asymmetric transfer characteristics*, Nanotechnology 26, 475202 (9pp) (2015).

6. Di Bartolomeo A, Giubileo F, **Iemmo L**, Romeo F, Santandrea S and Gambardella U, *Transfer characteristics and contact resistance in Ni- and Ti-contacted graphene-based field-effect transistor*, J. Phys.: Condens. Matter 25, 155303 (6pp) (2013).

7. Addonizio M L, Castaldo A, Antonaia A, Gambale E and **Iemmo L**, *Influence of process parameters on properties of reactively sputtered tungsten nitride thin films*, Journal of vacuum science and technology A 30, 031506 (2012).

8. Di Bartolomeo A, Sarno M, Giubileo F, Altavilla C, **Iemmo L**, S. Piano S, Bobba F, Longobardi M, Scarfato A, Sannino D, Cucolo A M and Ciambelli P, *Multiwalled carbon nanotube films as small-sized temperature sensors,* Journal of applied physics, 105, 064518 (2009).

9. Giubileo F, Di Bartolomeo A, Scarfato A, **Iemmo L**, Bobba F, Passacantando M, Santucci S and Cucolo A M, *Local probing of the field emission stability of vertically aligned multiwalled carbon nanotubes,* Carbon 47, 1074-1080 (2009).

10. Ambrosio M, Ambrosio A, Ambrosone G, Campajola L, Cantele G, Carillo V, Coscia U, Iadonisi G, Ninno D, Maddalena P, Perillo E, Raulo A, Russo P, Trani F, Esposito E, Grossi V, Passacantando M, Santucci S, Allegrini M, Gucciardi P G, Patane` S, Bobba F, Di Bartolomeo A, Giubileo F, **Iemmo L**, Scarfato A and Cucolo A M, *Nanotechnology: A new era for photodetection* , Nuclear Instruments and Methods in Physics Research A 610, 1–10 (2009).

11. Passacantando M, Bussolotti F, Santucci S, Di Bartolomeo A, Giubileo F, **Iemmo L** and Cucolo A M, *Field emission from a selected multiwall carbon nanotube,* Nanotechnology 19, 395701 (6pp) (2008).

12. Di Bartolomeo A, Giubileo F, Sarno M, Altavilla C, Sannino D, **Iemmo L**, Mancusi D, Bobba F, Cucolo A M and Ciambelli P, *Multiwalled carbon nanotube films as temperature nano-sensors*, Technical Proceedings of the 2008 NSTI Nanotechnology Conference and Trade Show, NSTI-Nanotech, Nanotechnology 2008. Vol 1, 2008, Pages 112-115 - Boston 1-5 June 2008.

13. Ambrosio M,..., Bobba F, Di Bartolomeo A, Giubileo F, **Iemmo L** and Cucolo A M, *Current results on the development of a carbon nanotube radiation detector,* Proceedings of the 10th ICATPP Conference on Astroparticle, Particle, Space Physics, Detectors and Medical Physics Applications, 8-17 - Villa Olmo, 8-12 October 2007.

Acknowledgments

I would like to thank all the people who contributed to completion of the thesis with their suggestions, criticisms and comments and who supported me over these years.

I would like to express my sincere gratitude and respect to my thesis advisor Prof. Antonio Di Bartolomeo for his excellent scientific and technical guidance, and because he motivated me with his constructive criticism.

A big thank you to Dr. Filippo Giubileo for his support over these years, his precious advices and the stimulating discussions.

I would also like to thank Dr. Nadia Martucciello for her cooperation, encouragement and for her friendship.

A heartfelt thank you to Prof. Maurizio Passacantando, who hosted me in his lab, and supported me scientifically and technically in this training.

A special thanks to Prof. Canio Noce, coordinator of my PhD, who guided me in meticulous and carefully way during these years.

I would also like to thank all my loved ones: my friends, my family, especially my children, *Aurora* and *Ivan*, born during this journey, to whom this work is dedicated.